2022

An Electrochemical, Fluidic, Chip-Based Biosensor for Biomarker Detection

Lauren Bell

University of Kentucky, bell.lauren51@gmail.com
Author ORCID Identifier:
ⓘ https://orcid.org/0000-0001-8407-4784
Digital Object Identifier: https://doi.org/10.13023/etd.2022.039

AN ELECTROCHEMICAL, FLUIDIC, CHIP-BASED BIOSENSOR
FOR BIOMARKER DETECTION

_____

THESIS

_____

A thesis submitted in partial fulfillment of the
requirements for the degree of Master of Science in
Biomedical Engineering in the College of Engineering
at the University of Kentucky

By
Lauren Bell
Lexington, Kentucky
Director: Dr. Guigen Zhang, Professor of Biomedical Engineering
Lexington, Kentucky
2022

ABSTRACT OF THESIS

AN ELECTROCHEMICAL, FLUIDIC, CHIP-BASED BIOSENSOR
FOR BIOMARKER DETECTION

Biosensors and their use in both the research and clinical field for the detection and monitoring of critical biomarkers are prevalent and constantly improving. However, continued research needs to be done to address shortcomings, such as low sensitivity, poor specificity, and poor readiness for integration into research use and patient care. The objective of this research was to create a combined fluidic, chip-based biosensor that could detect different biomarkers with high sensitivity and ease of use. For assessing the developed sensor, three separate biomarkers were tested: glucose, cholesterol, and oxygen. Both the glucose biosensor and cholesterol biosensor were combined with the microfluidic platform for biomarker detection testing. The oxygen biosensor was tested as a stand-alone chip, with future work including the combination with the microfluidic platform. Results of stepwise, amperometric tests prove the success of the microfluidic, chip-based biosensor for both glucose and cholesterol detection within the respective physiological ranges, with the glucose biosensor showing high sensitivity and a low limit of detection. The oxygen biosensor also proved successful in detecting changes in oxygen concentration in solution within physiological ranges of arterial oxygen partial pressure.

KEYWORDS: Amperometric Biosensor, Enzymatic Biosensor, Microfluidics, In-Situ
Biomarker Detection, Continuous Monitoring

Lauren Bell
_____

03/14/2022
_____

AN ELECTROCHEMICAL, FLUIDIC, CHIP-BASED BIOSENSOR
FOR BIOMARKER DETECTION

By
Lauren Bell

Dr. Guigen Zhang
Director of Thesis

Dr. Sridhar Sunderam
Director of Graduate Studies

03/14/2022
Date

DEDICATION

In memory of Rev. Dr. Robert V. Hale, or as I call him, Granddaddy.

ACKNOWLEDGMENTS

First and foremost, I would like to thank God for the opportunities and abilities He has given me and the support system He has blessed me with. Without Him none of this would be possible.

Next, I would like to thank my advisor, Dr. Zhang for his vital help on this research and for always pushing me and also encouraging me to continue to learn. Thank you for all your guidance and support over the past couple of years. I would also like to thank my Thesis Committee, Dr. Frédérique Yiannikouris and Dr. Sheng Tong, for their time and helpful advice along the way. Thank you for always being eager to provide assistance and contribute greatly through discussion.

In addition, I would like to thank my lab mates Erik Davis and David Alexander for always being a sounding board for my ideas and for providing great friendship and encouragement over the years.

Lastly, I would like to thank my parents, Tony Bell and Jennifer Hale, my boyfriend, Ali Elbakoush, and the rest of my family and my friends for their unending support and encouragement. Thank you for always being there to lift me up, force me to take a break, listen to me stress, and celebrate with me along the way. I would not have made it this far without every single one of you.

TABLE OF CONTENTS

LIST OF TABLES

LIST OF FIGURES

vii

CHAPTER 1.   INTRODUCTION

1.1   Overview of Biosensors

Biosensors are analytical devices that convert a biological reaction into a measurable and processable signal. A biosensor is typically regarded as made of three components: the sample, the transducer and the electronic system. However, the function of a biosensor is better understood by breaking down the structure further and dividing it into five parts, shown as parts a) through e) in Figure 1.1. The first part is recognition molecules, like bioreceptors that bind specifically to the analyte used or enzymes that facilitate a specific reaction. The second part is an interface where a particular biological binding or reaction event occurs and produces a signal, such as the electrodes on a screen printed electrode chip. The third part is a transducer element that converts and amplifies a biological event into physical, electronic signals. The fourth part is a computer software that processes the signal and coverts it to a quantitative parameter and the fifth part is an interface that presents the resulting quantity to the user (Grieshaber et al., 2008). Potential components of each of these parts and their interaction is shown in Figure 1.1. This creates the basic structure of a biosensor with each component depending on the type of sensor and analyte being detected.
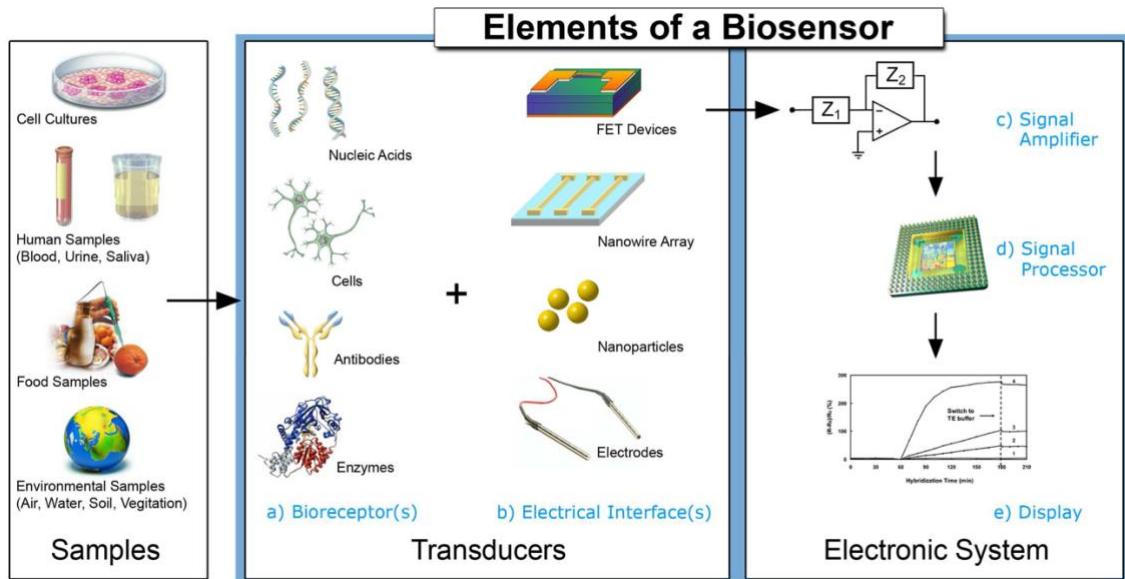
Figure 1.1 Elements of a typical biosensor (Greishaber et al., 2008).

Biosensors can be classified in a broad sense based on the type of recognition event that occurs. The two classifications are bioaffinity devices and biocatalytic devices. Bioaffinity devices involve selective binding of a target analyte to a surface-immobilized ligand coupler, such as an antibody (Murugaiyan et al., 2012). This classification can be further divided into subclasses depending on the particular binding mechanism, such as immunosensors, DNA biosensors, and cell biosensors (Liang et al., 2016). In comparison, biocatalytic devices involve the utilization of an enzyme for catalyzing an anticipated bioreaction. Because of this, enzymatic biosensors are the most common example of biocatalytic devices (Borisov and Wolfbeis, 2008). A commonly known and frequently used example of this is diabetes sensor strips.

Biosensors can also be classified based on the transduction mechanism, such as electrochemical sensors and optical sensors. The literature review in Chapter 2 provides details and examples of biosensors based on transducer classification. A summary is

provided in Table 1.1 of the function, advantages, and disadvantages of the different types

of sensors that will be discussed in more detail later.

Sensor Type (transducer classification)	Transducer Function	Advantages	Disadvantages
Electrochemical	converts chemical signal into an electronic signal	simplicity, low cost, rapid results, reproducibility, exceptional detection limits, miniaturization capability	low sensitivity, low specificity
Optical	converts light rays into an electronic signal	miniaturization capability, multi-analyte detection, high sensitivity, high specificity, rapid results, doesn't require molecule labeling	ambient light interference, expensive, delicate, complex to operate
Mechanical	converts mass or position change into an electronic signal	rapid results, high sensitivity, efficient with limited sample processing	not easily reproduced
Biosensors on-a-chip (microfluidic & chip combination)	dependent on type of sensor chip	small volume of concentrations, quicker diagnostics through the manipulation of the sensor geometry, highly sensitive real-time measurements, wide range of designs and techniques	undesirable adsorption of non-specific molecules, solution interference

Table 1.1 Summary of the function, advantages, and disadvantages of the types of biosensors discussed in Chapter 2.

Several characteristics can be used to compare the relative performance of different

types of biosensors. One characteristic is response time, that is, how fast a change in the

environment produces a change in signal. To have an ideal performance, changes in the

environment should produce a fast change in the resulting signal. Another important characteristic is the limit of detection (LOD), which provides the lowest concentration of an analyte that can be definitively detected. Lastly, selectivity and sensitivity are two of the most common and important characteristics to evaluate. Selectivity measures whether the sensor is responding only to the analyte being measured with no interference. Sensitivity evaluates a change in detection based on a change in concentration (Catherino, 2006).

One aspect of biosensor function that seems to be scarcely studied and included in experimental design and testing is the role of reaction kinetics and mass transport in biosensing. Different analytes possess different reaction kinetics and mass transport properties that play a role in their transport to and interaction with the biosensor surface. The limit of detection, an important response feature as explained above, is often determined by the mass transport of an analyte to the surface of the biosensor (Jin et al., 2019). Mass transport can be governed by diffusion, convection, electromigration, or a combination of these. Understanding what mass transport process is occurring can help with biosensor optimization. In a study done by Anandan et al. (2007), the impact of reaction kinetics and mass transport on glucose sensing electrodes integrated with nanopillars was investigated. They found that for functionalized nanopillar array electrodes (NAEs), or electrodes containing arrays of pillar shaped nanostructures with diameters measuring on the nanoscale, an increased current response resulted due to the successful mass transport that was aided by the low reaction rate constant of glucose. Their study echoed the need for sensor optimization to accommodate the specific reaction kinetics and mass transport properties of the analyte being used.

Biosensors provide a wide range of applications in both the clinical and research fields, including biomarker detection and analysis, drug discovery, in-situ monitoring and diagnostics. However, there are ongoing challenges facing biosensing, which include but are not limited to low sensitivity, poor specificity and proneness to fouling (Anandan et al., 2007). Continued research into the advancement and improvement of biosensor design and techniques of use is critical for medical advancement.

1.2   Objectives

Currently, there is an urgent need for rapid, specific, and reliable detection and monitoring systems in both the research and clinical fields. Biosensors are well equipped to fit this need and can be used in a multitude of different ways, either as a stand-alone method or combined with other sensor platforms, imaging modalities or analysis techniques. The use of biosensors is not a new concept, however, many improvements still need to be made. Hence, continual research is being performed to improve biosensors and their ability for in-situ monitoring and diagnostics.

Based on this need and the promising potential of biosensors used for biomarker detection, the overall focus of this research is to develop an in-situ technique to measure multiple biomarkers in vitro. More specifically, the objective of this research is to develop a practical and cost-effective means to detect biomarkers in-situ, including glucose, cholesterol, and oxygen.

1.3 Structure of Thesis

Chapter 1: Introduction. Provides background information and an overview of biosensors, including the elements of their construction and the testing characteristics. Describes the objectives of this thesis and outlines the structure of this thesis.

Chapter 2: Literature Review. Provides a survey of the relevant literature focused on the mechanism and applications of different types of biosensors, mainly electrochemical biosensors, as well as other types of biosensors. Unmet needs within the field are also explored.

Chapter 3: Glucose Detection Biosensor. Provides details on the materials, sensor biofunctionalization methods, and detection mechanism, as well as discusses the results for the glucose detection biosensor.

Chapter 4: Cholesterol Detection Biosensor. Provides details on the materials, sensor biofunctionalization methods, and detection mechanism, as well as discusses the results for the cholesterol detection biosensor.

Chapter 5: Oxygen Detection Biosensor. Provides details on the materials, sensor biofunctionalization methods, and detection mechanism, as well as discusses the results for the oxygen detection biosensor.

Chapter 6: Conclusion and Future Work. Provides a summary of the major outcomes of this thesis and discusses future research work.

CHAPTER 2.   LITERATURE REVIEW

2.1   Electrochemical Biosensors

Electrochemical biosensors are a method of sensing that commonly utilizes a three-electrode system consisting of a reference electrode, a working electrode, and a counter electrode. Some designs use only a two-electrode system, consisting of a reference and working electrode, but it is less common. The reference electrode is usually made from silver-silver chloride (Ag/AgCl) or is a saturated calomel electrode (SCE) and maintains a stable potential by remaining a constant potential drop across the electrode-liquid interface. Ag/AgCl and SCE reference electrodes are able to maintain a constant and known potential because they are composed of a fixed concentration of chloride. The working electrode functions as the site of the primary half-cell reaction and the counter electrode as the site of companion half-cell reaction to facilitate continuing flow of electrons to maintain an electrochemical reaction. This type of sensors provides an attractive design since there is a direct transduction of a biological reaction into electrical signal (Figure 2.1).
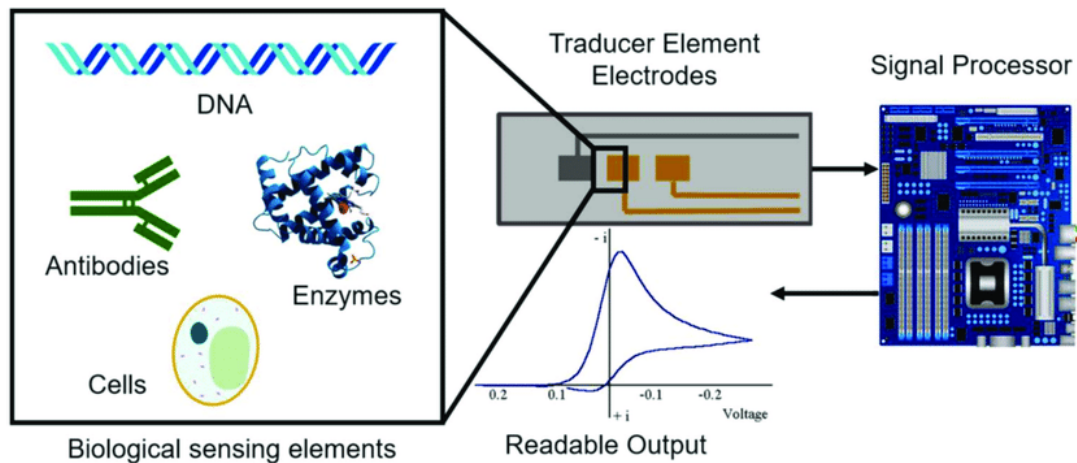
Figure 2.1 Schematic of an electrochemical biosensor (Hernandez-Vargas et al., 2018). (https://creativecommons.org/licenses/by/4.0/legalcode) (no changes made)

Electrochemical biosensors supply many desirable advantages, such as simplicity, low cost, rapid results, reproducibility, exceptional detection limits and miniaturization capability. They are also advantageous due to their low power consumption and compatibility with microfabrication technologies. However, there are some disadvantages that allude to more research being performed and design modifications being made. These undesirable properties include low sensitivity and low specificity. In complex biological samples, issues arise with detection accuracy and the inability to distinguish from background material in the sample (Grieshaber et al., 2008, Gangadharan et al., 2011). In order to be successful and useful in a clinical setting, sensors need high sensitivity and specificity in the human media being tested.

This type of sensor requires biomolecule immobilization techniques that each come with advantages and disadvantages, with the chosen immobilization technique depending on the design and intended use of the sensor. One technique is physical adsorption to the surface. This method is reversible and involves the biomolecule being attached or physically adsorbed to the material surface. This is desirable due to its simplicity and the absence of harsh chemicals. However, this method is not considered reliable or reproducible and can result in undesirable leaching during storage. Another technique used is cross-linking reagents. This method is irreversible and involves using crosslinkers to create strong covalent bonds that anchor biomolecules to the surface. This method can result in stabilized proteins, which can lead to higher stability, but this method can also cause loss of activity. Entrapment within a polymer or gel is another technique that is used. Entrapment is an irreversible method that involves an enzyme held in place by a polymeric gel structure. Substrates and other products are then allowed to traverse. This technique is

convenient, gentle, and the degree of cross-linking can be controlled, which can minimize undesirable leaching. Covalent attachment, an irreversible technique that involves chemical coupling of biomolecules, has an advantage in that it is pH, temperature and ionic strength resistant. Lastly, utilizing biomolecular interactions, known as affinity binding, is a reversible technique that relies on a particular biochemical reaction. This method is beneficial because the properties of the reaction can create a detectable response (Catherino, 2006, Asal et al., 2018). Figure 2.2 provides an illustration of the immobilization methods discussed.
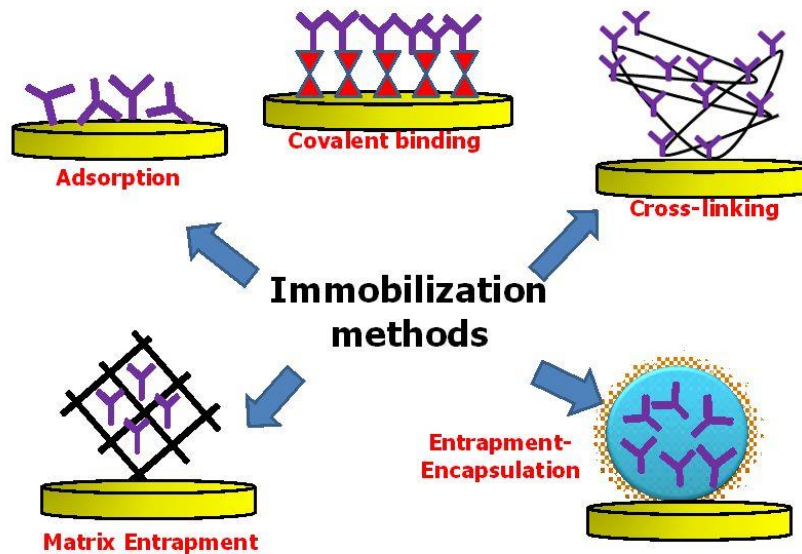
Figure 2.2 Schematic of biomolecule immobilization techniques (Rodriguez et al., 2015). (https://creativecommons.org/licenses/by/3.0/legalcode) (no changes made)

Kim et al. (2019) has recently conducted research on creating an electrochemical biosensor that is both stretchable and disposable. Previous studies have been done on stretchable, electrochemical biosensors for detecting ions, uric acid, and glucose, but no studies have been conducted on detecting specific protein biomarkers. In this study, a sensor was created that could detect low concentrations of tumor necrosis factor alpha

(TNF-α), which is an inflammation biomarker. TNF-α-activated signal transduction pathways play a key role in vascular dysfunction, hypertension and atherosclerosis (Urschel and Cicha, 2015). Therefore, this biomarker may be important to monitor with respect to cardiovascular disease (CVD). There proved to be durability and high stability after static and cyclic stretching, suggesting that this design condition could be further applied to wearable sensors.

Electrochemical biosensors have been utilized in the detection of an array of biomarkers, both lipidic and amphiphilic. The most common and successfully commercialized use is for the detection of glucose, in the form of glucose monitors used primarily by individuals with diabetes (Kubicek-Sutherland et al., 2017). Further, when considering cardiac biomarkers in particular, electrochemical biosensors have been used to detect cardiac troponin I or T (cTnI/T), myoglobin, C-reactive protein (CRP), Lipoprotein-associated phospholipase A, IL-6, LDL and MPO. Out of these, one of the most noteworthy, presented by Qureshi et al. (2012), is a miniaturized point-of-care sensor used for detecting myoglobin, with the ability to detect a concentration of 100 ng/ml. This sensor functions through the use of an antibody layer that is immobilized on a planar gold electrode. Cardiac enzyme is seized by this layer and sensed through impedimetric sensing.

CRP is a cardiac biomarker known to be a sensitive indication of infection, inflammation and cardiac risk. Current CRP testing methods used in a clinical setting, such as enzyme-linked immunosorbent assay (ELISA), are time consuming, inaccurate or don't produce an acceptable sensitivity. Due to this, Bryan et al. (2013) have developed and optimized an electrochemical, label free biosensor that is reusable and provides consistent detection of CRP in dilute or whole blood serum. Other sensor types developed for CRP

detection were researched (surface plasmon resonance, piezoelectric microcantilevers, microfluidics, etc.) and electrochemical methods proved to be most advantageous for low cost, sensitivity and flexibility.

Electrochemical biosensors can be further classified based on the type of measurement that is taken. More specifically, these biosensors can be classified as amperometric, potentiometric, impedimetric, and conductometric. These subclasses of electrochemical biosensors will be discussed in further detail next.

2.1.1   Amperometric

Amperometric biosensors are a subclass of the electrochemical biosensor and involve the transfer (either loss or gain) of electrons. This subclass functions by applying a potential, or voltage, to the system and measuring the current response that arises from electron transfer on the working electrode that results from the biochemical reaction that takes place, and the products that are oxidized or reduced during this reaction (Chaubey and Malhotra, 2002). For enzyme sensors, reactions involving a single analyte, or substrate, can be written in a general form:

$$E + S \rightleftharpoons ES \longrightarrow E + P \tag{1}$$

where E is the enzyme, S is the substrate and P is the product. The intermediate complex ES breaks down into products P and liberates the enzyme (Wang, 2000). For example, a common final reaction that is monitored amperometrically is the liberation of hydrogen peroxide, denoted as:

$$H_2O_2 \xrightarrow{electrode} O_2 + 2H^+ + 2e^- \tag{2}$$
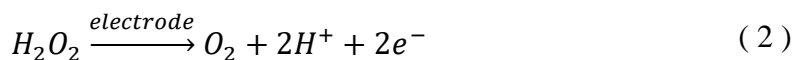
This enzymatic activity determines the sensor response in the form of the resulting electrochemical current. In the above example, an oxidation reaction is occurring, denoted by the loss of electrons. In general, the loss or gain of electrons, depending on if an oxidation or reduction process is occurring, leads to the current measurement. The more efficient the electron transfer, the larger the current response. The peak current value measured over a linear potential range is directly proportional to the bulk concentration of the analyte (Grieshaber et al., 2008). As discussed previously, two half-cell reactions occur on the working and counter electrode. The electrochemical event occurs at the working electrode and produces either a reduction or oxidation. If reduction occurs at the working electrode, oxidation occurs at the counter electrode. Due to this, the counter electrode should be composed to be as inert as possible (Elgrishi et al., 2018). The composition of the transducer varies based on the type of sensor being used and the particular reaction taking place. Because of the need for an inert material, amperometric biosensors use metal or carbon electrodes, or chemically modified electrodes (CMEs) as the transducer element (Catherino, 2006).

Reactions that occur can be mediated or non-mediated, as shown in Figure 2.3. Mediators are synthetic electron transferring vehicles that can freely partake in the redox reaction with the biological component. This assists in rapid electron transfer. There are different types of mediators including ferrocene, conducting salts, quinones, and many others (Chaubey and Malhotra, 2002). Mediators may improve a sensors sensitivity and specificity, as well as contribute to a faster response time. Also, mediated enzyme electrodes have lower electrode potentials and therefore are less receptive to interfering elements.

Mediated Electron Transfer

Unmediated Electron Transfer
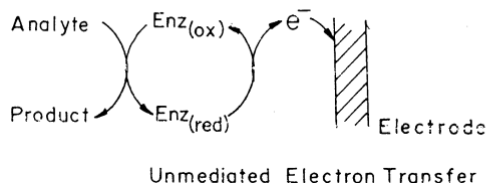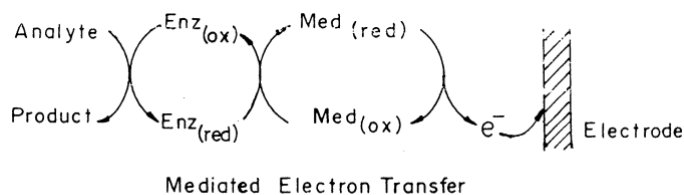
Figure 2.3 Schematic of mediated and unmediated electron transfer (Chaubey and Malhotra, 2002). Reprinted from Biosensors and Bioelectronics, 17, A. Chaubey and B.D. Malhotra, Mediated Biosensors (Review), 441-456, 2002, with permission from Elsevier.

The behavior of amperometric biosensors can be visualized mathematically by examining the Cottrell equation:

$$i(t) = \frac{nFACD^{1/2}}{\pi^{1/2}t^{1/2}} \qquad (3)$$

where n is the stoichiometric number of electrons involved in the reaction, F is Faraday's constant, A is the area of the electrode (cm^2), C is the concentration of the electroactive species (mol/cm^3), D is the diffusion constant for the electroactive species (cm^2/s) and t is time. This equation shows the change in current with respect to time and it can be seen that the current is proportional to the square root of the diffusion rate. The diffusion constant can be found by rearranging the equation and determining the number of electrons using amperometric techniques. Current depends on the rate at which the analyte diffuses to the electrode, so current is diffusion controlled. This behavior can be visualized graphically through the Cottrell diffusion curve, shown in Figure 2.4.
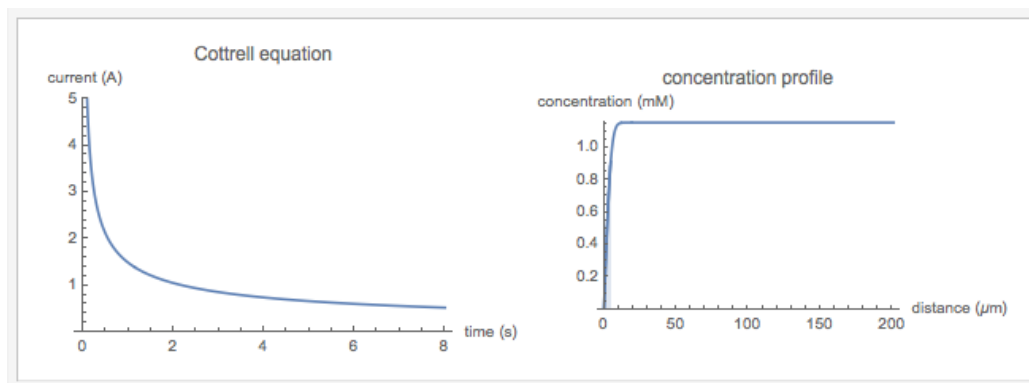
Figure 2.4 The plot on the left shows that current is inversely proportional to the square root of πt. The plot on the right shows the corresponding concentration profile. (Trinh, 2011). (https://creativecommons.org/licenses/by-nc-sa/3.0/) (no changes made)

Amperometric biosensors can be used to measure cholesterol concentration in the blood. This is important due to the negative relation between cholesterol content, atherosclerosis and CVD. Enzymatic amperometric biosensors have laid the foundation and have become the most commonly used approach for cholesterol biosensors. This approach involves the immobilization of an enzyme, most commonly cholesterol oxidase, ChOx, on the electrode surface. Electron transfer between the electrode and the enzyme occurs due to a redox reaction between the enzyme and cholesterol. Cholesterol is catalyzed by ChOx and leads to O_2 consumption and H_2O_2 production. The O_2 consumption and H_2O_2 production that occurs is not measured directly. Instead, as described by the Cottrell equation, the current that is measured expresses the rate of electron transfer occurring in the reaction. Further, since the analyte concentration that is present is proportional to the current outputted, the cholesterol concentration is able to be measured (Saxena and Das, 2016).

Although these cholesterol sensors have their advantages in their in-situ monitoring capabilities and their easiness to be miniaturized, there are a few disadvantages, such as a lack of sensitivity and stability. A common strategy to counter the reduction in current

14

signal that occurs with the reduction in electrode size is to increase the surface area through the use of nanostructures (Gangadharan et al., 2011). Saxena and Das (2016) presents the addition of nanomaterials to their design in order to combat these disadvantages. Different types of nanoparticles (metal, metal oxide, carbon nanotubes) have been used to improve the amperometric cholesterol biosensor (Figure 2.5).
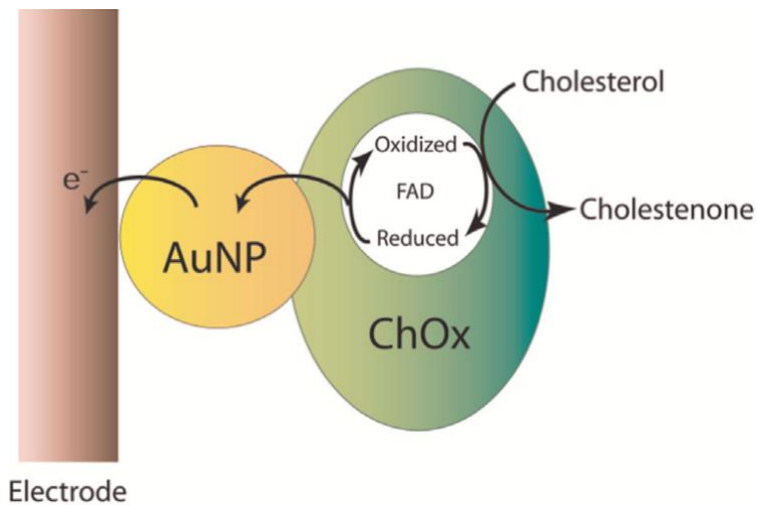
Figure 2.5 Facilitation of electron transfer between the electrode and the ChOx redox center by AuNP's (Saxena and Das, 2016). Reprinted from Biosensors and Bioelectronics, 75, U. Saxena and A.B. Das, Nanomaterials Towards Fabrication of Cholesterol Biosensors: Key Roles and Design Approaches, 196-205, 2016, with permission from Elsevier.

Carbon nanotubes (CNTs) are most commonly used for cholesterol biosensors because of their strong electrocatalytic properties for H_2O_2. Nanomaterial incorporation in different ways has shown to increase both the sensitivity and stability of the cholesterol sensor specifically (Saxena and Das, 2016).

Chauhan and Pundir (2014) presented an amperometric biosensor for the detection of acetylcholine. It is believed that Alzheimer's disease can result, in part, from dysfunctional regulation of the neurotransmitter acetylcholine. This biosensor was created by co-immobilizing acetylcholinesterase and choline oxidase onto nanocomposite of

chitosan (CHIT)/gold-coated ferric oxide nanoparticles (Fe@AuNPs) deposited onto a Au working electrode. The reference electrode was composed of Ag/AgCl and the counter electrode was a platinum wire connected through the potentiostat. The H_2O_2 that resulted from the oxidation of choline by immobilized choline oxidase was measured electrochemically using cyclic voltammetry. Measurement of acetylcholine was also performed in fresh plasma samples from both healthy persons and persons suffering from Alzheimer's disease. This sensor showed to have high specificity, a fast response time of 3 seconds, and a low detection limit of 0.005 μM. It provided accurate results when compared with the current method of detection, high performance liquid chromatography (HPLC), graphically seen in Figure 2.6.
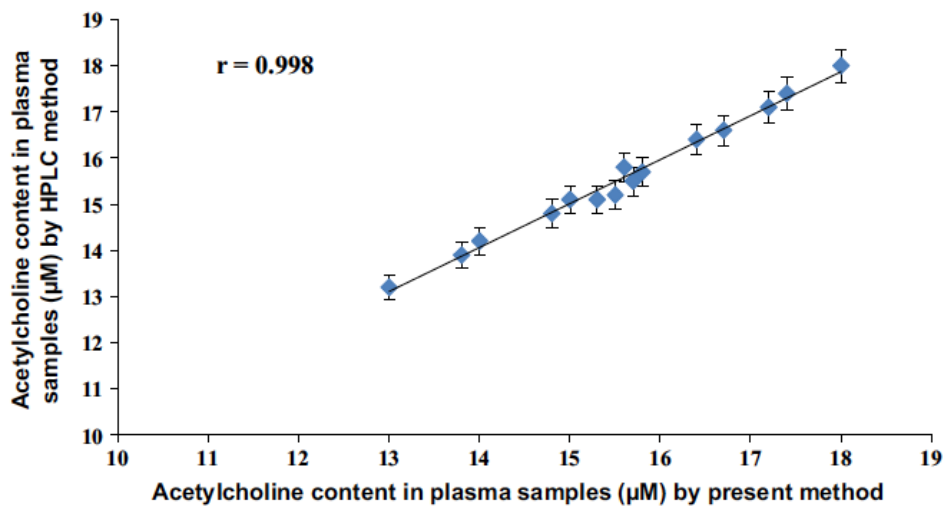
Figure 2.6 Correlation between acetylcholine values determined by the discussed biosensor (x-axis) and by standard HPLC method (y-axis) (Chauhan and Pundir, 2014). Reprinted from Biosensors and Bioelectronics, 61, N. Chauhan and C.S. Pundir, Amperometric Determination of Acetylcholine – A Neurotransmitter, by Chitosan/Gold-Coated Ferric Oxide Nanoparticles Modified Gold Electrode, 1-8, 2014, with permission from Elsevier.

2.1.2   Potentiometric

A second subclass of the electrochemical biosensor is the potentiometric biosensor, which functions by measuring the potential at the working electrode with respect to the reference electrode under equilibrium conditions. The accumulation of charge is measured with zero or no significant current flowing between the two electrodes. The change in voltage results from the selective binding mechanism that occurs at the electrode surface (Chaubey and Malhotra, 2002). The relationship between potential and concentration is governed by the Nernst equation:

$$E_{cell} = E_{cell}^0 - \frac{RT}{nF} \ln{(Q)} \qquad (4)$$

where E_{cell} is the observed cell potential at zero current or the electromotive force (EMF) of the cell, E_{cell}^0 is a constant potential contribution to the cell, R is the universal gas constant, T is absolute temperature in degrees Kelvin, n is the charge number of the electrode reaction, F is the Faraday constant, and Q is the ratio of ion concentration at the anode to ion concentration at the cathode (Grieshaber et al., 2008). Transducer types for potentiometric biosensors include ion-selective electrodes (ISE), glass electrodes, gas electrodes, metal, and metal hybrids (Catherino, 2006).

Potentiometric biosensors can be used to measure cholesterol, a lipid antigen. Lipid antigens are detected using lipid films (Kubicek-Sutherland et al., 2017). One such successful example is a potentiometric cholesterol biosensor created with graphene consisting of polymeric lipid membranes. This biosensor was tested in real blood serum samples and proved to have a lower detection limit than previously reported devices, making it useful for clinical analysis and practical applications. The resulting EMF data is shown in Figure 2.7. This figure also shows how the stability and reusability of the

17

biosensor was tested and presented promising results. However, it is noted that these experiments were conducted in solution with a pH value of 7.0, since it was determined this provides the optimal response from the biosensor (Nikoleli et al., 2013). The normal pH range for human blood is about 7.35 to 7.45 (Lewis, 2020). It would be important to perform further testing and note the effect of this increased pH on the biosensor performance.
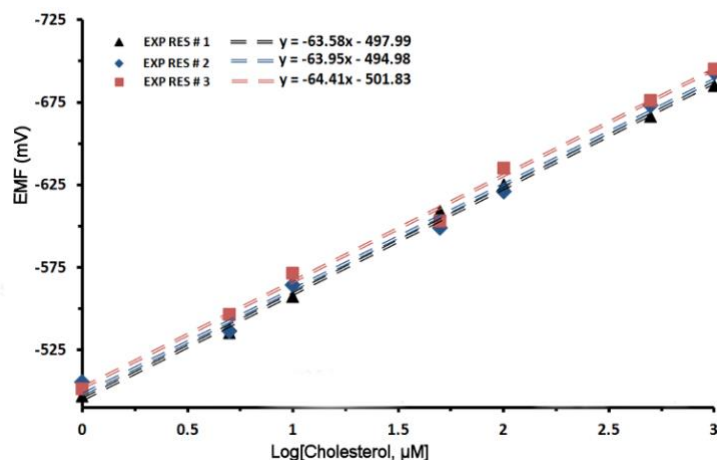
Figure 2.7 Calibration Curves for three consecutive experiments on single biosensor (Nikoleli et al., 2013). (https://creativecommons.org/licenses/by-nc-nd/3.0/legalcode) (no changes made)

2.1.3 Impedimetric

A third subclass of the electrochemical biosensor is the impedimetric biosensor, which involves a change in electron transfer behavior across the electrode-liquid interface resulting from a change in impedance consisting of resistance and capacitance occurring at the working electrode as selective binding occurs. Impedimetric biosensors can be visualized through circuit models, as shown by the Randles circuit model in Figure 2.8.
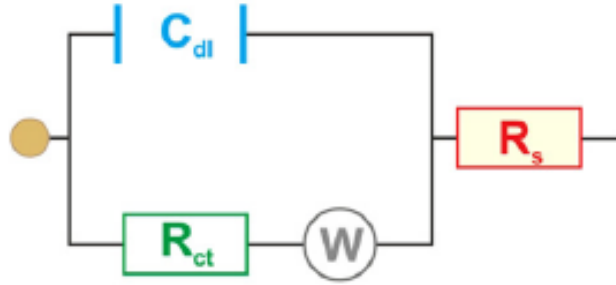
Figure 2.8 Common Randles circuit model for impedimetric measurements (Ahmed et al., 2014). Republished with permission of Clinical Microbiology Reviews, form Biosensors for Whole-Cell Bacterial Detection, A. Ahmed, J.V. Rushworth, N.A. Hirst, P.A. Millner, 27, 3, 2014; permission conveyed through Copyright Clearance Center, Inc.

R_s is the solution resistance, C_{dl} is the double layer capacitance, R_{ct} is the charge transfer resistance and W is the Warburg impedance, which is only observed in some operations at a low frequency (Ahmed et al., 2014). Mathematically, impedance for a simplified Randles circuit that doesn't include Warburg impedance can be calculated by using the following equation:

$$Z = R_s + \frac{R_{ct}}{1 + j\omega R_{ct} C_{dl}} \tag{5}$$

This relationship is shown graphically in Figure 2.9 A. R_s represents the solution resistance, R_{ct} represents the charge transfer resistance, and C_{dl} represents the double-layer capacitance. This provides the impedance response curve shown, with the semicircular shape indicating electron transfer blockage across an electrode/electrolyte boundary (Anandan et al., 2009). R, the resistance, termed the "real component of impedance", is located on the x-axis, and C, the capacitance, termed the "imaginary component of impedance" is located on the y-axis. It is shown that as the diameter of the semi-circle changes, the impedance changes. Nyquist plots showing both a semicircle and linear region indicate a combination of kinetics-controlled and diffusion-controlled electrode processes.

For example, if at low frequency the linear region of the Nyquist plot is absent, it would be inferred that after various molecules are adsorbed, the process is kinetics-controlled and is no longer diffusion-controlled (Lee et al., 2008). A kinetics-controlled reaction is a reaction limited by the rate of electron transfer, whereas a diffusion-controlled reaction is a reaction in which the rate is dependent on the diffusion of electroactive species from a region of high concentration to a region of low concentration, or the mass transport of the species to the surface of the electrode.

In practice, measuring impedance is done by applying a voltage and measuring the resulting current and phase shift. The impedance is given by this current-voltage ratio, and can either increase or decrease depending on the analyte being studied (Rushworth et al., 2013). For example, if a voltage is applied, then the voltage (V) and resulting current (I) would take the form:

$$V = V_{DC} + V_{AC}\sin(\omega t) \ and \ I = I_{DC} + I_{AC}\sin(\omega t - \varphi) \tag{6}$$

And the impedance would have a magnitude of:

$$Z(\omega) = \frac{V_{AC}}{I_{AC}} \tag{7}$$

and phase φ (Daniels and Pourmand, 2007).
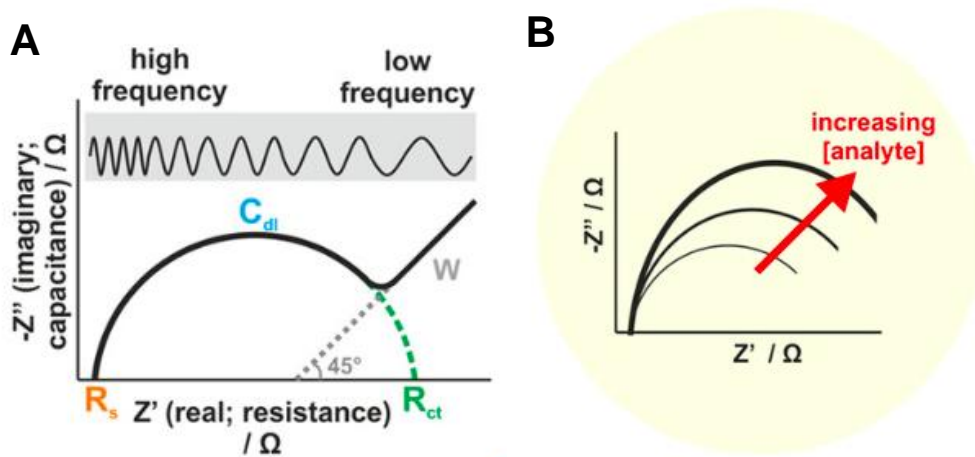
Figure 2.9 Nyquist plot containing features of Randles circuit (A) and changes in impedance resulting from analyte-surface interactions (B) (Ahmed et al., 2014). Republished with permission of Clinical Microbiology Reviews, form Biosensors for Whole-Cell Bacterial Detection, A. Ahmed, J.V. Rushworth, N.A. Hirst, P.A. Millner, 27, 3, 2014; permission conveyed through Copyright Clearance Center, Inc.

The response curve that results from impedance measurement provides the relationship between the output variable of the sensor and the concentration of the target analyte (Daniels and Pourmand, 2007). Since impedimetric biosensors present a change in capacitance and electron transfer resistance across the working electrode as a result of analyte-bioreceptor interaction, it follows that as analyte binding increases the impedance changes. As shown in Figure 2.9 B, the impedance changes that result from these interactions are proportional to the analyte concentration present (Ahmed et al., 2014).

In a review by Bahadir and Sezginturk (2016), it is stated that there are two main recognition mechanisms of impedimetric sensors that are studied. These types are impedimetric immunosensors, which involve antibodies and antigens binding causing electron transfer and a change in resistance, and impedimetric aptasensors, which involve the binding of target sequences, DNA damages, or conformational changes that result in impedance changes. Both recognition mechanisms of impedimetric sensors have

advantages, such as reproducibility and high specificity. However, it is important to note that higher specificity, better stabilization and longer shelf left has been reported for the use of aptamers compared to antibodies.

This type of biosensor has been used for the detection of important Alzheimer's disease biomarkers. For example, an Electrochemical impendence spectroscopy (EIS) biosensor was created consisting of graphene oxide/gold nanoparticles (GNPs) and a hydrogel electrode with the immobilization of cellular prion protein (PrP^C) peptide probe on the GNPs to target soluble biomarker amyloid-beta oligomers (AβO) present in blood or cerebral spinal fluid (Sun et al. 2018). This sensor proved to be highly specific and sensitive for the detection of AβO, with a detection limit as low as 0.1 pM. The sensor was also able to distinguish between AβO and amyloid-beta monomers or fibrils.

Rushworth et al. (2014) have presented a label-free electrical impedimetric biosensor that also detects AβO in relation to Alzheimer's disease. Their design is similar to the previously mentioned design in that it utilizes PrP^C, however, instead of using hydrogel for attachment a biotin/NeutrAvidin bridge was used. EIS was used for analysis, along with cyclic voltammetry and scanning electron microscopy. This biosensor proved to be specific for detecting AβO and provided a detection limit of ~0.5pM, which is higher than the previously discussed design by Sun et al. (2018).

2.1.4   Conductometric

A fourth subclass of the electrochemical biosensor is the conductometric biosensor, which measures conductance changes between two electrodes as a result of the biochemical reaction that occurs (Chaubey and Malhotra, 2002). Conductometric biosensors are sometimes noted as a subclass of the impedimetric biosensor since conductance is the

inverse value of resistance (Pohanka and Skladal, 2008). Based on this relationship,

conductance can be derived from Ohm's law ($V = I * R$), giving conductance as:

$$G = \frac{I}{V} \qquad\qquad (8)$$

where V is voltage, I is current, R is resistance and G is conductance. For conductometric

sensing, a voltage is applied to the system and a resulting current is measured. When

voltage is applied, a biochemical reaction occurs that changes the concentration of the ionic

species. This change in ionic concentration leads to a change in current flow. By examining

equation (8), it can be seen that a change in current will result in a change in conductance.

An example of this measurement is shown in Figure 2.10.

This type of biosensor is commonly used to study enzymatic reactions (Grieshaber

et al., 2008). Metal electrodes are the most commonly used transducer type for this type of

biosensor (Catherino, 2006). Clinical samples have varying and potentially complex ionic

backgrounds and require the measurement of small conductance changes in media of high

ionic strength. This presents a limitation for conductometric biosensors and restricts the

applicability for this form of biosensing in real clinical applications (Grieshaber et al.,

2008).

A single polyaniline (PANI) nanowire biosensor with an integrated microfluidic

channel has been developed that can successfully detect myoglobin (Myo), cardiac

troponin I (cTnI), creatine kinase-MB (CK-MB), and b-type natriuretic peptide (BNP),

which are critical biomarkers used in diagnosing CVD (Lee et al., 2012). In this design,

conductance measurement was chosen due to its ability to produce a quick response and

function without the need for a reference electrode. Microfluidic channels were integrated

for more precise sensing, to slow flow of the solution through only the active portion of

the PANI nanowire, for reliable sensing and for overall system stability. Conductance

measurement detection results are shown in Figure 2.10.
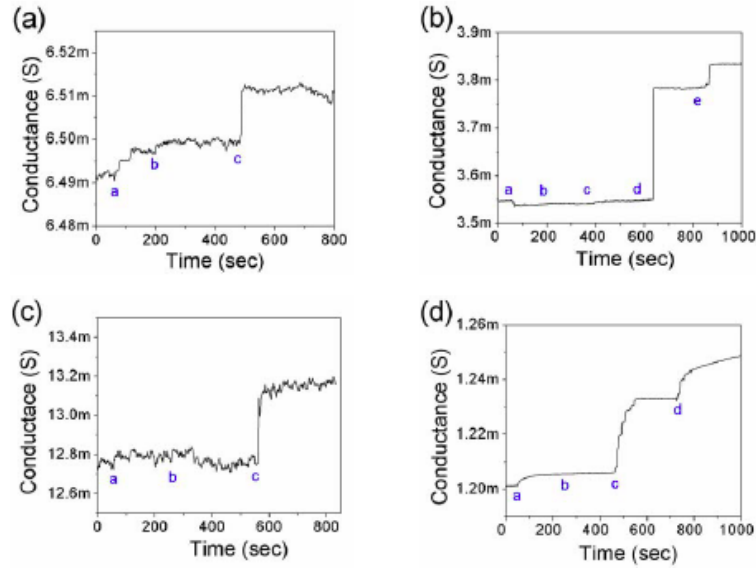
Figure 2.10 (a) Detection of Myo (a: PBS, b: 100 ng/mL BSA, and c: 100 pg/mL Myo); (b) Detection of cTnI (a: PBS, b: 10 ng/mL BSA, c: 5 fg/mL cTnI, d: 250 fg/mL cTnI, e: 20 pg/mL cTnI); (c) Detection of CK-MB (a: PBS, b: 10 mg/mL BSA, c: 150 fg/mL CK-MB); (d) Detecion of BNP (a: PBS, b: 100 ng/mL BSA, c: 50 fg/mL BNP, and d: 1 pg/mL BNP) (Lee et al., 2012). (https://creativecommons.org/licenses/by/3.0/legalcode) (no changes made)

Overall, this sensor design detects Myo, cTnI, CK-MB and BNP at low

concentration levels while maintaining very high sensitivity and specificity, and having

good reproducibility.

2.2   Other Biosensors

Although this thesis is focused on electrochemical biosensors, to complete the survey of

literature other types of sensors were examined and are discussed in the next sections.

These sensor types include optical, mechanical, and on-chip biosensors.

2.2.1 Optical Biosensors

Optical biosensors are sensors that measure the light emitted or absorbed as a result of a biochemical reaction. Optical fibers or waveguides are used to guide the light wave to appropriate detectors (Chaubey and Malhotra, 2002). A schematic of a basic optical biosensor, including potential transducer elements, is shown in Figure 2.11. Different types of optical biosensors include colorimetric, fluorescence, luminescence, surface plasma resonance (SPR) and fiber optic. The specific theory and mechanism used to operate the biosensor depends on the chosen transducer and intended function. A few specific types will be described in more detail below.
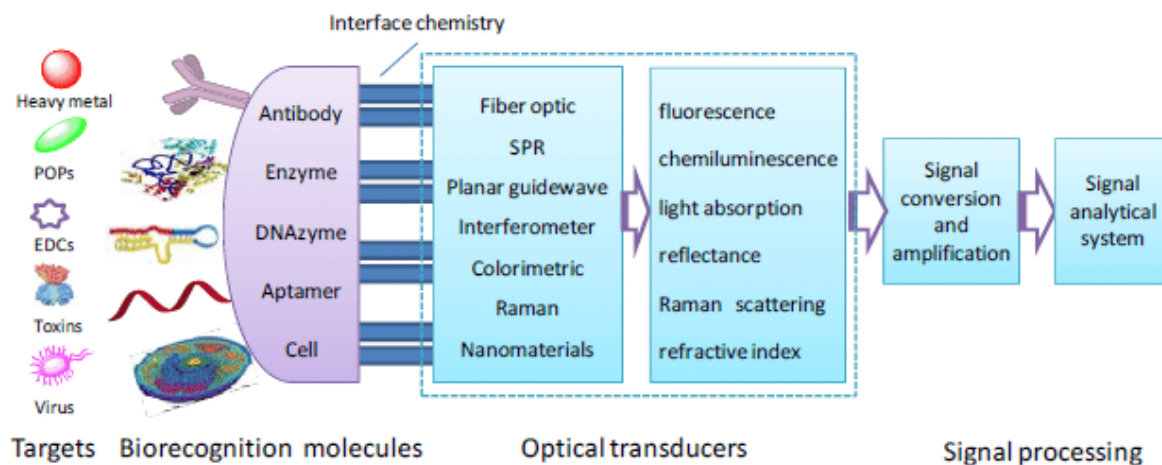
Figure 2.11 Schematic of an optical biosensor (Long et al., 2013).
(https://creativecommons.org/licenses/by/3.0/legalcode) (no changes made)

Optical biosensors are advantageous due to their sensitivity, ability to produce rapid results, high specificity, and the ability to produce quantitative and kinetic measurements (Qureshi et al., 2012). Furthermore, optical biosensors do not require molecule labelling to produce a higher accuracy and allow for in-situ monitoring. However, the sensors can be delicate and costly, and familiarity of the theory of the experiment and of optics may be

required by the user to obtain meaningful results (Ramsden, 1997). Further limitations that have encouraged more research into creating a more robust optical sensor are miniaturization difficulty, a lack of resolution, and issues with efficient use in turbid media.

Different forms of optical biosensors have been used to detect promising biomarkers for the diagnosis and progression analysis of Alzheimer's disease. One example, by Song et al. (2018), uses a label-free optical nanosensor design to detect AD biomarkers beta-amyloid (Aβ42) and total tau (T-tau) in buffer and in CSF. Four nanosensors were fabricated on a chip, with one sensor acting as a reference, one used to detect Aβ42, one used to detect T-tau, and the last to detect a mixture of Aβ42 and T-tau. When the specific biomarker binds to the corresponding antibody immobilized on the sensing surface, a shift occurs in the reflected optical signal and this is monitored. This sensor design proved to have important advantages such as high specificity and sensitivity, great repeatability, low cost and ease of operation, making them a promising device for point-of-care diagnostics. The detection limit was also low in buffer, with Aβ42 detectable at 7.8 pg/ml and T-tau detectable at 15.6 pg/ml.

Although there are many different subclasses of optical biosensors, two have been chosen to be examined further: surface plasmon resonance (SPR) optical biosensors and fiber optic SPR biosensors.

2.2.1.1   Surface Plasmon Resonance (SPR)

Surface plasmon resonance is a subset of optical biosensors that uses surface plasma waves to examine biomolecular interactions occurring at the surface of the sensor. Biomolecular recognition elements are immobilized on the surface. Analyte molecules

bind to these, and the refractive index is increased, which changes the propagation constant of the surface plasmon wave (SPW). A change is measured in one of the properties of the light wave interacting with the SPW (Homola et al., 2002). The properties measured are traditionally the wavelength, the incident angle or the intensity of the reflected light. The change that occurs in the measured property provides a measurement of the target analyte adsorbed (Hoa et al., 2007). The basics of the SPW vector (β_{SP}) is given by the following equation:

$$\beta_{SP} = Re \left\{ \frac{2\pi}{\lambda} \sqrt{\frac{\varepsilon_M \varepsilon_D}{\varepsilon_M + \varepsilon_D}} \right\} \qquad (9)$$

where λ is the wavelength of the incident light, ε_M is the value of the real part of the metal dielectric constant, and ε_D is the value of the real part of the medium dielectric constant (Prabowo et al., 2018).

In order for a light wave to couple to a SPW at a metal-dielectric interface, the component of light's wavevector that is parallel to the interface must match that of the SPW. In most cases, the light's wavevector needs to be enhanced to match the wavevector of the SPW and to allow for excitation of the SPW (Homola et al., 2002). This excitation can be done using different coupling methods such as grating coupling, waveguide coupling, fiber optic coupling (Liang et al., 2016) and prism coupling (Figure 2.12) (Homola et al., 2002).

SPR biosensing allows for both qualitative and quantitative measurement data, real-time measurements, and doesn't require labeling. SPR biosensors can detect concentration levels of an analyte from a complex sample, which is advantageous for clinical applications (Hoa et al., 2007). However, for compatibility purposes the metal surface of the electrode

has to be coated, and an analysis of the entire resonance curve is required, which is time-consuming (Ramsden, 1997). An example of a resonance curve is shown in Figure 2.12.
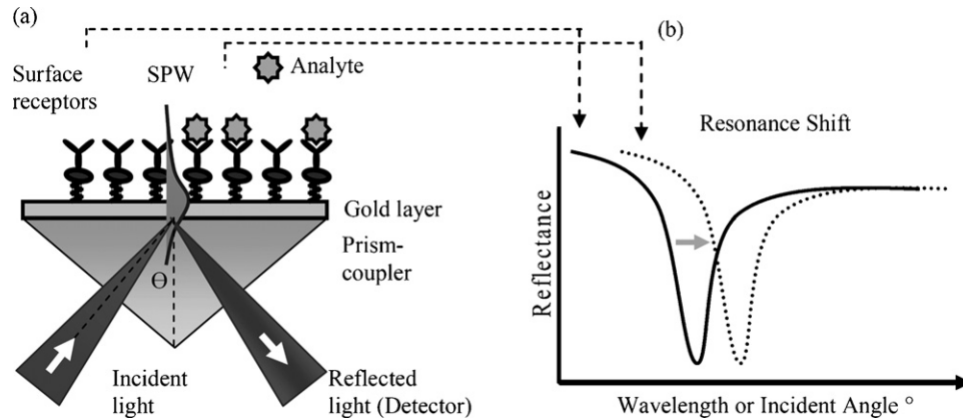
Figure 2.12 (a) schematic of prism-coupled structure and (b) resonance shift in reflected light spectrum (Hoa et al., 2007). Reprinted from Biosensors and Bioelectronics, 23, X.D. Hoa, A.G. Kirk, and M. Tabrizian, Towards Integrated and Sensitive Surface Plasmon Resonance Biosensors: A Review of Recent Progress, 151-160, 2007, with permission from Elsevier.

Traditional prism-coupled SPR designs are the general basis for today's commercial systems of SPR biosensors and will be discussed in greater detail in this paper. Advantages include simplicity, sensitivity and robustness. One main disadvantage is the inability or difficulty of miniaturization. This has caused alternatives, such as optical fibers and waveguide structures to be proposed and explored. There are also subsets of SPR biosensors that result in different sensitivities. These are fiber-SPR, waveguide-SPR, silicon-SPR, and multi-analyte SPR (Hoa et al., 2007).

To fully understand how coupling works, an example of a prism coupler will be examined. The underlying principle includes conducting the excitation using transverse magnetic ™ wave (k) through a medium that has a higher refractive index than the boundary dielectric medium. The resonance condition, or the point of intersection, can be described by (Prabowo et al., 2018):

$$k_X = \beta_{SP}$$

(10)

$$\frac{2\pi}{\lambda} * n_P * \sin \theta = \frac{2\pi}{\lambda} * Re \left\{ \sqrt{\frac{\varepsilon_M \varepsilon_D}{\varepsilon_M + \varepsilon_D}} \right\}$$

(11)

where n_P is the prism material and θ is the incident angle. It follows then that the incident angle can be calculated using the following equation:

$$\theta = \sin^{-1} \left[\left(\frac{1}{n_P} \right) * Re \left\{ \sqrt{\frac{\varepsilon_M \varepsilon_D}{\varepsilon_M + \varepsilon_D}} \right\} \right]$$

(12)

It is shown in Figure 2.13 that the propagation constant of incident light can couple the wavevector of SPW at the intersection point.
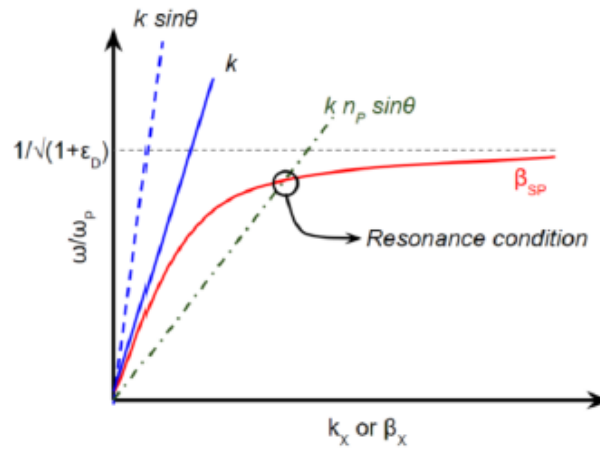
Figure 2.13 The relation between the dispersion of TM incident light coupling a SPW (Prabowo et al., 2018). (https://creativecommons.org/licenses/by/4.0/legalcode) (no changes made)

When performing an experiment using SPR, the shift in this incident angle is observed and measured and represents the adsorption activity when plotted as a function of time (Biosensing Instrument Inc., 2014). An example of results obtained from such an experiment is shown graphically in Figure 2.14.

SPR biosensors have been widely studied and used for detection of particular cardiac biomarkers. These include metalloproteinase (MMP)-2, B-type natriuretic peptide (BNP), cTnT, myoglobin, cTnl, TNF-a, and MPO. They have also been used for detecting modified CRP (mCRP), which is an important indicator for assessing risk of developing CVD (Qureshi et al., 2012). Hu et al. (2006) report on the creation of an SPR biosensor that can accurately detect mCRP in real time. The detection of both pentamer C-reactive protein (pCRP) and mCRP is analyzed in the study through the use of different monoclonal antibodies (Mabs) immobilized on a protein G layer, and pCRP is used independently to evaluate the detection level. Figure 2.14 shows the SPR responses, in the form of angle shift over time, that resulted from the binding of Mab C8 with pCRP and mCRP, indicating that Mab C8 reacts with both pCRP and mCRP.
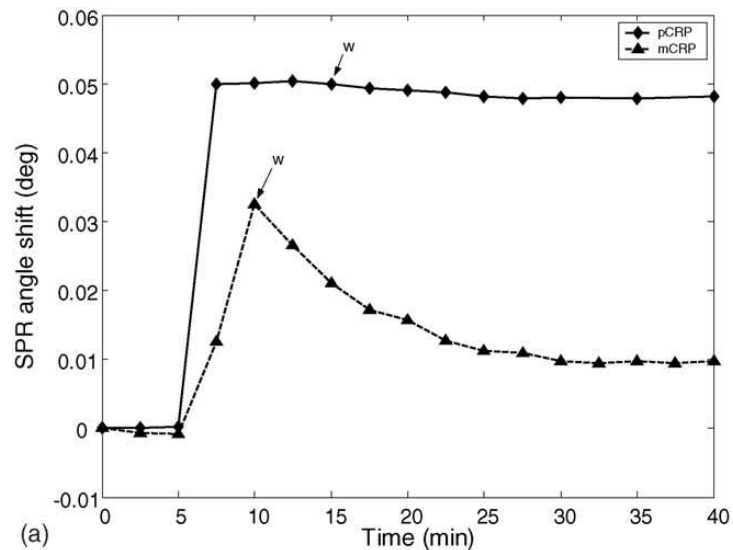
Figure 2.14 SPR sensorgram trace of antibody-antigen interaction of Mab C8 against pCRP and mCRP (Hu et al., 2006). Reprinted from Biosensors and Bioelectronics, 21, W.P. Hu, H.-Y. Hsu, A. Chiou, K.Y. Tseng, H.-Y. Lin, G.L. Chang, and S.-J. Chen, Immunodetection of Pentamer and Modified C-reactive Protein Using Surface Plasmon Resonance Biosensing, 1631-1637, 2006, with permission from Elsevier.

Based on the results, the biosensor has the ability to be used in clinical applications for the detection of CRP at clinical concentrations. However, it is noted that when compared with the high sensitivity CRP assay that has the lowest detection limit, this biosensor does not perform better but does rival other assay methods, such as enzyme-linked immunosorbent assay (ELISA).

SPR biosensors have also been studied and used for the detection of particular Alzheimer's disease biomarkers. One example is a multichannel SPR biosensor for the detection of 17beta-hydroxysteroid dehydrogenase type 10 (17β-HSD10), a biomarker that is a possible target for Alzheimer's disease diagnostics (Hegnerova et al., 2009). This sensor uses a self-assembled monolayer for the immobilization of biorecognition components against 17β-HSD10. The results show the sensor can detect 17β-HSD10 enzyme at ng/ml levels in artificial cerebrospinal fluid. Further studies will need to be performed to test the sensors detection capabilities in human cerebrospinal fluid.

2.2.1.2 Fiber Optic SPR Sensors

Another subclass of optical biosensors is fiber optic SPR biosensors. This subclass of optic sensor has gained popularity recently and has been investigated more extensively due to its ability to effectively handle measurement situations that other, more conventional sensors cannot handle, such as sensing in low sample volumes and portability. These biosensors involve the binding of a target analyte to the biological recognition component, which causes variation in the refractive index of the absorbed layers at the metal surface. All types of fiber optic SPR biosensors, which includes immunoassay, DNA, enzyme and living cell, rely on this mechanism (Liang et al., 2016).

In contrast to SPR biosensors, fiber optic SPR biosensors incorporate optical fiber that consists of a core that can replace components, such as a prism, in the sensing system. A schematic of a typical fiber optic SPR sensor is shown in Figure 2.15.
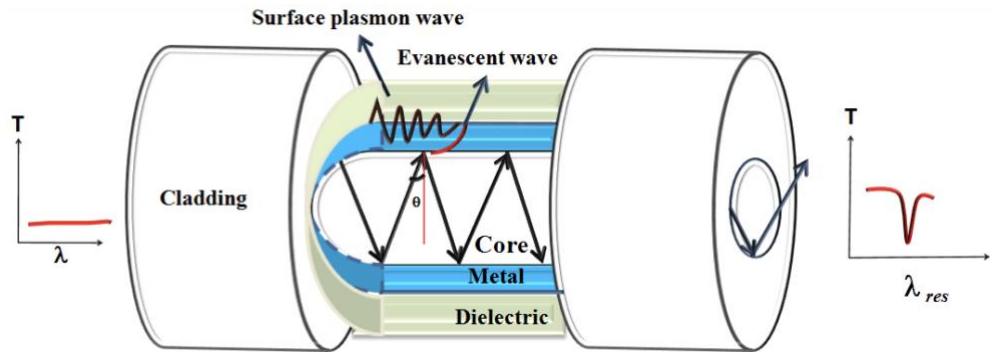
Figure 2.15 Schematic of a typical fiber optic SPR sensor with straight probe design (Gupta et al., 2016). (https://creativecommons.org/licenses/by/4.0/legalcode) (no changes made)

Although different, a fiber optic SPR biosensor follows the same basic principles involving the fundamentals of SPW and the SPR biosensor design that was discussed previously. In the case of a fiber optic SPR biosensor, the prism is replaced by the core of an optical fiber. Total internal reflection is the method of light transmission in optical fibers. The total internal reflection (TIR) of the guided ray at the core-cladding interface lends to the light guidance of the evanescent wave in the optical fiber (Gupta and Verma, 2009). The refractive index of the core (n_1) must be larger than the refractive index of the cladding (n_2), and the angle of incidence has to be larger than the critical angle for total internal reflection and propagation of light through the fiber to occur. The critical angle can be calculated mathematically by Snell's law (Marazuela and Moreno-Bondi, 2002):

$$\theta_C = \sin^{-1} n_2/n_1 \qquad\qquad (13)$$

These sensors are constructed by removing the cladding of the fiber and revealing the bare core of the sensing section. A metal coating and dielectric region is then used to coat the section. Guided rays are propelled into the fiber and produce evanescent waves, which stimulate surface plasmons at the metal-dielectric boundary (Gupta et al., 2016). Transmitted light is detected at the output side of the optical fiber at the resonance wavelength.

Measurement of resonance wavelength allows the examination of the interaction between the analyte and the sensing surface (Kant and Gupta, 2018). Obtaining experimental results involves analyzing SPR response curves that contain light intensity data at given wavelengths for analyte concentrations. The resonance wavelengths (dip in the curve) can then be determined and plotted against analyte concentration to obtain the calibration curve (Gupta et al., 2016, Kant and Gupta, 2018). An example of these results is shown in Figure 2.16.

These sensors are ideal for their simple optical setup that includes no electromagnetic interference. Other advantages include the capability for remote, in-situ and label-free sensing, low cost, high sensitivity, miniaturization ability, portability and compactness. Similarly to SPR optical biosensing, fiber optic SPR has shallow penetration depth, although this limitation is reduced with fiber optic SPR compared with SPR. These sensors have currently been used for monitoring artificially buffered samples and haven't been used for real clinical samples and medical diagnostics yet (Liang et al., 2016).

Similarly to SPR biosensors, fiber optic SPR biosensors have also been used to detect cardiac biomarkers. The cardiac biomarkers detected are BNP, cTnl, Mg, CRP, nerve growth factor (NGF), and IL-6 (Qureshi et al., 2012). Tang et al. (2007) developed

and tested a fiber optic immunobiosensor for point-of-care analysis of human plasma NGF. NGF is a biomarker that is indicative of cardiac arrhythmia and has been used for CVD diagnosis and projection. Identical tests were performed with both the biosensor and the standardly used and accepted ELISA method to provide a comparison between the two modalities. The fiber optic immunobiosensor had a faster response time than ELISA and was able to quickly quantify (within 5 minutes) physiological concentrations of NGF in buffer and human blood plasma samples. The data accuracy was comparable between the two methods, making the sensor a promising point-of-care option that can be utilized for detection of NGF and other clinically noteworthy cardiac biomarkers.

It is hypothesized that a substantial drop in the synthesis of acetylcholine is linked to the cause of Alzheimer's disease. Based on this, a fiber optic SPR based acetylcholine biosensor was created to aid in the diagnosis of Alzheimer's disease (Kant and Gupta, 2018). This sensor functions by creating a sensing surface that is comprised of tantalum (v) oxide (Ta_2O_5) nanoflakes functionalized with acetylcholinesterase enzyme. This design proved to be advantageous in many aspects, such as compactness, ease of use, cost efficiency, and ability for remote sensing. SPR response curves were generated for different concentrations of acetylcholine, shown in Figure 2.16 (left). The resonance wavelength values were determined from these curves and plotted against acetylcholine concentration to form the calibration curve, shown in Figure 2.16 (right).
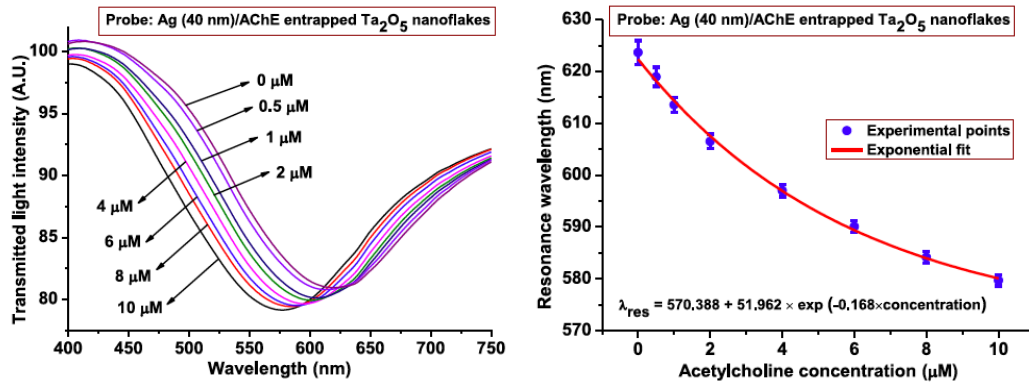
Figure 2.16 SPR response curves for range of acetylcholine concentrations (left) and calibration curve showing resonance wavelength variation vs. acetylcholine concentration (right) (Kant and Gupta, 2018). © 2018 IEEE

This sensor was also optimized for high sensitivity and high selectivity towards acetylcholine. It presents a LOD value of 38 nM, which is reported to outperform other detection techniques for acetylcholine. This experimental design was performed in a lab, and although the pH was set to mimic blood pH value, further testing may need to be performed to test the viability in true clinical applications.

2.2.2 Mechanical Biosensors

Mechanical biosensors provide a method of measurement that is rapid and can produce sensitive measurements, while requiring only limited sample processing. However, although mechanical biosensors are rapid, they are not easily reproduced. There are two main techniques used for mechanical biosensors: quartz crystal microbalances (QCM) and cantilever (Figure 2.17).

35
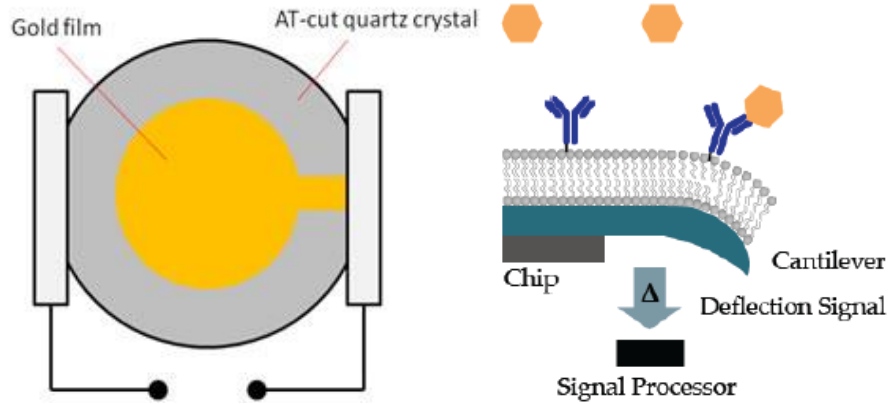
Figure 2.17 (a) schematic of a QCM chip (http://biosensingusa.com/technical-notes/technical-note-103-surface-plasmon-resonance-v-quartz-crystal-microbalance/) (b) schematic of a cantilever configuration (Kubicek-Sutherland et al., 2017). (https://creativecommons.org/licenses/by/4.0/legalcode) (no changes made)

QCM detects resonance frequency changes on the surface due to mass increase from analyte binding. Cantilever technique involves a receptor-functionalized microcantilever that is sensitive to the specific biomolecule. Mechanical bending is measured upon binding of this microcantilever with the target molecule (Kubicek-Sutherland et al., 2017).

A QCM consists of a quartz crystal, a gold electrode, and connecting metal wires. The quartz crystal is placed between two electrodes, creating an electric field that produces a mechanical oscillation in the crystal. The frequency change (Δf) that occurs due to change in mass (Δm) is governed by the following Sauerbrey equation:

$$\Delta f = \frac{-2\Delta m n f_0^2}{A\sqrt{\mu\rho}} \qquad (\,14\,)$$

where n is the overtone number, f_0 is the base resonant frequency of the crystal before the mass change, A is the area, μ is the shear modulus of quartz, and ρ is the density of quartz. From this equation it can be seen that an increase in mass corresponds to a decrease in frequency (Wang, 2000).

For use in the cantilever method, these small cantilevers can be surface-stress sensors or dynamic-mode sensors (Arlett et al., 2007). The surface-stress mechanical biosensor measures the quasistatic deflection caused by the binding of biomolecules to functional groups located on the surface of the sensor. One way that the deflection can be measured is by the reflection of a laser beam off the cantilever. The equation that governs the relationship between surface stress and deflection is given by Stoney's formula:

$$\Delta\sigma = \frac{Et^2}{3(1-v)L^2}\Delta z \qquad (15)$$

where Δz is the cantilever deflection, E is the elasticity modulus, v is the Poisson ratio, t is the thickness of the cantilever and L is the effective length, measured as the distance from the base of the cantilever to the point where the deflection is read out by the laser (Fritz, 2008). Molecular adsorption onto the surface creates surface stress and causes deflection. This surface stress is proportional to the analyte concentration that is adsorbed to the surface (Ji and Armon, 2010). The dynamic-mode, or resonance mode, mechanical biosensor is not quasistatic. Instead, oscillation occurs with resonance frequency that changes when molecules land on the cantilever. For instance, when mass is added the resonance frequency is lowered. The basic resonance frequency of the cantilever is modeled like the behavior of a harmonic oscillator, given by:

$$f = \frac{1}{2\pi}\sqrt{\frac{k_{spring}}{m^*}} \qquad (16)$$

where k_{spring} is the spring constant and m^* is the effective mass that considers the cantilever geometry and mass distribution along the cantilever (Fritz, 2008). This type of cantilever allows variance in the operating environment and mode. For example, these can be used in humid environments and for continuous operation (Arlett et al., 2007). A

disadvantage to the cantilever method is that it usually functions in air samples only, instead of liquid (Kubicek-Sutherland et al., 2017). This makes this technique less valuable to biomarker detection in clinical applications.

The specific output signal of the cantilever biosensor depends on the technique used for detection. The detection of the deflection of the cantilever beam, caused by either a change in surface stress or resonance frequency, plays a part in all types. However, the method in which it is accomplished varies based on the sensor design. Commonly used techniques include measuring the optical beam deflection (changes in reflection angle of optical beam), piezoresistivity (changes in resistivity caused by applied strain), piezoelectricity (changes in voltage produced by material under mechanical stress), interferometry (changes in refractive index) and capacitance (measurement of cantilever displacement) (Alvarez et al., 2008). An example of a piezoresistive microcantilever biosensor and the transduction techniques used is presented later.

Some other types of mechanical biosensors include whispering-gallery microcavity (WGM), optical microring resonators (MRRs), and nanowire biosensors. Mechanical biosensors can be categorized into four groups depending on the relationship between the analyte and the sensor. Group one includes affinity-based assays, which use high specificity between the target and the functionalization at the surface. This is done to achieve very selective target identification and capture, such as between antigens and antibodies. Group two includes fingerprint assays, which identify a target through distinctive binding affinities to an ensemble of sensors. This depends on an assortment of less-selective functionalization layers. Group three includes separation-based assays, in which spatiotemporal separation of analytes is permitted due to chemical affinities between

immobilized species. Group four includes spectrometric assays, where identification is performed using the mass or optical properties of the target analyte (Arlett et al., 2007).

Mechanical biosensors have been used for the detection of cardiac biomarker CRP using self-sensing piezoresistive microcantilever sensors and antigen-antibody interaction (Wee et al., 2005). The experiment conducted by Wee et al. (2005) utilized the static mode or surface-stress method, and the piezoresistive microcantilever sensor allowed for electrical detection via surface stress changes of antigen-antibody specific binding. An internal and external half dc-bias Wheatstone bridge was measured to provide the electrical measurement of change in sensor resistance and was used to measure the piezoresistive induced voltage. Figure 2.18 shows the resulting piezoresistive response curves, that are a result of static deflection of the cantilevers, at different CRP concentrations. It is shown that the output voltage of the sensor was proportional to the concentration of CRP in solution.
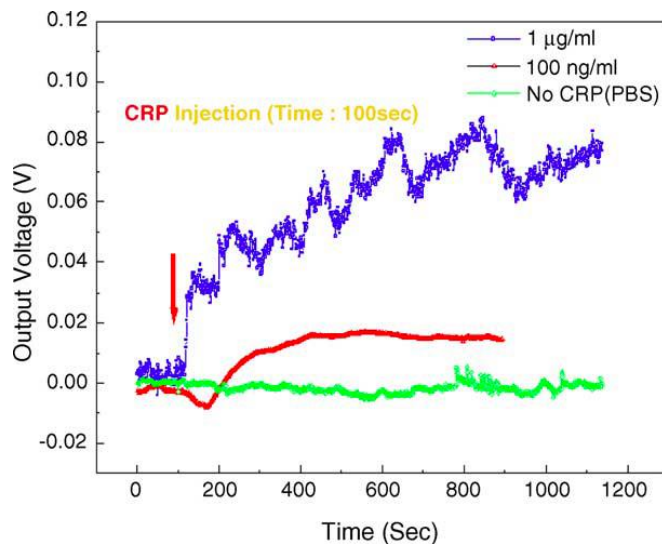
Figure 2.18 Output voltage as a function of CRP concentration (Wee et al., 2005). Reprinted from Biosensors and Bioelectronics, 20, K.W. Wee, G.Y. Kang, J. Park, J.Y. Kang, D.S. Yoon, J.H. Park, T.S. Kim, Novel Electrical Detection of Label-free Disease Marker Proteins Using Piezoresistive Self-sensing Micro-cantilevers, 1932-1938, 2005, with permission from Elsevier.

This suggested that the microcantilever sensor design is effective for the detection of CRP.

A NiCr strain gauge cantilever biosensor has been utilized for the detection of the addition of amyloid beta (Aβ)(1-40) protein in human serum (Taniguchi et al., 2017). Evidence has suggested that a crucial factor in the development of Alzheimer's disease is the interaction between Aβ and the cell membrane (Zhang et al., 2017). More specifically, the interaction with cerebral nerve cells and the buildup of Aβ on these cells. Using the cantilever microsensor design combined with a droplet-sealing structure, Taniguchi et al. (2017) were able to show improvements in this sensor by using a digital filtering procedure to eliminate external noise, and by incorporating cholesterol to suppress liposome and protein interactions in the human serum. They were able to conclude that with these additions the cantilever biosensor is able to detect low-concentrated Aβ in human serum.

2.2.3   Biosensors On-a-Chip

Biosensors on-a-chip is a technology that combines microfluidics, a lab-on-a-chip technology, with biosensors. Microfluidics can be combined with different biosensing platforms, such as electrochemical or optical, to create a more robust diagnostic tool. A microfluidic biosensor is a fluidic system that encompasses micro-sized channels to aid in the detection of a given target molecule. This type of biosensor encompasses two types of channel flow: pressure-driven flow and electrokinetic flow. Using an electric field instead of a pressure gradient may be preferable to drive channel flow since pressure-driven flow becomes more challenging as channel size decreases (Prakash et al., 2012). Reynolds number describes fluid flow and is given as:

$$Re = \frac{\rho d \upsilon}{\eta} \qquad (17)$$

where ρ is the fluid density, d is the characteristic length or dimension of the microchannel, υ is the flow rate of the fluid, and η is the fluid viscosity (Kaur et al., 2018). The concentration of target molecules and the speed of target molecule detection is governed by basic physics of mass transport and reaction time. The trade-off between detection speed and concentration has been investigated and is evident through different microfluidic designs that have developed over the years. A higher fluid velocity is required for a faster detection speed, however, the time required for the molecule to diffuse is the limiting factor. The characteristic time scale for the biosensor, t_c, is therefore expected to scale according to:

$$\frac{l_c^2}{D} \qquad (18)$$

where l_c is the characteristic length of the device and D is the diffusivity of the target molecule.

There are three different microfluidic systems: continuous flow, droplet-based, and digital microfluidic (DMF). Continuous flow systems can by pressure driven or electrokinetic and provide a motion of continuous fluid in micro-channels. Droplet-based systems are pressure driven and provide droplets in micro-channels using streams of immiscible fluids. DMF involves electrowetting on dielectric or dielectrophoresis and provides discrete droplets on an array of planar electrodes. These different systems are shown schematically in Figure 2.19.
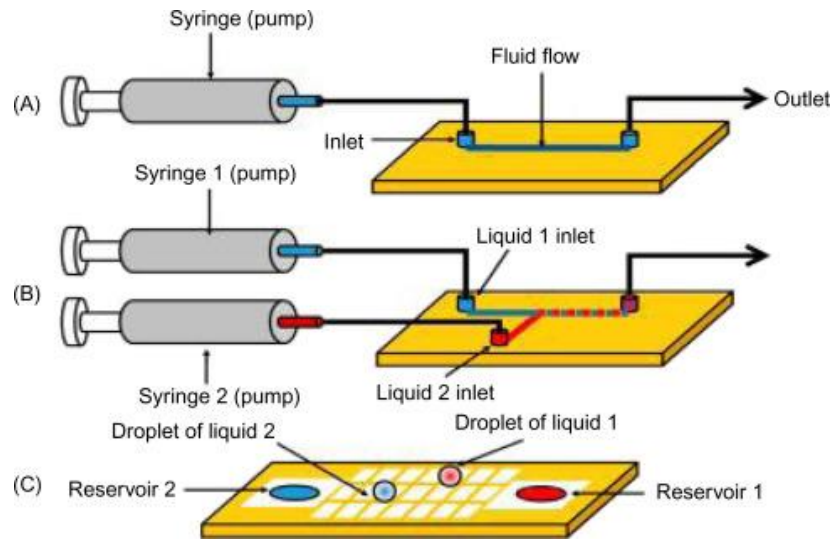
Figure 2.19 Schematic of three microfluidic systems (a) continuous; (b) drop-based; and (c) digital (Luka et al., 2015). (https://creativecommons.org/licenses/by/4.0/legalcode) (no changes made)

Each type of the three microfluidic systems presented provides integrated sensing applications for the three most common biological recognition elements used in microfluidic devices: enzymes, antibodies, and aptamers (Luka et al., 2015). As with all biosensors, the signal that results from the interaction between the analyte and the biological recognition element is modified by a transducer. However, the readout that occurs depends on the particular biosensor integration.

Microfluidic biosensors are most commonly made of silicone, glass or types of polymers (Prakash et al., 2012). Further, PDMS is the most popular material due to advantageous qualities such as biocompatibility, easy handling, and low cost (Kaur et al., 2018). Microfluidic designs allow for target molecule detection in small concentrations, which is beneficial for clinical use. This aspect is also beneficial since the use of small concentrations means a reduction in the use of costly reagents (Xu et al., 2018). Some other notable advantages include quicker diagnostics through the manipulation of the sensor geometry and highly sensitive real-time measurements that eliminate non-uniformity and

non-homogeneity. A few disadvantages of microfluidic biosensors include undesirable adsorption of non-specific molecules and interference from solutions (Prakash et al. 2012)(Kaur et al., 2018).

Microfluidic techniques have been used in conjunction with electrochemical biosensors to create a method for cholesterol monitoring (Kaur et al., 2018). This design utilizes Nickel Oxide (NiO) thin film as the material for the immobilization of cholesterol oxidase enzyme and PDMS for the microchannel composition. The two electrode, three microchannel biosensor was created on glass substrate using photolithography. Cyclic voltammetry and chronoamperometry measurements were performed. The device proved capable of a wide range of cholesterol detection with less sample consumption and high sensitivity. It also is capable of a lower detection limit of 0.10 mM. Diluted serum samples were used to validate the biosensor and proved its performance is accurate and comparable to commercially accepted methods. Amperometric data obtained from electrochemical studies is shown in Figure 2.20.
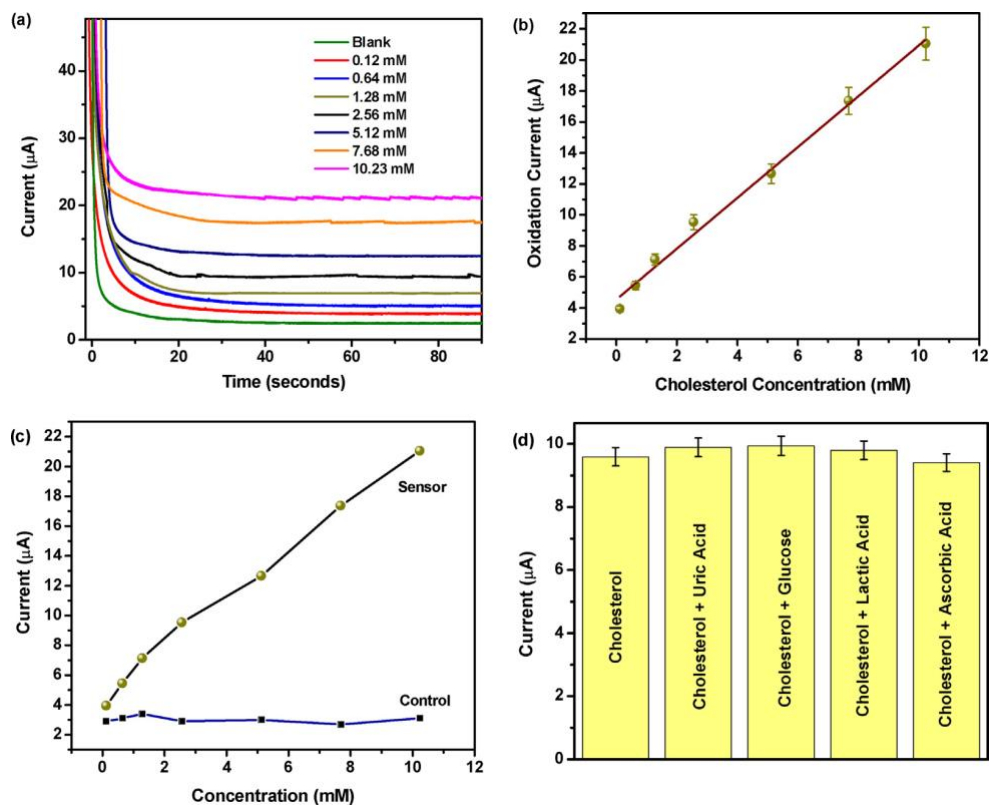
Figure 2.20 (a) amperometric curves as a function of cholesterol concentration (b) calibration curve (c) comparison to control (d) selectivity (Kaur et al., 2018). Reprinted from Sensors and Actuators B, 261, G. Kaur, M. Tomar, and V. Gupta, Development of a Microfluidic Electrochemical Biosensor: Prospect for Point-of-Care Cholesterol Monitoring, 260-466, 2018, with permission from Elsevier.

Interestingly, in recent years microfluidic biosensors have been coupled with smartphones to create smartphone-based microfluidic biosensors for point-of-care use. Research shows that these can provide accurate and rapid point-of-care detection. These also minimize downsides like cost, size and operational skill by the professional. These are still in the laboratory phase and present further research and challenges, such as the issue that miniaturization could decrease the accuracy and sensitivity compared to conventional testing instruments already developed (Xu et al., 2018).

Microfluidic biosensors allow for a wide range of designs and techniques. For example, Singh et al. (2019) and Mohammed and Desmulliez (2014) both present a

microfluidic system to detect CVD biomarker cardiac troponin I (cTnI). Singh et al. (2019) created a microfluidic biosensor using a soft lithography technique and integrated $Ni_3V_2O_8$ hollow-nanospheres that were modified with chitosan. This design proved to have high sensitivity and selectivity and a low limit of detection, with a LOD for cTnI of 5 pg/ml. Mohammed and Desmulliez (2014) created a microfluidic biosensor consisting of an autonomous capillary system with embedded optical components. This design proved to also provide high sensitivity, as well as advantages such as portability and low power consumption. However, the limit of detection was demonstrated to be 24 pg/ml for cTnI. This is still shown to be within the limits for clinical applications, but higher than the LOD of the previous design.

2.3   Unmet Needs and Possible Future Directions

Although biosensor research and development has made great strides and is consistently evolving, there are still gaps in the current research. One such gap is the medium and condition in which the biosensor is tested in. In order to confidently conclude that a biosensor is equipped for point-of-care use and in-situ monitoring, the testing of the biosensor must occur in such conditions. A shortcoming that we have seen throughout the literature is that many biosensors are tested only in a lab setting, often in artificial media. Going forward, testing would also need to be conducted in the required human media (blood, cerebral spinal fluid, etc.) and in a clinical, point-of-care setting. Human blood, for example, provides a complex environment for testing and requires the sensing method to exhibit a high level of selectivity towards the analyte or biomolecule being sensed. Having a biosensor that performs accurately in a complex environment would prove very beneficial, if not crucial, for clinical needs. Another issue we have seen throughout the

literature is the need to improve the long-term performance of the biosensor. This ties in to the stability of the sensor reducing over time and with use. This is not an issue for sensing methods that are intended as single use. However, for those methods that are intended to be reusable, the stability and performance over time needs to be examined in order to be confident that results after months of use are as accurate as the results seen on first use. Lastly, biosensors have shown to lack reproducibility in results. Variance in results from one sensor to another sensor of the exact same design is not acceptable in a research or clinical application and could lead to false results.

In all, biosensor research and development are progressing swiftly. Encouraging improvements have been made, however, an increase in sensitivity, selectivity, miniaturization and integration is still needed to successfully meet the requirements for a point-of-care biosensor device. Biosensors-on-a-chip, as previously discussed, provide a promising solution to achieve this goal. This lab-on-a-chip technology is relatively newer and less researched. More consideration and development should be done in this area of design to move towards more integrated systems with more complex biosensing capabilities.

Future research should also be performed in the areas of wearable biosensors and in-vivo biosensors. Success with these forms of biosensors would provide great value to the medical field, as it would allow for interactive, real-time data collection and analysis with the patient or individual wearing it. Recent glucose sensors for individuals with diabetes have paved the way for this technology. Now, this should be expanded on to reach more areas of diagnosis and detection.

For the detection of cholesterol in human blood, the most commonly used methods for detecting cholesterol concentration for diagnostics involve complex laboratory equipment and user training. A sensitive and easy to use electrochemical biosensor would provide the same ability as current methods but with simplicity and point-of-care capability. An ideal solution could be to develop a detection method that achieves two functions. One function being a biosensor designed with a bioreactor type of environment that would allow the study of drug effects on cholesterol concentration, and the second function being in vivo detection of cholesterol.

New biomarkers are being explored for the diagnosis and understanding of Alzheimer's disease. One such biomarker is amylin production and hyperamylinemia. Based on research done by Jackson et al. (2013), amylin was examined as a potential second amyloid in Alzheimer's disease. Accumulation of amylin in the brain was assessed for three groups: diabetic patients with vascular dementia or Alzheimer's disease, non-diabetic patients with Alzheimer's disease, and healthy controls of the same age. Interestingly they found that, in addition to patients with diabetes, amylin deposition was identified in brain parenchyma and blood vessels of non-diabetic patients with Alzheimer's disease. This suggested that the formation of amylin amyloid in the wall of cerebral blood vessels could result in the inability to get rid of AB from the brain. This failure could contribute to the cause of Alzheimer's disease. Our work on the design of a biosensor that can accurately distinguish and detect this biomarker will benefit this research by providing a rapid and accurate means of detection and monitoring.

The importance and necessity of portable, rapid and accurate biosensors is undoubtedly seen through the testing response for the novel and unfamiliar severe acute

respiratory syndrome coronavirus 2 (SARS-CoV-2), the coronavirus (COVID-19) taking place in our world today. This pandemic has been a shock to the world and due to its novelty, there were no prior approved testing methodologies, unlike the testing for a more common virus like influenza. This required emergency testing methods to be developed and implemented under an Emergency Use Authorization (EUA) by the FDA. One of the most common methods used is a rRT-PCR panel, however, the drawback of this method is long turn around rates. This has left patients waiting up to a week to get their results, potentially delaying their treatment and increasing their likelihood of infecting others without knowing. The situation is very fluid and new technologies are emerging daily (Emergency Use Authorization, 2020).

In response to the need for a rapid diagnostic test for COVID-19, companies and researchers are working to develop such methods. One of the technologies emerged from Cepheid, who has produced an automated molecular test that provides detection in approximately 45 minutes ("Xpert Xpress", 2020). Even more rapid, Abbott has developed a molecular point-of-care test that can deliver positive results in 5 minutes and negative results in 13 minutes ("Detect COVID-19", 2020). Both methods leverage the principles of each companies testing platform for influenza and RSV testing.

Many issues have been encountered with the testing capabilities developed for COVID-19. Some issues include the difficulty in handling the constant mutation of the virus, dealing with both false negative and false positive results, and the complexity of commonly used and approved methods for virus detection.

This pandemic is a prime example of the need for rapid and accurate biosensors for point-of-care detection and diagnostic use. Their creation for the detection of previous

coronavirus outbreaks, such as the electrochemical immunosensor proven for the detection of MERS-CoV, shows that biosensor application for the detection of such viruses is possible and extremely crucial (Layqah and Eissa, 2019).

2.4   Conclusion

Biosensors are a promising field for creating miniature, rapid, specific and reproducible detection systems that can be used in the research and clinical fields. In-situ diagnostics and point-of-care monitoring are essential for the medical system today. All of the sensor types discussed, electrochemical, optical, microfluidic, and mechanical, have had success and provide necessary advantages. However, further work needs to continue to optimize these biosensors and to minimize as many disadvantages as possible. For example, maintaining sensitivity and specificity with miniaturization, and improving biosensor longevity are problems that are continually being explored. It is also clear that while some biosensors are employed and tested in human serum, others are limited by only being tested artificially. Further testing needs to be performed to ensure the success and potential clinical use of these biosensor designs.

Biosensors have proven to be a reliable source for the detection of many different biomarkers related to cardiovascular disease and Alzheimer's disease. However, the research presented is just the beginning. Continued efforts need to be made to have these sensors optimized and able to be used as a standard in clinical monitoring and diagnosis. Additionally, other less common biomarkers are being discovered and researched that may have a large impact on the treatment of both diseases. Having the ability to detect such biomarkers quickly and efficiently through the use of biosensors could lead to significant breakthroughs in monitoring and treating such life-altering diseases.

CHAPTER 3. DEVELOPMENT OF A FLUIDIC, CHIP-BASED GLUCOSE
BIOSENSOR

3.1 Introduction

Based on the needs identified in chapter 2 regarding improving the capability of
biosensors for the detection and monitoring of different critical biomarkers, the goal of this
research was to combine microfluidics and a chip-based biosensor to develop a device for
the detection of glucose. A combined microfluidic biosensor platform provides many
desired advantages, one being the ability to perform continuous monitoring. This capability
presents a device that would meet current needs and improve biomarker monitoring within
both a clinical and research setting.

Currently, there are continuous glucose monitors (CGM) on the market that are
used by individuals who have diabetes. According to the National Institute of Diabetes and
Digestive and Kidney Diseases (Russell, 2017), CGM devices are used by those with type
I diabetes, and rarely used by individuals with type II diabetes, as research is still being
done on how these devices would benefit those with type II. CGM devices also reportedly
need improvement in accuracy and ease of use, requiring a finger-stick glucose test twice
a day to compare results against a standard meter. It is also reported that CGM devices
can't be used as the only resource for treatment decisions, a finger-stick glucose test is still
required. Given all of this, CGM devices are a step in a positive direction, however, the
standard finger-stick glucose test is still used for treatment decisions, for persons with type
II diabetes, and present a cheaper alternative than the CGM (Russell, 2017). A microfluidic
glucose biosensor could provide another option to bridge these gaps by providing an

inexpensive, easy to use device that would allow for glucose monitoring by clinicians, while also providing an effective monitoring method for researchers.

To create a successful microfluidic glucose biosensor we took a continuous improvement approach by testing different concentration ranges and experimental setups to reach our final microfluidic design. This chapter first gives an overview of the electrodes used, along with the surface characterization performed. The biofunctionalization process is then described, followed by methods and results of glucose detection performed at high and low ranges of glucose concentration. The chapter concludes with the final microfluidic, chip-based platform design, covering the methods and results, followed by the longevity and robustness testing of the biosensor.

3.2   Screen Printed Electrodes

Three-electrode screen-printed electrodes (SPE) consisting of a ceramic base, silver reference electrode, gold working electrode and gold counter electrode were purchased from Metrohm USA, Inc. (Riverview, FL, USA). Two different models of the Metrohm SPE were purchased, each with a different temperature of gold screen-printed ink. The AT model SPE is made with gold ink that is cured using a high temperature process (~900°C), compared with the BT model SPE made with gold ink that is cured using a low temperature process (~150°C). SEM images provided by Metrohm of each of the working electrodes show the BT models have a rougher, more porous surface than the AT models (Figure 3.1).
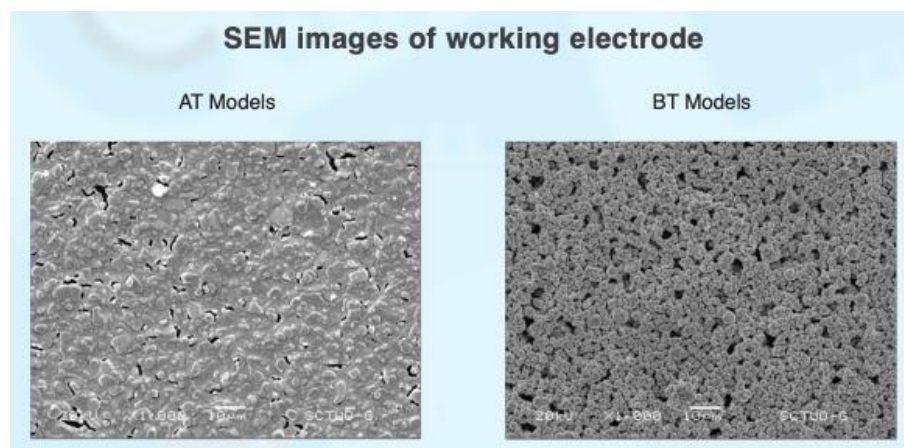
Figure 3.1 SEM images of the working electrode for the AT model SPE (high temperature cured gold) and the BT model SPE (low temperature cured gold) (Metrohm).

Further information provided by Metrohm explains that the behavior of the SPE's could be similar or differ depending on the application of use. To confirm, a surface characterization experiment to the gold working electrode on the SPE was performed by running cyclic voltammetry (CV) on each type of SPE. This experiment was performed by placing the chip sensor in a solution of phosphate buffered saline (PBS) containing 5mM potassium ferricyanide (Sigma-Aldrich, St. Louis, MO, USA). An external glass Ag/AgCl electrode and platinum gauze were used as the reference and counter electrodes, respectively. The gold working electrode on the SPE along with the external reference and counter electrodes were placed in a beaker containing the prepared solution with a stir bar. Stirring is to facilitate convective mass transport in addition to the slow diffusion. CV experiments were performed from +0.7 V to -0.15 V to +0.7V for 20 cycles. Four different scan rates were used: 50 mV/s, 100 mV/s, 150 mV/s, and 200 mV/s. The stir settings were adjusted to reach optimal results for each scan rate.

Figure 3.2 provides a sample of the raw data, showing the last cycle of the CV experiment for each model of SPE at 50 mV/s and 150 mV/s scan rate. The effect of scan

rate on current can be observed by comparing the two graphs. One characteristic that was consistent with expectations is that the standard potential doesn't change with a change in scan rate. The data also shows that as the scan rate was increased, the resulting current values also increased, which was to be expected. When the scan rate increases the overall time decreases, so an increase in scan rate results in a decrease in the diffusion layer, and vice versa. As summarized in Table 3.1, to examine this data further, the area under each CV curve was taken by using the trapezoidal rule. The area under the curve, or integration with respect to time, gives the surface charge (mC). The area under the curve was calculated between +0.2 V and +0.4 V for the 20th cycle of each CV curve. This potential range was chosen to eliminate the noise interference, especially below +0.2V. Additionally, the current differentials for the 20th cycle were calculated between the positive and negative ends of each curve by taking the difference of current values at +0.7V and -0.15V.

AT vs. BT at 50 mV/s Scan Rate
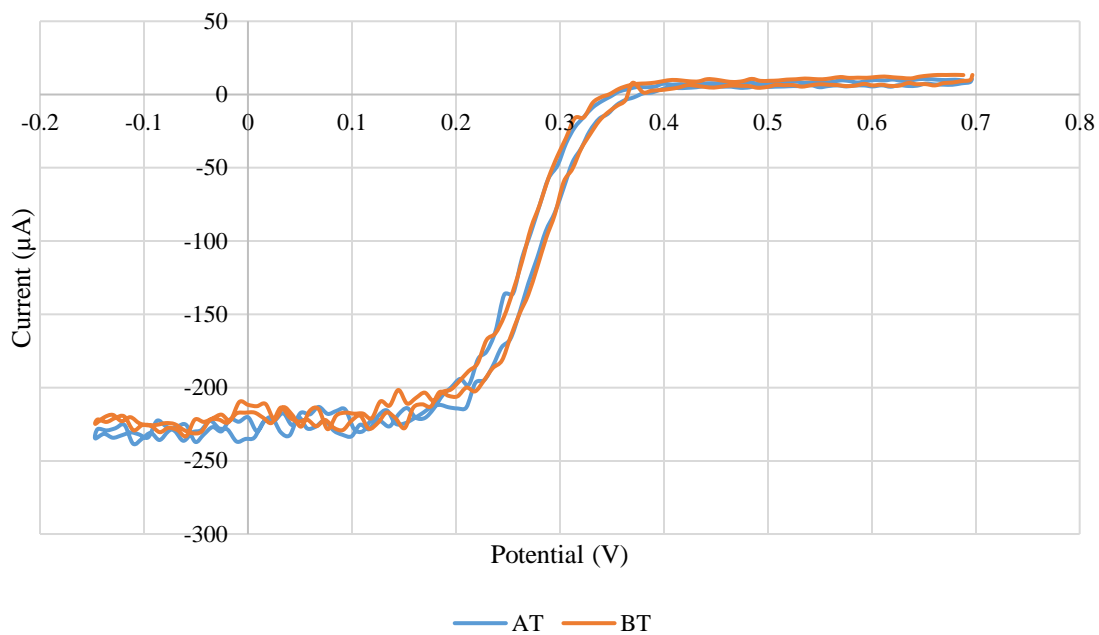
AT vs. BT at 150 mV/s Scan Rate
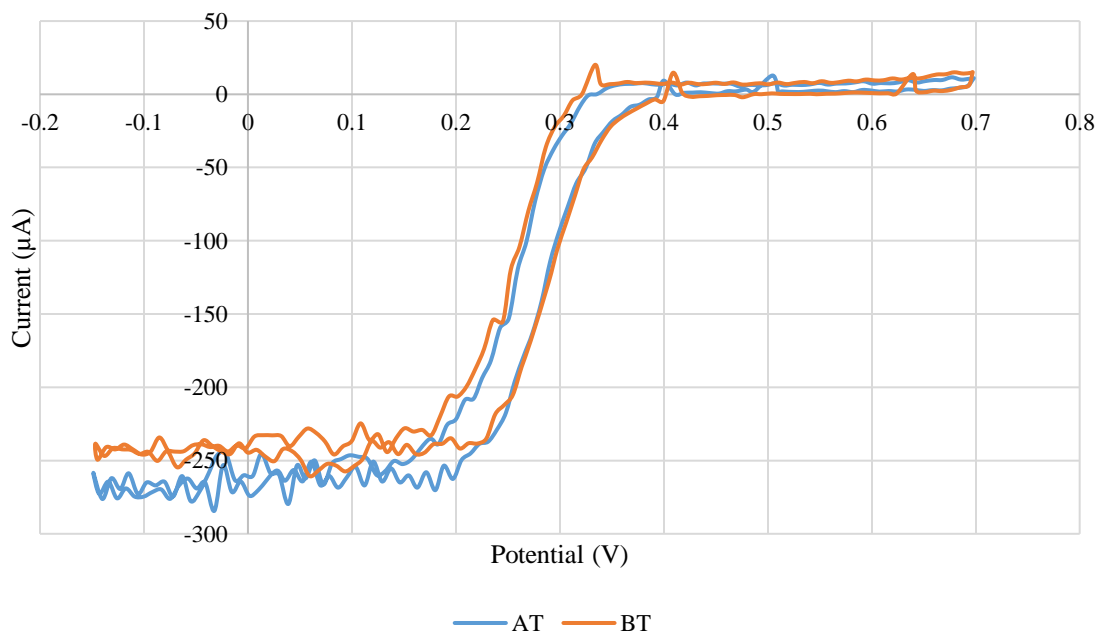
Figure 3.2 Sample of cyclic voltammetry data for AT and BT model SPE at 50 mV/s and 150 mV/s scan rates. Curves shown represent the last cycle of the cyclic voltammetry experiment.

Scan Rate (mV/s) / Sensor Model	Surface Charge 1 (mC)	Surface Charge 2 (mC)	Surface Charge 3 (mC)	Mean Surface Charge (mC)	Surface Charge Stdev (mC)	Mean Differential (mA)	Differential Stdev (mA)
50 / AT	0.1091	0.1132	0.1175	0.1133	0.0042	0.2457	0.0070
50 / BT	0.1130	0.1203	0.1166	0.1166	0.0036	0.2367	0.0068
100 / AT	0.0754	0.0732	0.0782	0.0756	0.0025	0.2507	0.0063
100 / BT	0.0718	0.0777	0.0731	0.0742	0.0031	0.1854	0.0195
150 / AT	0.0588	0.0585	0.0657	0.0610	0.0040	0.2706	0.0010
150 / BT	0.0737	0.0725	0.0765	0.0742	0.0020	0.2620	0.0073
200 / AT	0.0687	0.0614	0.0711	0.0671	0.0051	0.2906	0.0052
200 / BT	0.0630	0.0732	0.0731	0.0699	0.0059	0.2844	0.0097

Table 3.1 Data obtained from cyclic voltammetry experiments performed on bare AT & BT working electrodes. Three experiments were performed at each scan rate and the mean area value was calculated using the 20th cycle. The mean differential at the 20th cycle is given for each scan rate & model.

The data shows that at 50 mV/s, 150 mV/s, and 200 mV/s the BT model has a slightly larger surface charge, inferred from a larger area under the curve, and at 100 mV/s the AT model has a slightly larger surface charge. The instance at 100 mV/s presents an outlier to the observed trend. The surface charge can then be divided by the surface area of the working electrode to determine the charge density. The diameter of the circle working electrode is 4 mm, which provides a surface area of 12.57 mm^2. The resulting charge density values are given in Table 3.2.

Scan Rate / Model	50 / AT	50 / BT	100 / AT	100 / BT	150 / AT	150 / BT	200 / AT	200 / BT
Charge Density Run 1 (mC/mm^2)	0.0087	0.0090	0.0060	0.0057	0.0047	0.0059	0.0055	0.0050
Charge Density Run 2 (mC/mm^2)	0.0090	0.0096	0.0058	0.0062	0.0047	0.0058	0.0049	0.0058
Charge Density Run 3 (mC/mm^2)	0.0093	0.0093	0.0062	0.0058	0.0052	0.0061	0.0057	0.0058
Mean Charge Density (mC/mm^2)	0.0090	0.0093	0.0060	0.0059	0.0049	0.0059	0.0053	0.0056
Stdev (mC/mm^2)	0.0003	0.0003	0.0002	0.0002	0.0003	0.0002	0.0004	0.0005

Table 3.2 Charge density values at each scan rate for AT & BT model. Values calculated by dividing the area under the CV curve by the surface area of the working electrode.

The charge density data can be analyzed to distinguish differences between the surface of the AT vs. BT working electrode. Although both electrodes measure 4 mm in diameter, the porous composition of the BT electrode could provide slightly more working surface compared to the smoother AT electrode surface. A two-tailed *t*-test with α=0.05 was utilized to determine if a significant difference exists between the two surfaces based on the charge density at each scan rate. At a scan rate of 150 mV/s a statistically significant difference is shown with a p-value of 0.007, which is less than 0.05. At a scan rate of 50 mV/s, 100 mV/s, and 200 mV/s, the difference is not statistically significant, with p-values of 0.353, 0.582, and 0.584, respectively. The effect the surface has on the sensor biofunctionalization and detection performance will be examined through biomarker detection experiments.

3.3 Sensor Biofunctionalization

Prior to use each sensor was cleaned using the RCA-1 method, which involves the removal of organic contaminants using a 5:1:1 solution of DI water, ammonium hydroxide (Sigma-Aldrich, St. Louis, MO, USA) and hydrogen peroxide (Sigma-Aldrich, St. Louis, MO, USA). After cleaning, the sensor is rinsed in DI water, dried and prepared for the biofunctionalization steps. The enzymatic biofunctionalization process involves glucose oxidase (GOx) being functionalized on the working electrode through the electropolymerization of pyrrole. Conceptually, a positive potential is applied to the system to pull electrons away and facilitate the pyrrole to polypyrrole reaction that is required. Visually, this process is shown in Figure 3.3. This process was performed using two different methods, first using a beaker then using a PDMS well. The PDMS well provided necessary improvements for the electropolymerization process, which will be discussed.
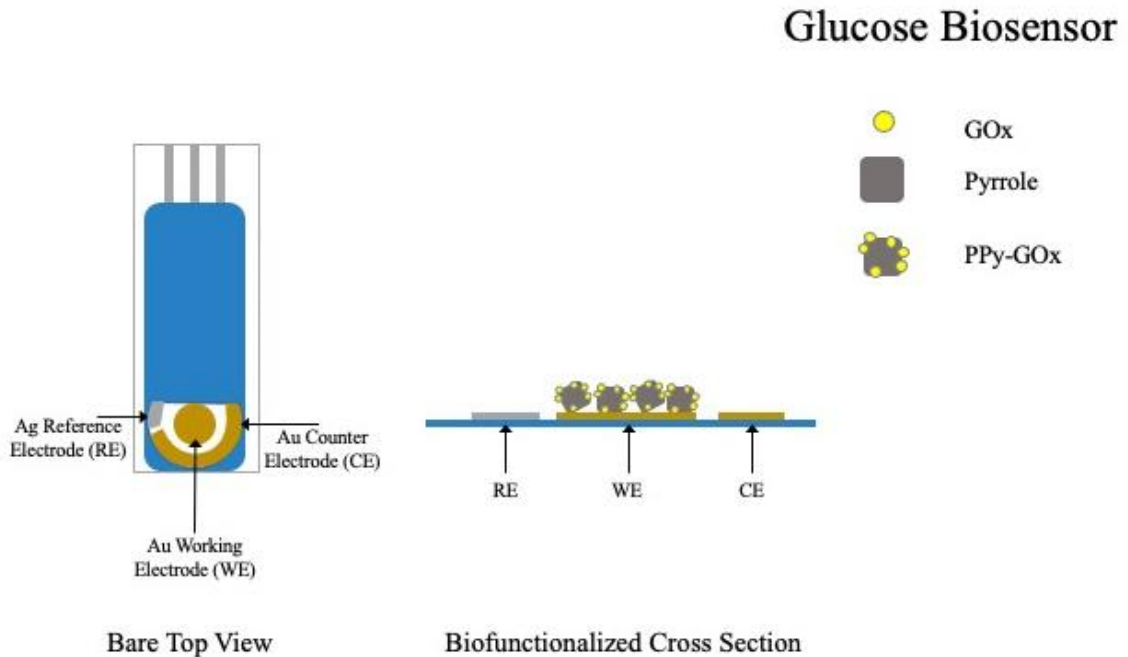
Figure 3.3 Schematic of the biofunctionalization process for the glucose detection sensor.

Initially, this process was performed in a 10 mL beaker with a two-electrode setup, using the gold working electrode on the sensor and an external platinum gauze strip as the counter electrode. The on-chip counter and reference electrodes were taped over with masking tape to prevent any unwanted contact with the electropolymerization solution. This was performed galvanostatically using a Keithley 2450 SourceMeter SMU (Tektronix, Beaverton, OR, USA). The sensor was placed inside the beaker containing solution and chronopotentiometry experiments were carried out in 0.1M PBS containing 0.1 mM pyrrole (VWR, Batavia, IL, USA) and 1 mg/ml GOx (Sigma-Aldrich, St. Louis, MO, USA). The deposition current of 10 µA was applied for 7.5 minutes (450 seconds) for AT electrodes and 4 minutes (240 seconds) for BT electrodes.

The time needed for functionalization was determined by performing optimization experiments on each sensor model. This was completed by applying different timed amounts of deposition, testing the glucose detection response of each sensor, and then comparing the slopes and R^2 values of each corresponding calibration curve. The condition that produced the highest slope was chosen as optimal. This data is presented in Table 3.3. The applied current was kept constant at 10 µA and the initial times performed were 7, 13 and 19 minutes. The BT sensor was later tested further with less time since it was observed that deposition occurred more quickly than on the AT sensor. This observation was to be expected based on the different surface properties of the working electrode surfaces. Through this optimization the previously stated electropolymerization times of 7.5 minutes for AT electrodes and 4 minutes for BT electrodes was determined.

	AT (7 min.)	AT (13 min.)	AT (19 min.)	BT (7 min.)	BT (13 min.)	BT (19 min.)
Slope (μA/M)	2	1	1	3	2	1
R^2	0.9879	0.9545	0.9973	0.9665	0.7778	0.8801

Table 3.3 Optimization data for the AT and BT model sensor for the working electrode electropolymerization. Slope and R^2 values obtained from glucose detection testing of functionalized sensors.

To improve on this initial setup, a PDMS well was created that contained a circular well with a diameter slightly larger than the diameter of the on-chip working electrode. This design is shown in Figure 3.4. This design allows for solution to be applied only on the working electrode without having to tape over the on-chip reference and counter electrodes, preventing any tape residue or surface disturbance. This method also reduces the amount of solution needed to perform the functionalization.
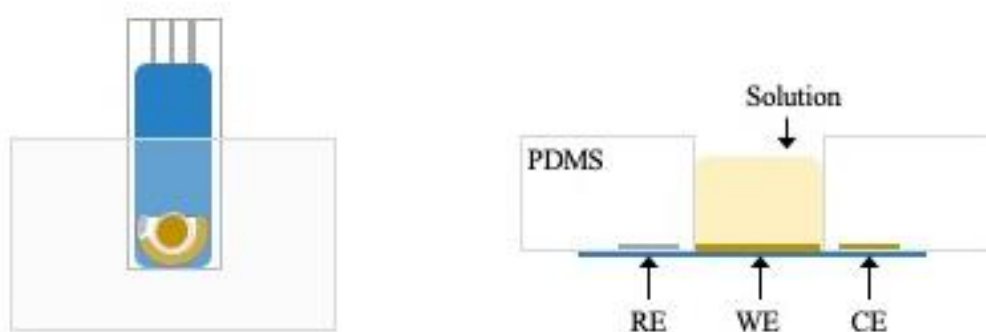
Figure 3.4 The left schematic shows the PDMS well used for biofunctionalization of the sensor. The right schematic provides a cross sectional view of the design.

The PDMS well was clamped onto the sensor and a syringe with a blunt needle placed into the well. The needle tip was positioned close to the working electrode without making contact to the surface. The needle tip was also wrapped in conductive tape, which is then connected to the machine, allowing the metal needle to function as the counter electrode

for the two-electrode system setup. The deposition solution was pumped from the syringe into the well, and the solution was removed from the well and replaced periodically throughout the experiment. For this method, chronopotentiometry experiments were carried out in 0.1 M PBS containing 0.2 mM pyrrole and 1.97 mg/mL GOx. The deposition current of 10 µA was applied for 6 minutes (360 seconds) for AT electrodes and 5 minutes (300 seconds) for BT electrodes. These values were based off of visual observations and previously optimized times.

Functionalized sensors were stored dry in the refrigerator at 4°C. The storage conditions of the sensors were optimized and this condition proved best compared with sensor storage in PBS at room temperature and sensor storage in PBS at 4°C. The success of the storage conditions was based on the visual condition of the silver reference electrode and the rate of degradation observed in glucose detection results after storage.

3.4 Methods for Glucose Detection

A positive potential was applied to the working electrode and an electron transfer between the electrode and GOx occurs due to the redox reaction between GOx and glucose. As shown in the following reaction, glucose is catalyzed by GOx, which leads to O_2 consumption and H_2O_2 production:

$$Glucose + \ O_2 + \ H_2O \ \xrightarrow{GOx} Gluconic \ acid + \ H_2O_2$$
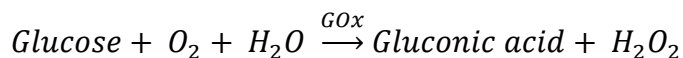
To assess the sensing capabilities of the biofunctionalized glucose detection sensor, step-wise tests were performed at increasing concentrations of glucose. A three-electrode setup was utilized, consisting of the silver reference, gold working, and gold counter electrodes on the Metrohm screen-printed electrode. Four different methods were tested to

perform the glucose detection experiments: low glucose concentration range, high glucose concentration range, manual solution flow, and a microfluidic, chip-based platform.

3.4.1   Low Glucose Concentration Range

Testing was performed to determine the detection capabilities of the sensor within a low concentration range of glucose. To facilitate this, an experimental setup using a beaker containing solution was utilized. The biofunctionalized sensor was placed in the 10 mL beaker containing a 5 mL solution of phosphate buffered saline (PBS) (Sigma-Aldrich, St. Louis, MO, USA) with 3 mM p-benzoquinone (Sigma-Aldrich, St. Louis, MO, USA), included as a mediator. Amperometric current responses were collected via the chronoamperometry technique on the PARSTAT MC multichannel potentiostat (AMETEK, Berwyn, PA, USA). The biosensor was allowed to equilibrate in solution via pre-conditioning for 30 minutes. The experiment was then performed at an electrode potential of +0.35 V versus reference for a total of 25 minutes. After stabilization of the current at 15 minutes (900 seconds), a controlled amount of glucose from a 1 M glucose stock solution was added to the PBS / p-benzoquinone solution. Consecutive additions of glucose were made each minute after for a total of 10 glucose additions. Manual stirring was performed to promote solution homogenization.

3.4.2   High Glucose Concentration Range

Testing was also performed to determine the detection capabilities of the sensor within a high concentration range of glucose. To examine this, a lower amount of solution was able to be used. Based on this, the biofunctionalized sensor was placed in one well of a 24-well plate with 1.5 mL solution of phosphate buffered saline (PBS) containing 3 mM

p-benzoquinone. Amperometric current responses were collected via the chronoamperometry technique on the PARSTAT MC multichannel potentiostat. The biosensor was allowed to equilibrate in solution via pre-conditioning for 30 minutes. The experiment was then performed at an electrode potential of +0.35 V versus reference for a total of 25 minutes. After stabilization of the current at 15 minutes (900 seconds), a controlled amount of glucose from a 1 M glucose stock solution was added to the PBS / p-benzoquinone solution. Consecutive additions of glucose were made each minute after for a total of 10 glucose additions. Manual stirring was performed to promote solution homogenization.

3.4.3   Manual Solution Flow

Before moving to a microfluidic design, the response of the sensor to flow of solution across the electrodes was experimented with manually. This method utilized the capacity of the sensor to hold a drop of liquid covering the electrodes. The solution volume chosen was 70 μL, as this amount could be held comfortably over the electrodes without overflow. To perform the detection experiments, the sensor was secured to a flat surface and 70 μL of solution composed of phosphate buffered saline (PBS) containing 3 mM p-benzoquinone was pipetted onto the surface. The biosensor was allowed to equilibrate in solution via pre-conditioning for 5 minutes. The pre-conditioning time was shortened due to the reduced amount of solution. The experiment was then performed at an electrode potential of +0.35 V versus reference for a total of 15 minutes. After stabilization of the current at 5 minutes (300 seconds), a new 70 μL addition was made using one pipette, while a second pipette was concurrently removing the previous solution. The addition

62

solutions consisted of pre-determined amounts of PBS, p-benzoquinone and glucose and were added to the electrodes starting from low concentration of glucose to high. These solutions were made according to Table 3.4. Consecutive additions were made each minute for a total of 10 additions.

Addition Number	PBS / p-benzoquinone soln. (mL)	Glucose (µL)	Molarity (mol/L)	Clinical (mg/dL)
1	1.5	5	0.0033	59.8
2	1.5	7	0.0046	83.6
3	1.5	9	0.0060	107.4
4	1.5	11	0.0073	131
5	1.5	15	0.0099	178.2
6	1.5	20	0.0132	236.8
7	1.5	25	0.0164	295.1
8	1.5	35	0.0228	410.4
9	1.5	45	0.0291	524.3
10	1.5	50	0.0323	580.7

Table 3.4 Amount of each solution and the corresponding molarity and clinical value for each addition for glucose detection testing. The table shows the total amounts used to create each solution, with each addition number resulting in a different final volume to reach the desired molarity. However, the same volume was withdrawn from each prepared solution to be used for an addition.

3.4.4 Microfluidic, Chip Based Platform

After examining the detection capabilities of the sensor at low and high glucose concentrations and testing the sensor response to the flow of solution across the electrodes, the next step was to incorporate the sensor chip with a microfluidic platform. To do this, a PDMS microfluidic platform was designed and created in the lab. The design consists of an inlet well and inlet channel that flows into a dome that covers the sensor electrodes, and an outlet channel for solution to exit through. The inlet well, channels and dome are created using a 3D printer and PLA material. The 3D rendering of this design is shown in Figure 3.5.

Internal Structure of Microfluidic Platform
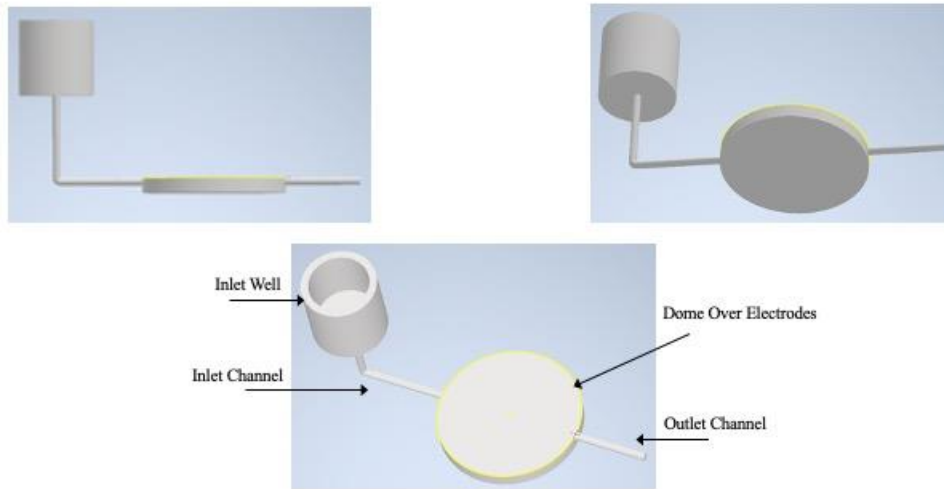
Figure 3.5 3D rendering of the internal structure of the microfluidic platform.

This material was chosen based on its ability to be dissolved out of the of PDMS using acetone. The PDMS was constructed using SYLGARD™ 184 Silicone Elastomer Kit and a 10:1 ratio of silicone elastomer base to elastomer curing agent, degassed in a centrifuge at 3200 rpm for 2 minutes. The entire platform was setup in a petri dish and PDMS was poured to cover all structures. After 48 hours of curing, the PDMS platform was extracted from the petri dish and the PLA structures were removed. A picture of the final PDMS component with sensor is shown in Figure 3.6.
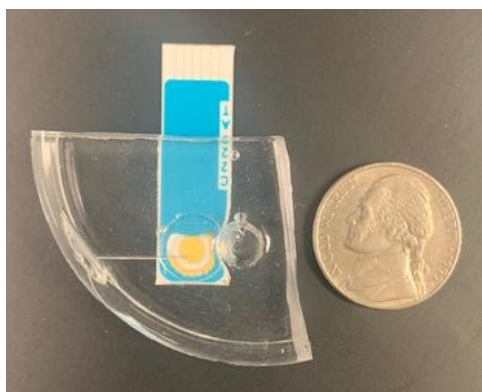
Figure 3.6 PDMS component after removal from petri dish and PLA dissolution. A nickel is shown for size reference.

A needle connected to tubing was inserted into the outlet channel and connected to a syringe pump. A schematic of the entire experimental setup, and a cross sectional view, is shown in Figure 3.7.
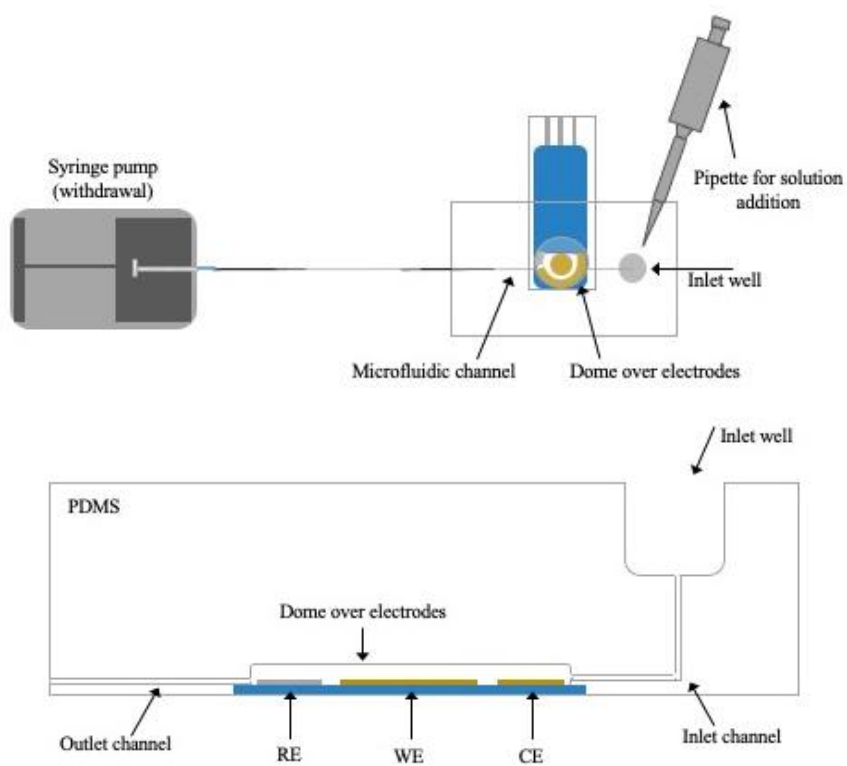
Figure 3.7 The top schematic shows the overall experimental setup for amperometric glucose detection. The bottom schematic shows a cross sectional view of the combined PDMS, chip based platform.

The withdrawal function of the syringe pump was used to pull solution through the microfluidic system at a rate of 0.1 mL/min. For detection experiments, the 10 solutions shown in Table 3.4 were made and used. Before the experiment, 100 μL of solution composed of phosphate buffered saline (PBS) containing 3 mM p-benzoquinone was pumped through the system, and the pump was paused when the well was emptied. The sensor was allowed to sit in solution for pre-conditioning for 5 minutes. The experiment was then performed at an electrode potential of +0.35 V versus reference for a total of 15 minutes. After stabilization of the current at 5 minutes (300 seconds), the first 100 μL addition was added into the well and the pump was started. Consecutive additions were added to the well every minute after for a total of 10 different additions.

3.5   Results & Discussion

All methods used for glucose detection proved the detection capability of the biosensor. However, as shown in the methods progression, continuous improvement was done to reach the microfluidic, chip-based platform that provides the most robust and desirable results.

3.5.1   Low Glucose Concentration Range

Utilizing a 10 mL beaker for the experimental setup to perform glucose detection experiments allowed for detection testing of the biosensor at lower concentrations of glucose, including within the physiological range of glucose levels, 3.9 – 7.1 mmol/L (70 – 130 mg/dL). Results proved the detection capabilities of the biosensor within this range, with good linearity, 0.9979 for the AT sensor and 0.9978 for the BT sensor. Visually, the raw data shows a large amount of noise, especially in the case of the AT sensor. This noise

was likely due to the larger amount of solution the biosensor was placed in, combined with the movement caused by manual stirring. To construct the calibration curve, the final current at each time segment was taken and plotted. Based on this, the sensitivity, given by the slope of each calibration curve, was higher for the AT sensor than the BT sensor in this case. The sensitivity was 0.04 µA/mM and 0.03 µA/mM for the AT and BT sensor, respectively.

Glucose Detection - Low Concentration Range - AT

Glucose Concentration vs Current - Low Concentration Range - AT

$y = 0.0405x + 0.311$
$R^2 = 0.9979$
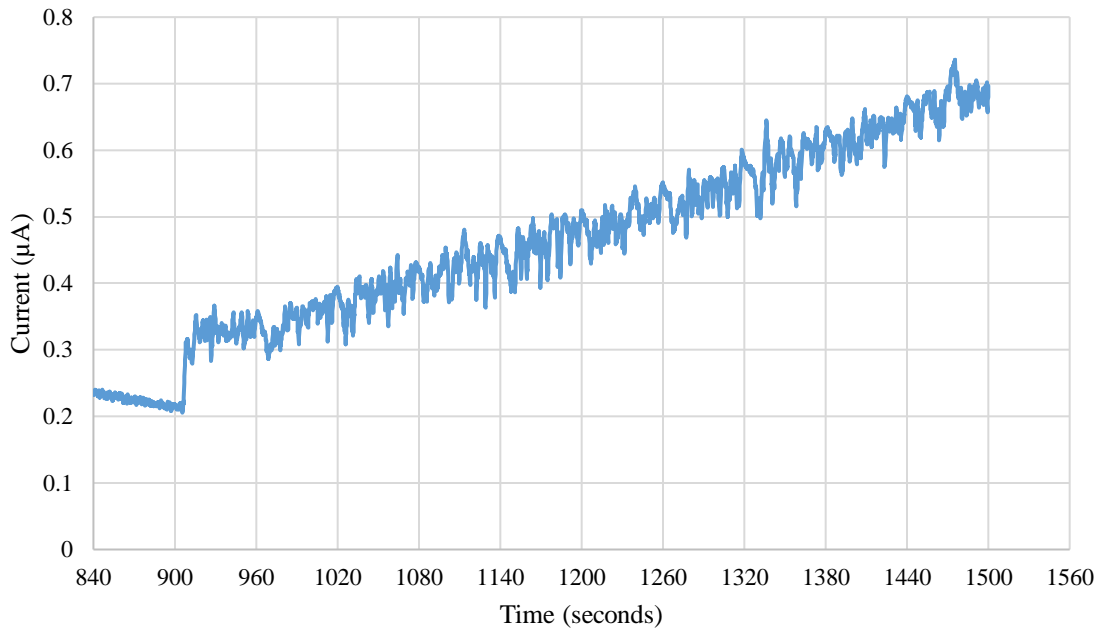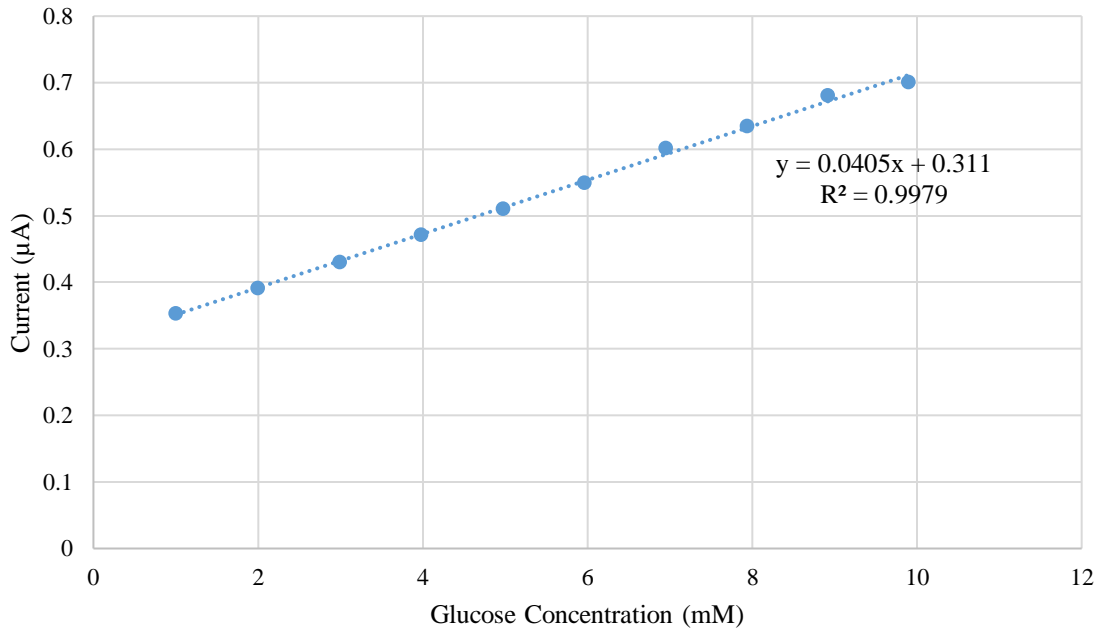
Figure 3.8 The top plot shows the raw data for AT sensor with glucose additions as a function of time. Additions began at 900 seconds and a controlled amount of 1M glucose stock solution was added every 60 seconds. The bottom plot shows the corresponding calibration curve.

Glucose Detection - Low Concentration Range - BT

Glucose Concentration vs Current - Low Concentration Range - BT

$y = 0.0287x + 0.2693$
$R^2 = 0.9978$
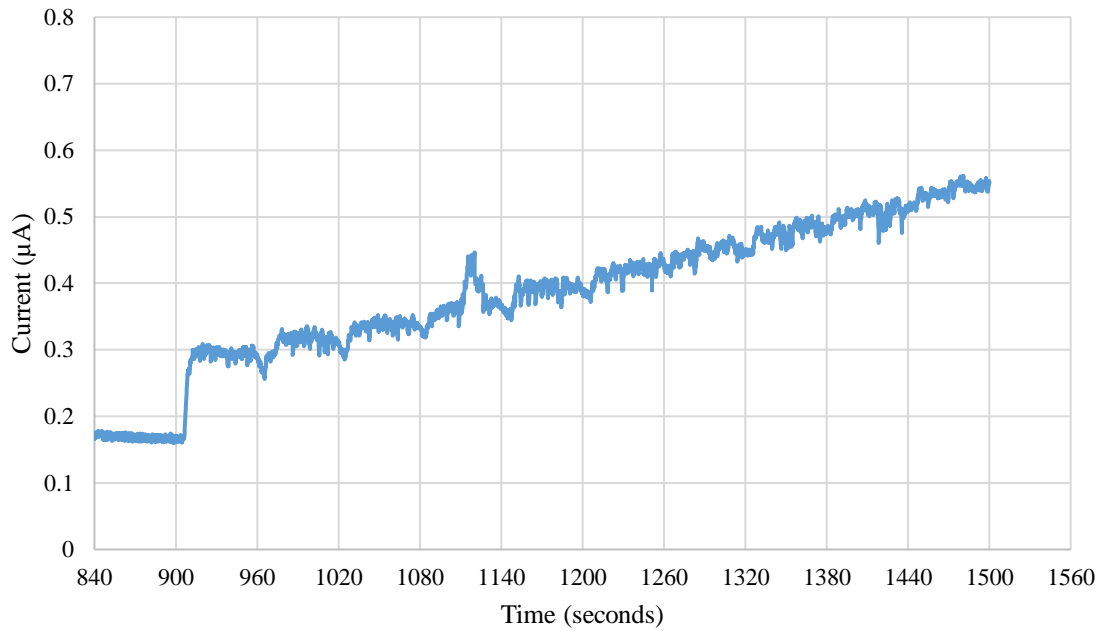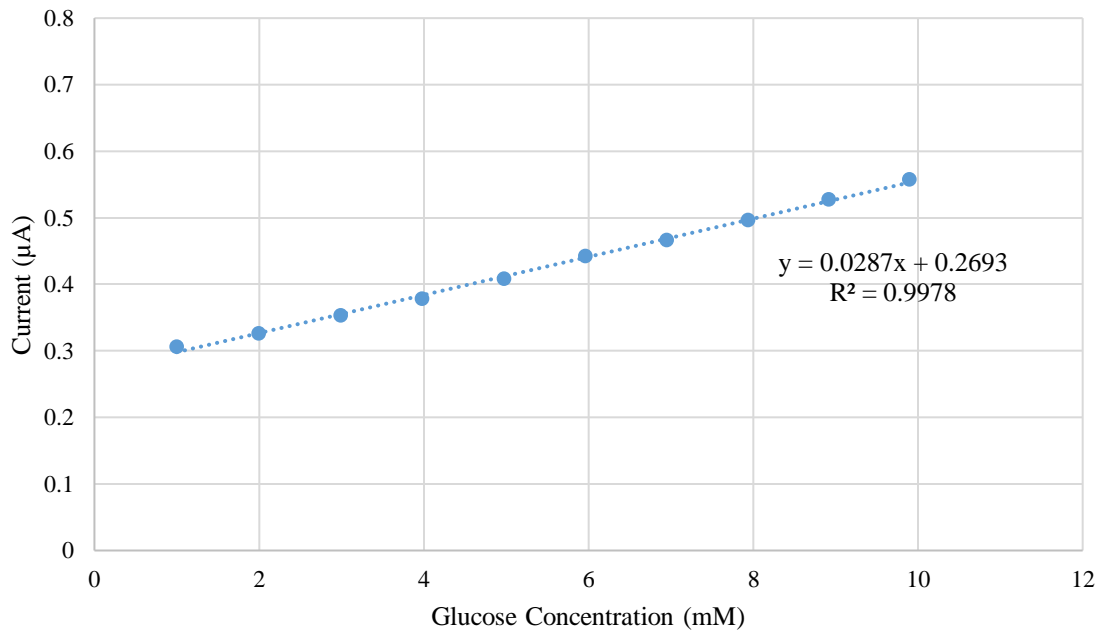
Figure 3.9 The top plot shows the raw data for BT sensor with glucose additions as a function of time. Additions began at 900 seconds and a controlled amount of 1M glucose stock solution was added every 60 seconds. The bottom plot shows the corresponding calibration curve.

3.5.2   High Glucose Concentration Range

As an effort to reduce the noise experienced using the beaker, as well as testing the detection capability of the sensor at higher glucose concentrations, the next step was using the 24-well plate. By using one well in a 24-well plate, the amount of solution needed to perform the experiments was reduced from 5 mL to 1.5 mL and glucose detection was performed at higher concentrations of glucose. However, manual stirring was still required. It is shown in the raw data for both the AT and BT sensor that the noise was significantly reduced, and the desired step trend corresponding to an increase in glucose concentration is more visible. This method also greatly increased the sensitivity of both sensors. In the presented case, the resulting sensitivity was 7.91 μA/M for the AT sensor and 8.12 μA/M for the BT sensor. In this experimental setup, the BT sensor showed higher sensitivity, opposed to the AT sensor showing higher sensitivity in the previous setup. Both sensors had high R^2 values, 0.9983 for the AT sensor and 0.9971 for the BT sensor. However, a limitation of this method is the inability to test the sensors within the physiological range of glucose. Due to the lower starting volume in the well, the volume of glucose additions required to obtain values within the physiological range was not achievable. This led to further methods being pursued and improvements made.

Figure 3.10 The top plot shows the raw data for AT sensor with glucose additions as a function of time. Additions began at 900 seconds and a controlled amount of 1M glucose stock solution was added every 60 seconds. The bottom plot shows the corresponding calibration curve.

Glucose Detection - High Concentration Range - BT
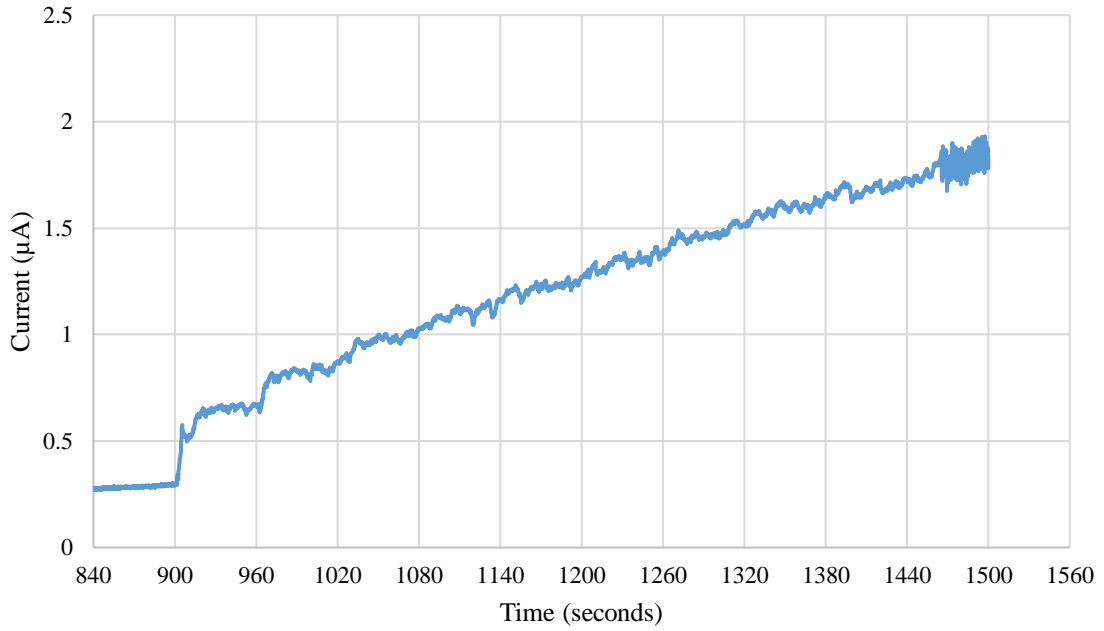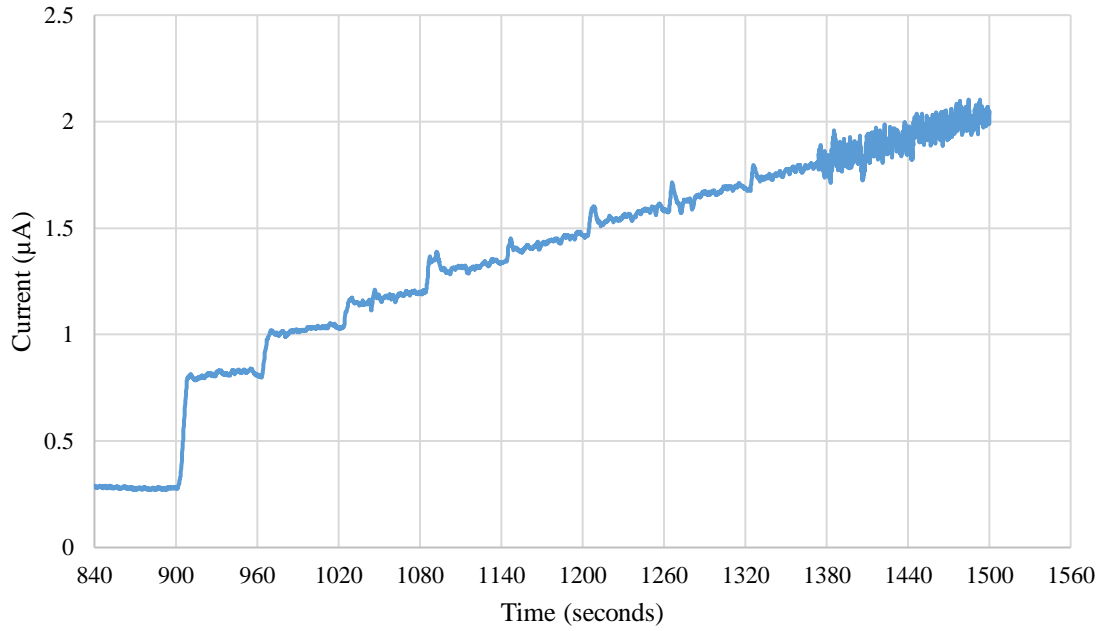
Glucose Concentration vs Current - High Concentration Range - BT

$y = 8.1205x + 0.7283$
$R^2 = 0.9971$
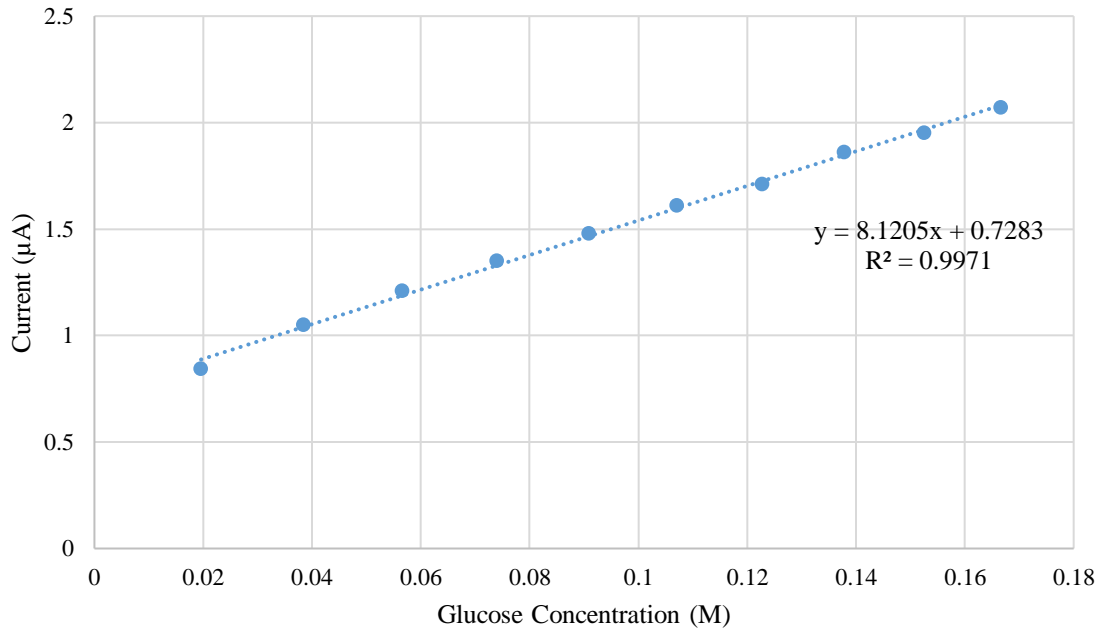
Figure 3.11 The top plot shows the raw data for BT sensor with glucose additions as a function of time. Additions began at 900 seconds and a controlled amount of 1M glucose stock solution was added every 60 seconds. The bottom plot shows the corresponding calibration curve.

3.5.2.1 Combined Low to High Glucose Concentration Range

The data obtained from low glucose concentration range testing and high glucose concentration range testing was then combined to examine the trend across the entire concentration range. These plots are shown in Figure 3.12. In both the AT and BT case, the combined currents follow the desired trend. More specifically, the current points at the beginning of the high concentration plot follow in line with the current points at the end of the low concentration plot. This trend is stronger in the BT data than the AT data. In both instances, the sensitivity of the sensor to glucose is higher in the low concentration range than high concentration range, which is to be expected. As the concentration is continually increased saturation occurs leading to a lower sensitivity. The trends shown in this combined data reiterates the capability of the functionalized glucose biosensor to detect changes in glucose concentration across a wide concentration range.

AT Sensor

y = 7.9054x + 0.5499
R² = 0.9983

y = 40.465x + 0.311
R² = 0.9979

- Low Concentration
- High Concentration
- Linear (Low Concentration)
- Linear (High Concentration)

BT Sensor

y = 8.1275x + 0.7274
R² = 0.997

y = 28.667x + 0.2693
R² = 0.9978

- Low Concentration
- High Concentration
- Linear (Low Concentration)
- Linear (High Concentration)
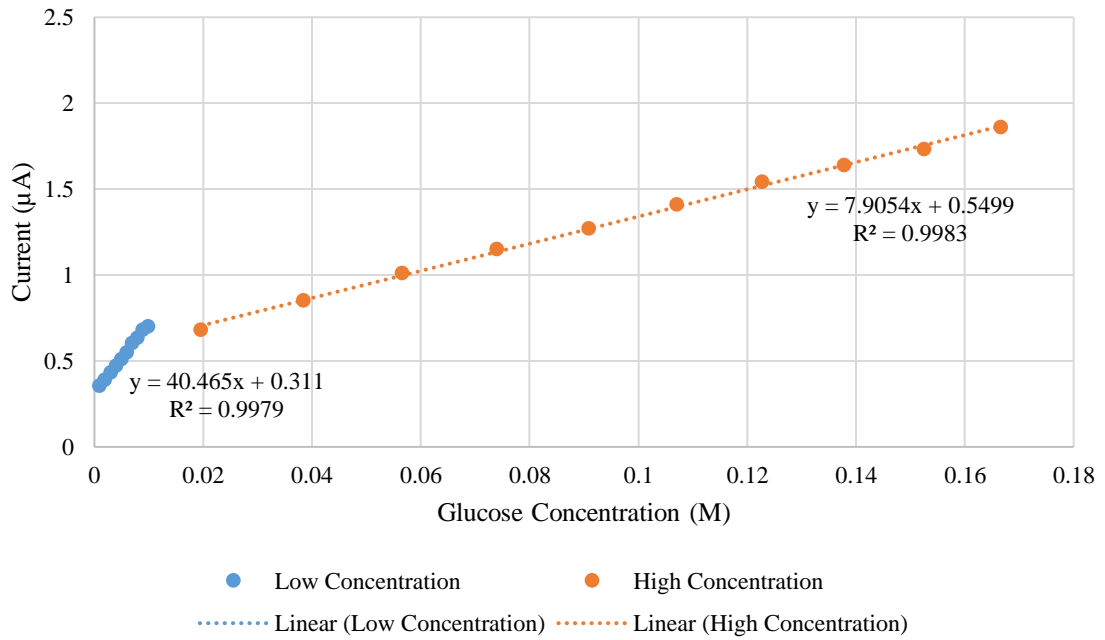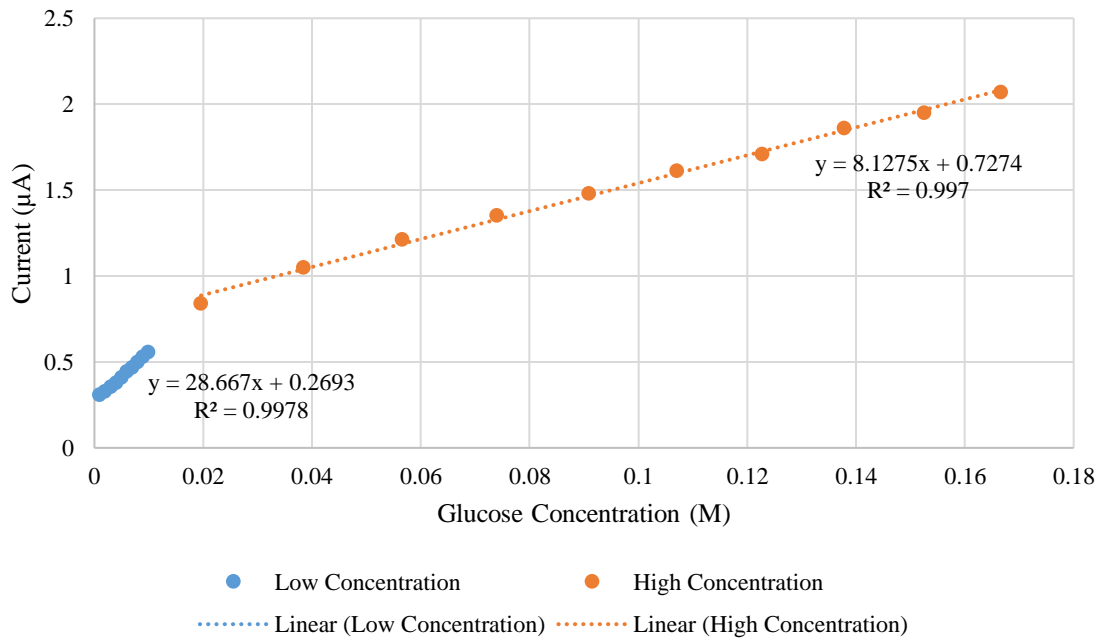
Figure 3.12 Combined calibration curve data for low glucose concentration and high glucose concentration testing.

3.5.3 Manual Solution Flow

Due to the setup of this method, particularly that the solutions for each 10 additions were prepared separately, a wide range of glucose concentrations were able to be tested in one experiment, including within physiological range. This method resulted in large spikes that occurred during the transition of removing and replacing solution on the electrodes. These spikes were likely a result of human capabilities and caused by potential non-uniformity of the flow of liquid. As solution was being removed and new solution added, if any section of the electrodes were not covered in solution and exposed to air it resulted in this large current spike. This was an aspect that improved with practice and repetition but could not fully be eliminated. To create a calibration curve from this data, the final steady state current from each time segment (before each spike) was taken and plotted. This resulted in a sensitivity of 5.54 µA/M and an R^2 value of 0.9822. The sensitivity was in-between that of the individual high and low concentration tests, being more similar to that of the high concentration testing. The R^2 value was lower than both previously tested methods. For this method, only an AT sensor was tested.
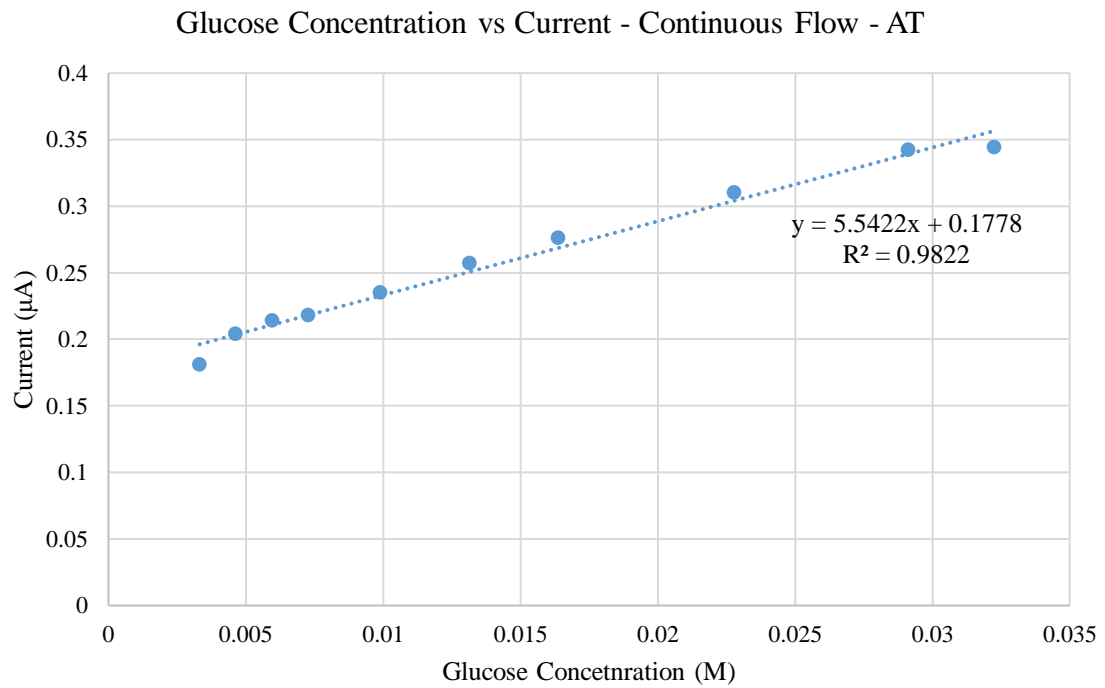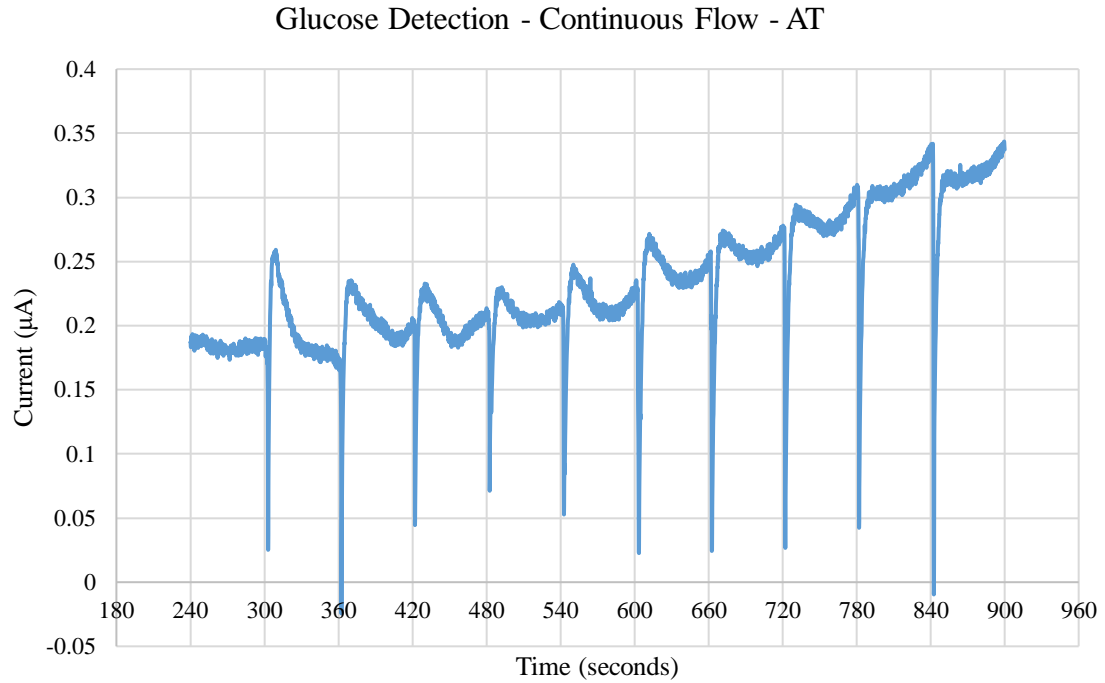
Figure 3.13 The top plot shows the raw data as a function of time, obtained by performing glucose additions using two pipettes to manually simulate continuous solution flow. Additions began at 300 seconds and continued every consecutive minute after with increasing concentration of glucose solution. The bottom plot shows the corresponding calibration curve.

3.5.4 Microfluidic, Chip-Based Platform

Expanding on the principle of the manual flow of solution method discussed previously, specifically flow of a small amount of solution across the electrodes, and the broader, more encompassing range of glucose concentration, leads to the microfluidic, chip-based platform. Similarly to the previous method, the microfluidic, chip based platform allowed for testing across a wide range of glucose concentrations with one experiment. With this method, the continuous flow of liquid across the electrodes produced a steady current response without any external noise or environmental interference. The steady state current at each time segment was taken and plotted to form each calibration curve. This method showed a significant increase in sensitivity for both the AT and BT sensor, with the AT sensor sensitivity being substantially higher than the BT sensor. In this case, for the lower concentration detection, the average sensitivity (3 experiments) of the AT sensor was 47.95 µA/M, compared with 30.40 µA/M for the BT sensor. For the higher concentration detection, the average sensitivity (3 experiments) of the AT sensor was 24.68 µA/M, compared with 14.99 µA/M for the BT sensor. The AT sensor also showed a higher linearity in both the low and high concentration range with an R^2 value of 0.9992 (low) and 0.9983 (high), compared with the BT sensor R^2 value of 0.9493 (low) and 0.9691 (high). The response time, or the time from each addition to when 90% of the steady state current is reached, was determined from the raw data. The response time was the same for each sensor, both producing a fast response time of an average of 15 seconds. However, the limit of detection (calculated using the formula LOD=3.3σ/S, where σ is the standard deviation of the response and S is the slope of the calibration curve) differed between the two models. These values were determined using the lower range concentration data of three

experiments taken on the first day of sensor testing. For the AT sensor, the LOD was

calculated as 0.02 mM. For the BT sensor, the LOD was higher at 0.11 mM.
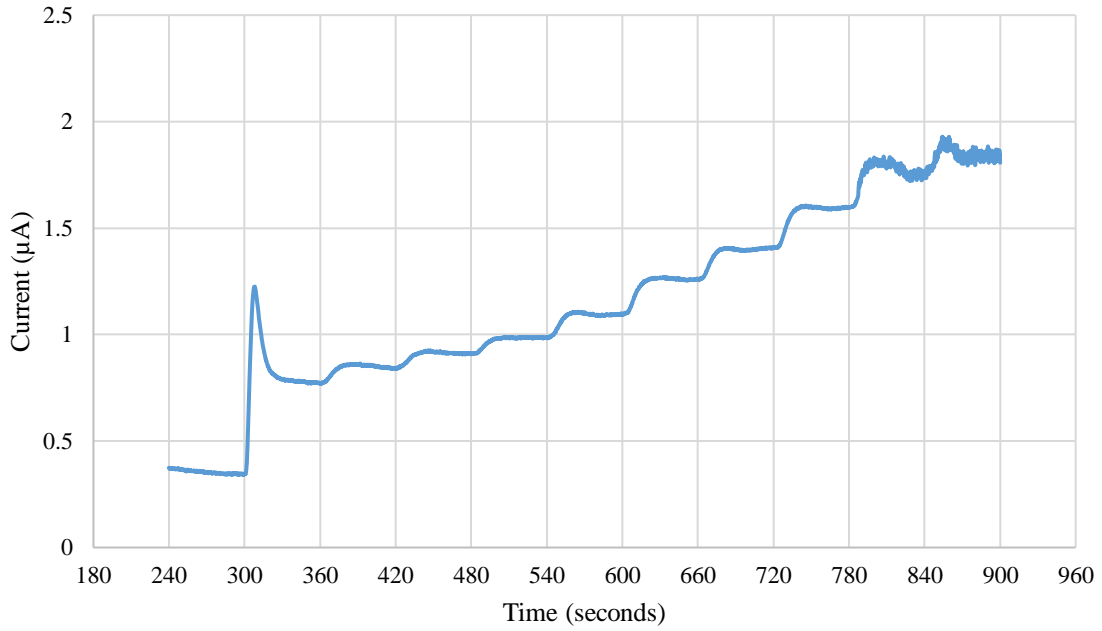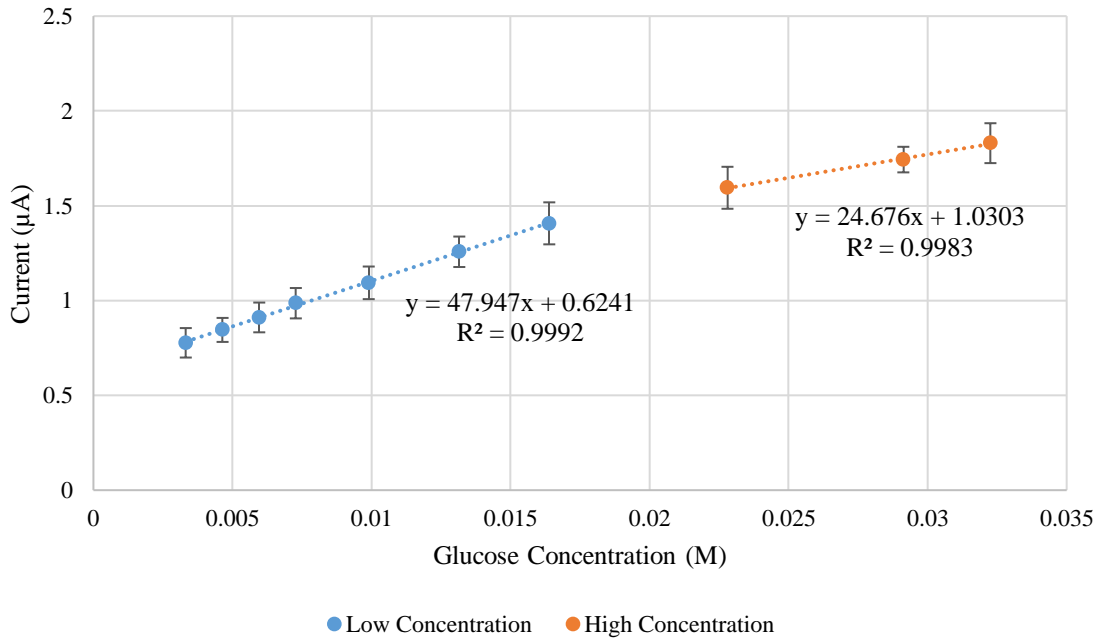
Figure 3.14 The top plot shows the raw data for AT sensor of glucose additions as a function of time (average of 3 experiments). Additions began at 300 seconds and continued every consecutive minute. 100 μL of increasing concentration of PBS/p-Benzoquinone/glucose solution was added to the well and pumped through the microfluidic system. The bottom plot shows the corresponding calibration curves.
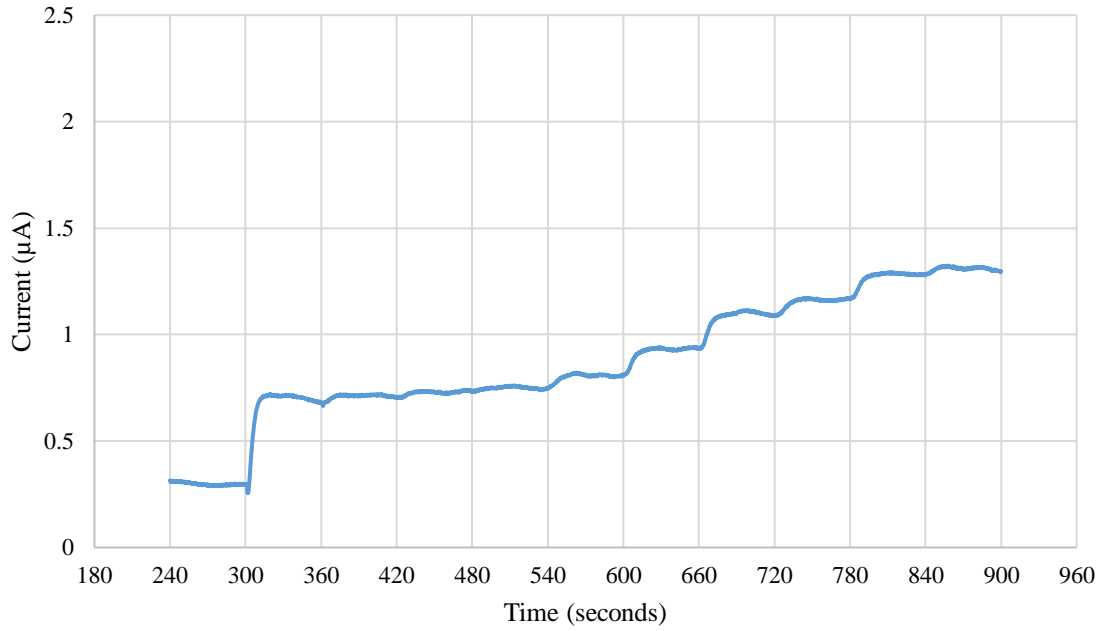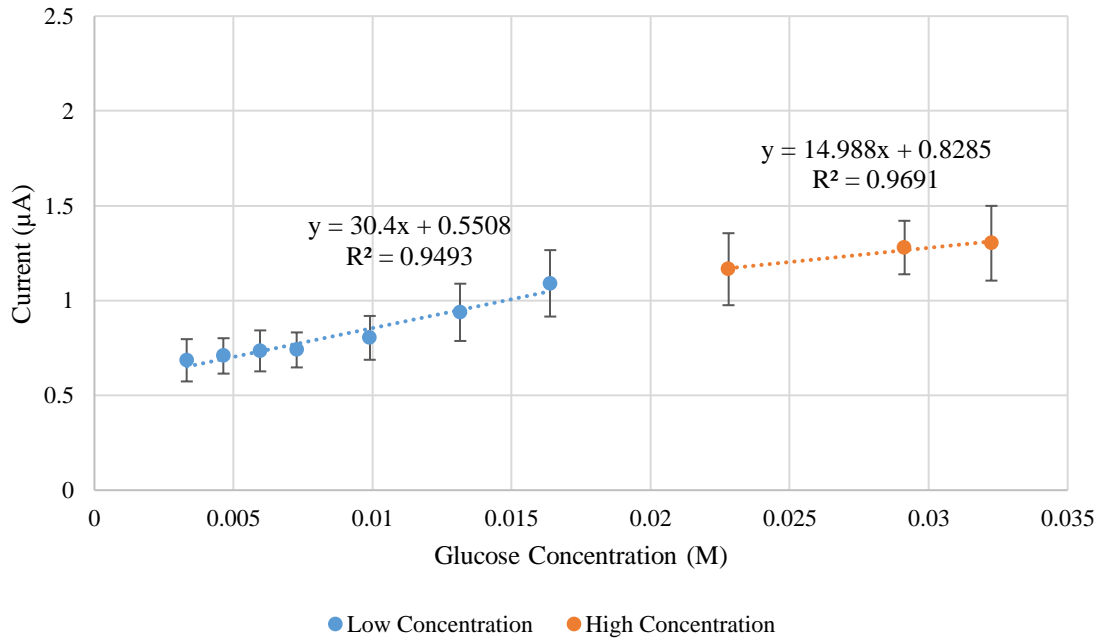
Figure 3.15 The top plot shows the raw data for BT sensor of glucose additions as a function of time (average of 3 experiments). Additions began at 300 seconds and continued every consecutive minute. 100 μL of increasing concentration of PBS/p-Benzoquinone/glucose solution was added to the well and pumped through the microfluidic system. The bottom plot shows the corresponding calibration curve.

3.5.5 Degradation Behavior of the Sensors

The longevity of each sensor, examined by looking at the sensitivity (slope), was also tested over a period of 28 days. For the AT sensor, peak performance was observed on day 0 and a rise in performance was seen on day 10, followed by a steady decline. For the BT sensor, there was a steady decline in performance after day 0, with a slight increase in average performance observed on day 4. The data in Table 3.5 and Table 3.6 as well as the graphed data in Figure 3.16 confirms that the AT sensor showed better overall performance. The average sensitivity (based off of three separate runs of the experiment) was higher for the AT sensor on every day of testing. The results for the AT sensor on day 28 of testing are most similar to the results on day 14 of testing for the BT sensor. To confirm this further, a one-way repeated measurement ANOVA with an alpha of 0.05 was performed between the AT and BT data. This resulted in a P-value of 0.0006. Since the P-value was less than alpha it can be concluded that the sensor model (AT vs. BT) had a statistically significant effect on sensitivity. Additionally, a one-way repeated measurement ANOVA was used to examine the effect of testing day on both the AT and BT sensor separately. For the AT sensor and BT sensor, the resulting P-value was 7.13×10^{-11} and 2.52×10^{-6}, respectively. These values are both less than alpha and it can be concluded that the testing day had a statistically significant effect on sensitivity for both the AT and BT sensor. It's also important to note that with the previous methods (sensor not attached to a PDMS platform) the sensors were regarded as single use sensors, due to their rapid decrease in performance and visual degradation of the reference electrode. The sealing of the sensor to the PDMS platform, and subsequent storage at 4°C in this sealed state, has shown to preserve the capabilities of the sensor for an extended period of time. The

environment within the seal seems to prevent the desiccation, or dehydration, of the

molecules.

	Day 0		Day 3		Day 6		Day 10		Day 14		Day 28	
	Slope	R^2	Slope	R^2	Slope	R^2	Slope	R^2	Slope	R^2	Slope	R^2
Run 1	35.88	0.9841	26.61	0.9880	20.58	0.9888	25.36	0.9897	*	*	8.38	0.9614
Run 2	37.96	0.9855	29.99	0.9889	25.02	0.9786	30.07	0.9974	16.57	0.9918	11.08	0.9832
Run 3	40.88	0.9895	N/A		26.68	0.9819	32.70	0.9874	19.31	0.9875	13.25	0.9933
Mean	38.24	0.9864	28.30	0.9885	24.09	0.9831	29.37	0.9915	17.01	0.9617	10.91	0.9793
Std Dev	2.51	0.0030	2.39	0.0010	3.15	0.0050	3.72	0.0050	1.94	0.0030	2.44	0.0160

Table 3.5 Slope (sensitivity) and linearity (R^2) data for the AT sensor over a 28-day testing period. The values for each experiment and the average of all 3 experiments is given.
*On Day 14, the first experiment run did not follow normal trends and it was determined that further flushing of the microfluidic channel was needed before further detection experiments were performed.

	Day 0		Day 4		Day 6		Day 10		Day 14		Day 28	
	Slope	R^2	Slope	R^2	Slope	R^2	Slope	R^2	Slope	R^2	Slope	R^2
Run 1	18.79	0.9649	22.99	0.9969	12.14	0.9949	*	*	8.93	0.9965	2.44	0.7032
Run 2	22.92	0.9773	22.11	0.9920	21.62	0.9965	11.76	0.9882	10.33	0.9960	2.39	0.6339
Run 3	27.41	0.9557	26.30	0.9946	17.86	0.9924	13.81	0.9973	11.54	0.9862	4.28	0.9474
Mean	22.95	0.9659	23.80	0.9945	17.21	0.9946	11.83	0.9844	10.27	0.9929	3.04	0.7615
Std Dev	4.18	0.0120	2.21	0.0020	4.77	0.0020	1.45	0.0060	1.31	0.0060	1.07	0.1650

Table 3.6 Slope (sensitivity) and linearity (R2) data for the BT sensor over a 28-day testing period. The values for each experiment and the average of all 3 experiments is given.
*On Day 10, the first experiment run did not follow normal trends and it was determined that further flushing of the microfluidic channel was needed before further detection experiments were performed.
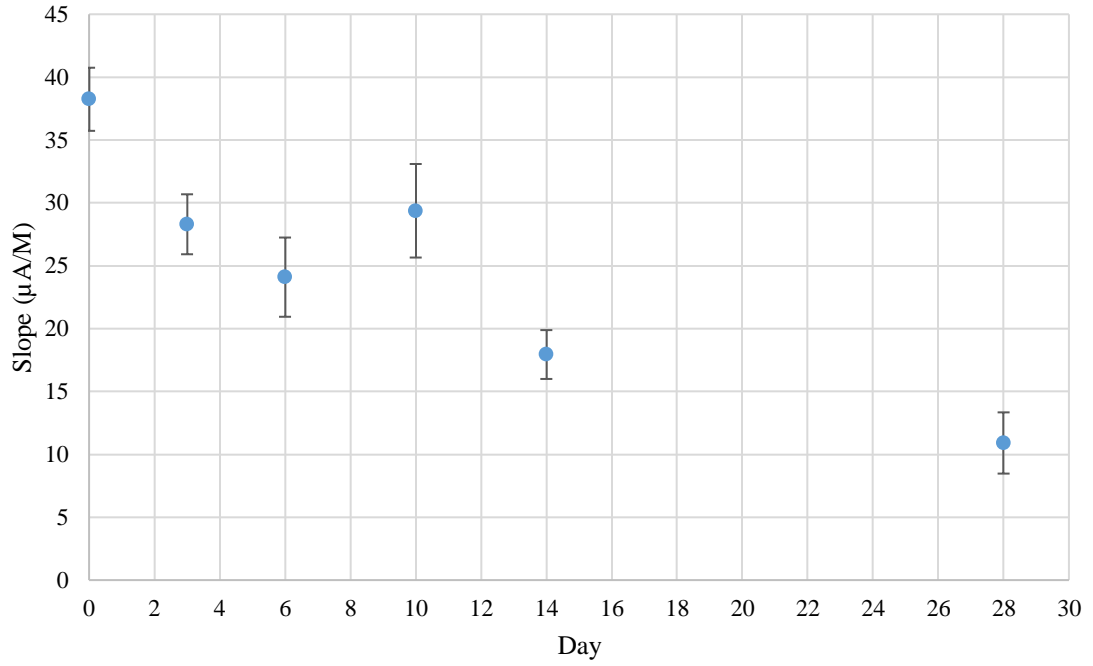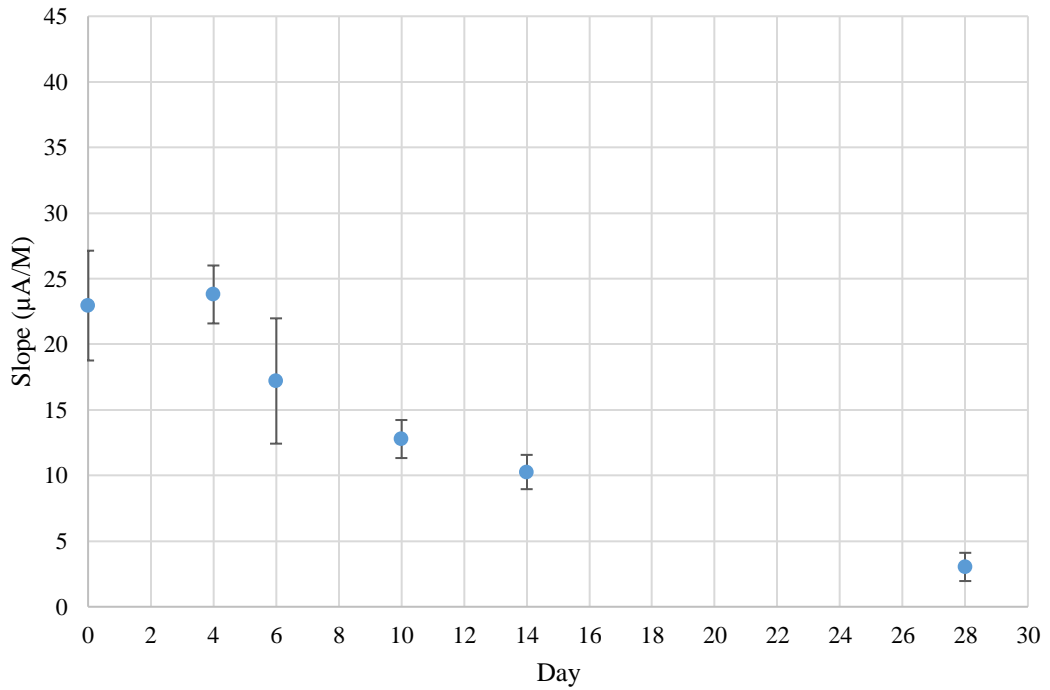
Figure 3.16 The average sensitivity (slope) per day of testing is shown for the AT sensor (top) and BT sensor (bottom). Each sensor was tested at given intervals over a period of 28 days.

3.5.6 Robustness of the Sensors

The robustness of the sensor was tested by performing different experiments from high to low glucose concentration as opposed to low to high concentration, examining the current response. This was done using the AT model sensors and completed the same day as day 6 detection testing. For the first experiment, shown in Figure 3.17, once steady state current was reached, DI water was added to the system at 300 and 360 seconds. At 420 seconds and every minute after, a glucose solution was added, starting from the highest glucose concentration, and decreasing with each addition. The current response followed the desired step trend in the decreasing direction. The steady state current at each time segment (exempting the DI water additions) was taken to plot the calibration curve. This resulted in a sensitivity of 27.83 µA/M and an R^2 value of 0.9616. The detection testing of the AT sensor on day 6 resulted in a sensitivity value of 24.09 µA/M. The similarity of these two sensitivity values supports the robustness of the sensor capabilities.

DI Water followed by Additions of High to Low Glucose Concentration

Glucose Concentration vs Current (DI Water followed by Additions of High to Low Glucose Concentration)

$$y = 27.83x + 0.5998$$
$$R^2 = 0.9616$$
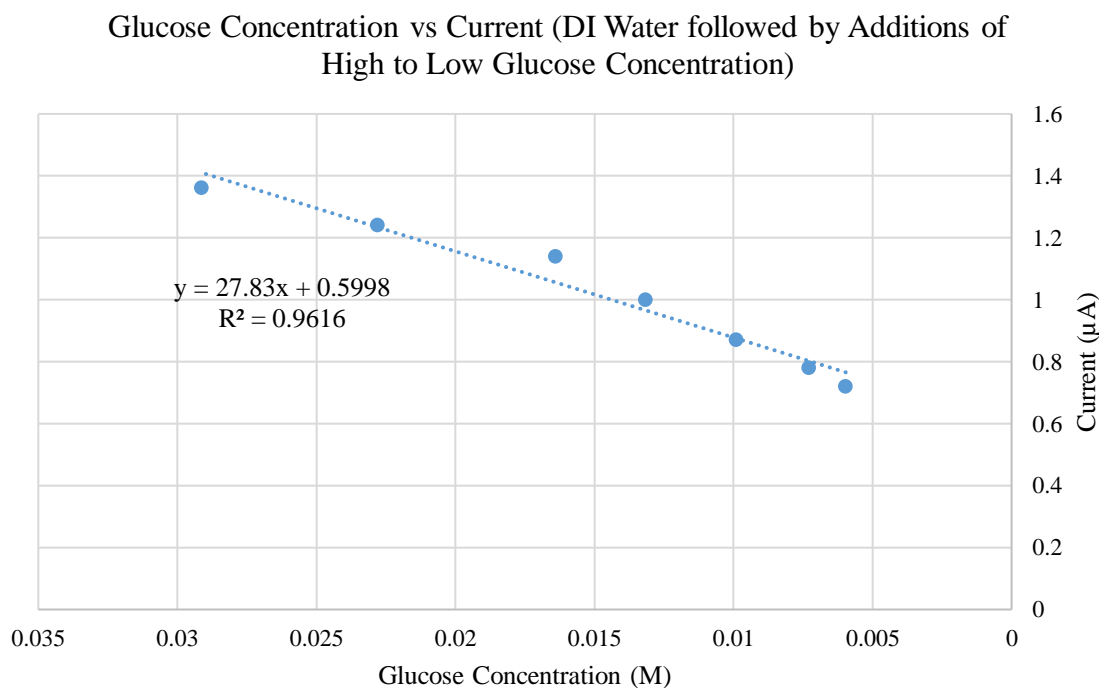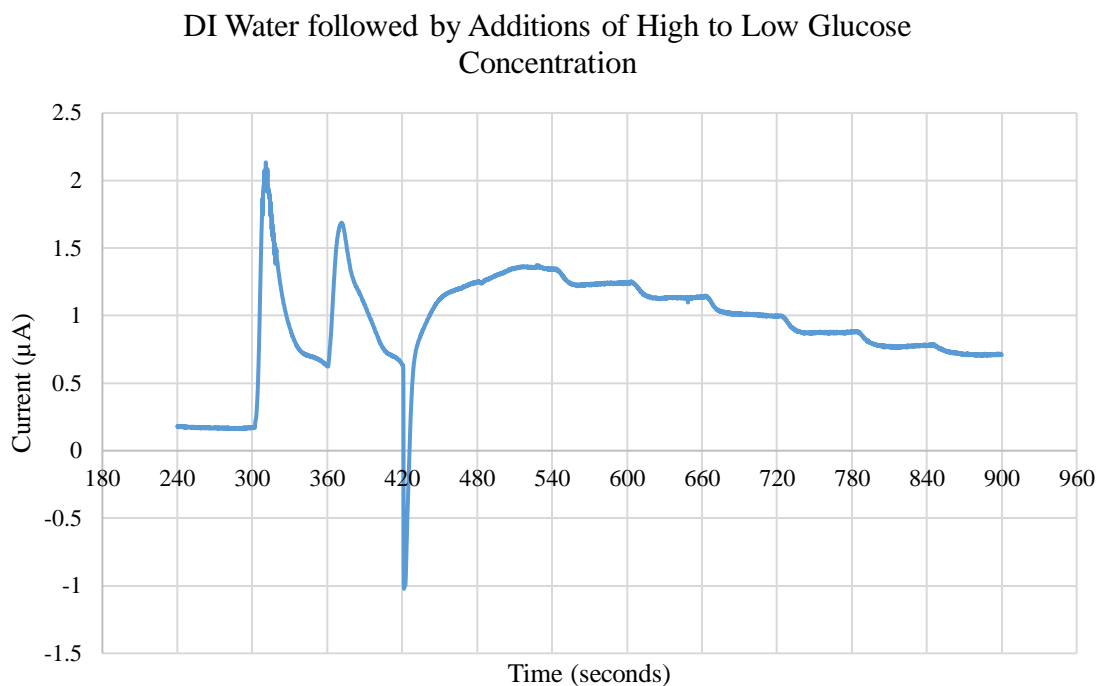
Figure 3.17 The top plot shows the raw data as a function of time. At 300 and 360 seconds, 100 µL additions of DI water were added to the system. At 420 seconds and every consecutive 60 seconds, 100 µL of PBS/p-Benzoquinone/glucose solution was added to the system, from high to low glucose concentration. The bottom plot shows the corresponding calibration curve without the DI water additions.

For the second experiment, shown in Figure 3.18, additions were alternated between DI water and glucose solution. After steady state current was reached at 300 seconds, the highest glucose concentration was added, followed by an addition of decreased glucose concentration. This pattern was repeated 3 more times, for a total of 3 DI water additions (420, 600 and 780 seconds) and 7 glucose concentration additions in decreasing order (300, 360, 480, 540, 660, 720 and 840 seconds). The sensor responded as expected to DI water additions and showed the appropriate decreasing step trend to glucose additions. The calibration curve was created by dividing the data into four segments (300-420 seconds, 480-600 seconds, 660-780 seconds and 840-900 seconds). The lowest steady state current was taken from each of the four segments and plotted against the corresponding concentration. This resulted in a sensitivity of 35.26 μA/M and an R^2 value of 0.9513. This sensitivity value is similar to that produced by the normal detection testing of low to high glucose concentration and the previous high to low glucose concentration testing, further supporting the robustness of the sensor.

Alternating Additions of DI Water and High to Low Glucose Concentration
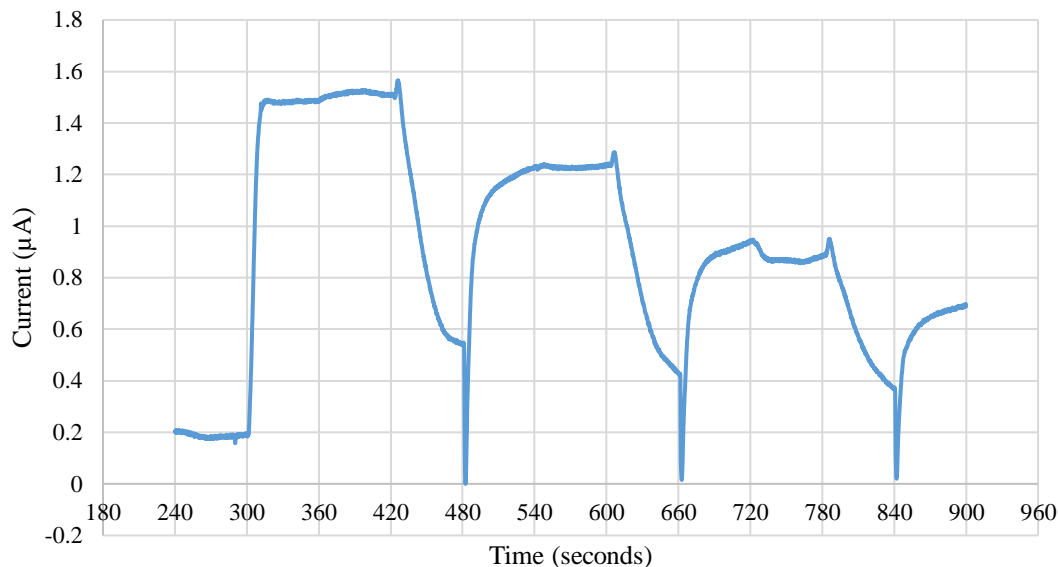
Glucose Concentration vs Current (Alternating Additions of DI Water and High to Low Glucose Concentration)

$$y = 35.264x + 0.5338$$
$$R^2 = 0.9513$$
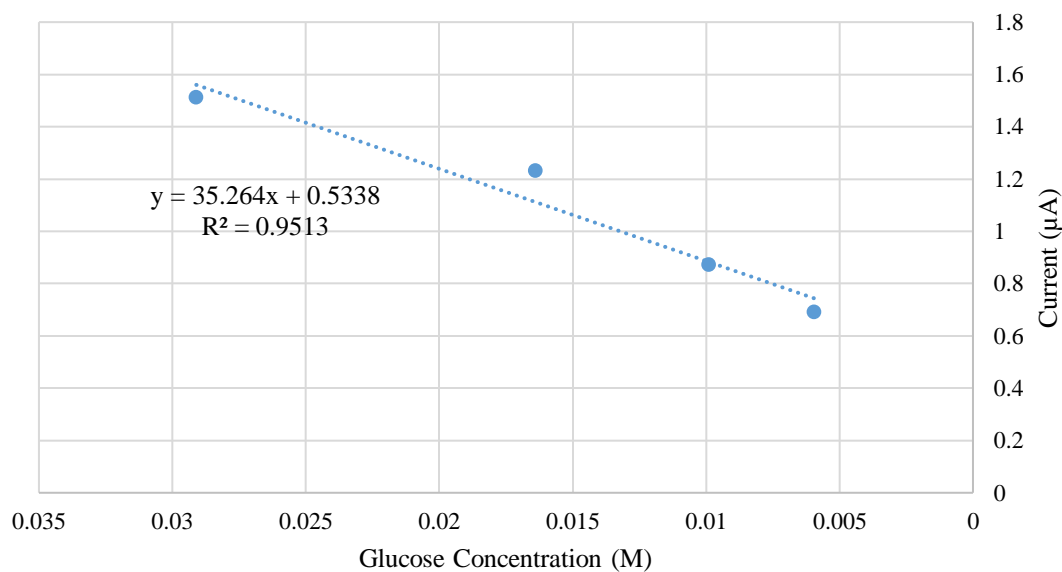
Figure 3.18 The top plot shows the raw data as a function of time. At 420, 600 and 780 seconds 100 µL additions of DI water were added to the system. At the remaining time points, 100 µL additions of PBS/p-Benzoquinone/glucose solution were added to the system in order of decreasing glucose concentration. The bottom plot shows the calibration curve (minus the DI water additions) constructed by taking the lowest steady state current response per segment (300-420s, 480-600s, 660-780s, and 840-900s).

3.6   Conclusion

Through continuous improvement in design and testing parameters, the microfluidic, chip-based biosensor for glucose detection was successfully completed. This provides an effective and promising platform for detection and continuous monitoring of glucose. The microfluidic design paired with the amperometric chip delivers rapid, sensitive and reproducible results, while maintaining a detection limit within physiological ranges of glucose. This design allows for an easy to use method that could translate well for uses in a research or clinical application. Based on this success, our goal of exploring the design beyond solely glucose detection was able to be investigated.

CHAPTER 4.   FLUIDIC, CHIP-BASED CHOLESTEROL BIOSENSOR

4.1   Introduction

In this chapter, further exploration of the fluidic, chip-based sensor beyond glucose detection is discussed through the use of different functionalization methods to target other important biomarkers, specifically cholesterol. Cholesterol is a critical biomarker that is physiologically essential but can cause harm when present at elevated or reduced levels. At elevated levels problems such as atherosclerosis, heart disease and nephrosis may occur and at low levels hypothyroidism and anemia can be an issue (Rahman, 2014). Current methods for cholesterol detection and measurement include fluorometric and colorimetric enzymatic assays, gas and liquid chromatography, mass spectroscopy and classical chemical methods based on the Abell-Kendall protocol. While all of these methods work, they come with disadvantages, including multistep procedures, costly equipment and materials, sample pretreatment requiring extensive training, and long processing times (Li et al., 2018). A fluidic, chip-based biosensor that can quickly and accurately detect cholesterol would provide a highly desirable option to combat these current disadvantages, offering a device that is beneficial in both clinical and research applications.

In the following sections, the biofunctionalization process of the cholesterol biosensor, the methods for detection and some obtained results are presented.

4.2   Sensor Biofunctionalization

Similar to the biofunctionalization process for the glucose biosensor, prior to using each sensor was cleaned using the RCA-1 method, which involves the removal of organic contaminants using a 5:1:1 solution of DI water, ammonium hydroxide (Sigma-Aldrich,

St. Louis, MO, USA) and hydrogen peroxide (Sigma-Aldrich, St. Louis, MO, USA). After cleaning, the sensor is rinsed in DI water, dried and prepared for the biofunctionalization steps. The enzymatic biofunctionalization process involves cholesterol oxidase (ChOx) (Sigma-Aldrich, St. Louis, MO, USA) being functionalized on the working electrode through the electropolymerization of pyrrole (VWR, Batavia, IL, USA). Conceptually, a positive potential is applied to the system to pull electrons away and facilitate the pyrrole to polypyrrole reaction that is required. Visually, the biofunctionalization process is shown in Figure 4.1.
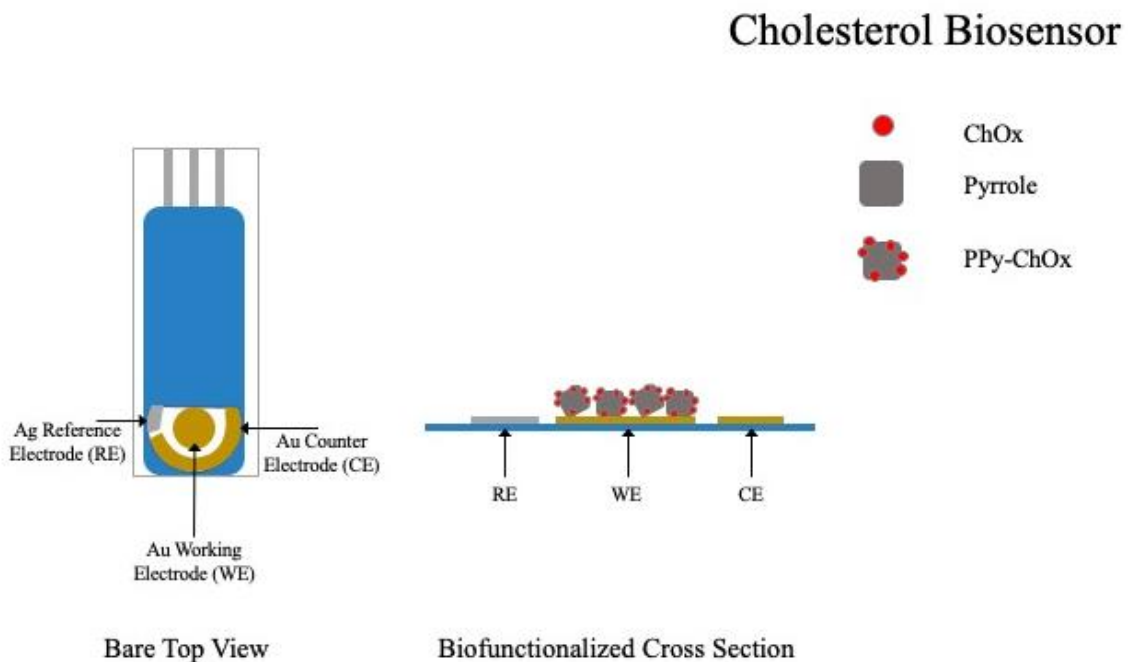
Figure 4.1 Schematic of the biofunctionalization process for the cholesterol biosensor.

This process was performed using a similarly made PDMS well as shown in Figure 3.7. The PDMS well was clamped onto the sensor and a syringe with a blunt needle was placed into the well. The needle tip was positioned close to the working electrode without making contact with the electrode surface. The needle tip was also wrapped in conductive tape, which was then connected to the PARSTAT MC multichannel potentiostat

(AMETEK, Berwyn, PA, USA), allowing the metal needle to function as the counter electrode in a two-electrode system setup. The deposition solution was pumped from the syringe into the well, and the solution was removed from the well and replaced periodically throughout the experiment. For this method, chronopotentiometry experiments were carried out in 0.1 M PBS containing 0.2 mM pyrrole and 1.67 mg/mL ChOx. The deposition current of 10 µA was applied for 8 minutes (480 seconds) for AT electrodes. Based on the previous results obtained for the glucose biosensors, only the AT model electrodes were used based on the overall better performance. Functionalized sensors were sealed to a PDMS microfluidic platform (constructed as discussed previously) and stored dry in the refrigerator at 4°C.

4.3   Methods for Cholesterol Detection

A positive potential was applied to the working electrode and an electron transfer between the electrode and ChOx occurs due to the redox reaction between ChOx and cholesterol. As shown in the following reaction, cholesterol is catalyzed by ChOx, and results in a cholesterol ketone and hydrogen peroxide. The applied positive potential facilitates the hydrogen peroxide redox reaction, which produces oxygen, hydrogen and electrons.

$$Cholesterol + O_2 \xrightarrow{ChOx} 4 - Cholestene - 3 - one + H_2O_2$$

$$H_2O_2 \xrightarrow{Constant\ Potential} O_2 + 2H^+ + 2e^-$$
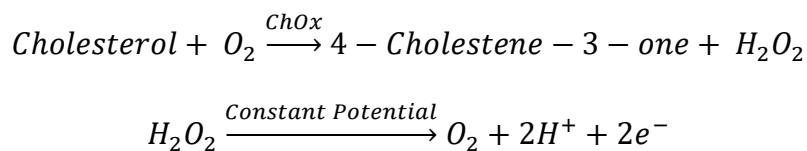
Similar to the glucose detection sensor, the sensing capabilities of the biofunctionalized cholesterol sensor were assessed by performing step-wise tests at increasing concentrations of cholesterol.

A similar experimental setup was utilized, consisting of the three-electrode chip sealed to a PDMS microfluidic platform as schematically shown in Figure 4.2. This platform design was almost identical to the design used for the glucose detection. However, an improvement was made by changing the shape of the dome over the electrodes. The previous full-circle dome was modified to a half-circle dome for eliminating any dead space for solution flow.
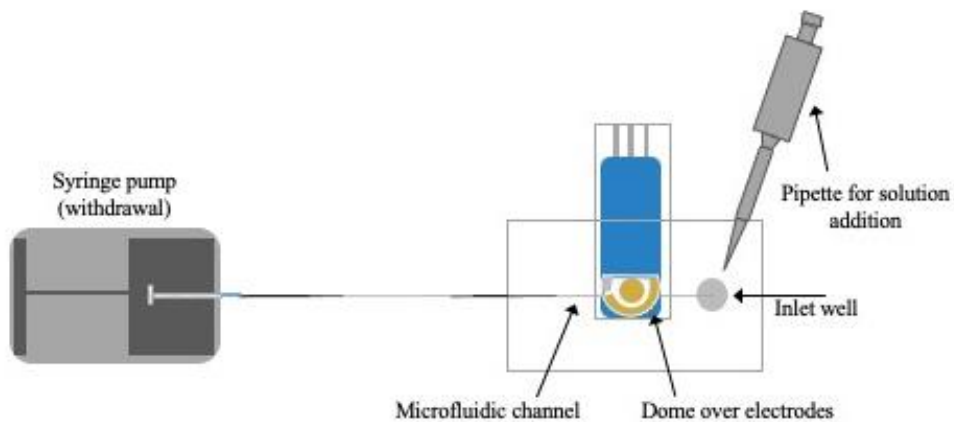
Figure 4.2 Schematic of the overall experimental setup for amperometric cholesterol detection.

A needle with tubing was inserted into the outlet channel and connected to the syringe pump. The withdrawal function was used to pull solution through the microfluidic system at a rate of 0.2 mL/min. For detection experiments, a Matrix Plus™ Cholesterol Reference Kit from Verichem Laboratories Inc. was used. The contents of this kit are shown in Table 4.1. The physiological range of total cholesterol that is classified as healthy is 125 to 200 mg/dL, with values above 200 mg/dL classified as high cholesterol. This kit provides a range that encompasses physiological values. Although the solutions in this kit also contain uric acid, it was determined that this was still a good option due to the wide range of pre-made cholesterol concentrations in solution and since it has been shown that uric acid

provides minimal interference in cholesterol detection (Gao et al., 2019, Gholivand and Khodadadian, 2014). It is also noted that the addition of a mediator into solution eliminates possible interference (Wang and Hu, 2020). Based on this, a solution consisting of 10 mM potassium ferricyanide (mediator) in PBS was added to each cholesterol solution prior to detection experiments.

Solution Level	Cholesterol (mg/dL)	Cholesterol (mM)	Cholesterol After Dilution with PBS/Potassium Ferricyanide Soln. (mg/dL)	Cholesterol After Dilution with PBS/Potassium Ferricyanide Soln. (mM)	Uric Acid (mg/dL)	Uric Acid (M)
A	40	1.034	23	0.604	2	0.000119
B	155	4.008	90	2.339	7	0.000416
C	270	6.982	158	4.073	12	0.000714
D	385	9.956	225	5.808	17	0.001011
E	500	12.930	292	7.543	22	0.001309

Table 4.1 The contents of the 5 solutions in the Matrix Plus Cholesterol Reference Kit from Verichem Laboratories Inc. The kit provides the values in mg/dL. This table shows mg/dL and M for reference. These 5 solutions were used for cholesterol detection testing.

Before the experiment, 300 μL of phosphate buffered saline (PBS) containing 10 mM potassium ferricyanide was pumped through the system, and the pump was paused when the well was almost emptied. The sensor was allowed to sit in solution for pre-conditioning for 45 minutes. During initial trial experiments it was determined that the functionalized sensors for cholesterol detection required a longer pre-conditioning time than those for glucose detection. The experiment was then performed at an electrode potential of +0.60 V versus reference for a total of 6 to 7 minutes, depending on current stabilization time. After stabilization of the current at 1 to 2 minutes, a 200 μL addition of the lowest

cholesterol concentration solution (solution level A) was added into the well and the pump was started. Consecutive 200 µL additions of increasing cholesterol concentration (solution level B through E) were added to the well every minute after for a total of 5 different additions.

4.4   Preconditioning

Through preliminary testing and troubleshooting of the cholesterol biosensor, it was determined that the sensor needed to be preconditioned through prolonged storage time at 4°C to increase the overall sensitivity. A proper preconditioning step was determined by first testing a newly functionalized sensor on Day 0 and Day 3. Day 0 represents the day following sensor biofunctionalization and platform sealing. The sensor was kept in storage at 4°C in-between testing days. On Day 0 the detection experiment was run on the sensor one time to observe results and pre-condition the sensor prior to storage. The results from this experiment are shown in Figure 4.3. In contrast to subsequent testing, 100 µL additions of cholesterol solution were added instead of 200 µL additions. Based on this test and the pump withdrawal rate, it was determined that 200 µL additions would be the best option moving forward. It is shown in the graph that there was an initial spike as a result of the first cholesterol addition, and then slight current increases when an addition of increased concentration was added at 60, 90, 120, 150 and 180 seconds. However, the overall current trend was decreasing with increasing cholesterol concentration, instead of stepped current increases with increasing cholesterol concentration.
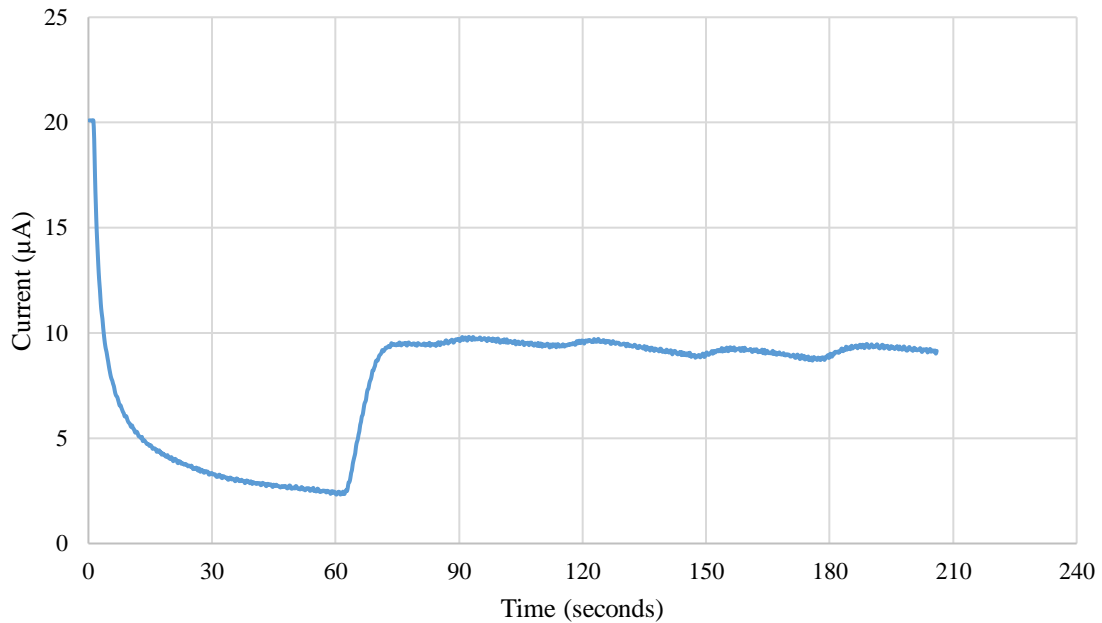
Figure 4.3 Raw data from cholesterol detection experiment performed on functionalized cholesterol sensor. PBS/ferricyanide solution present on electrodes from 0-60 seconds. Cholesterol solution additions of increasing concentration added at 60, 90, 120, 150 and 180 seconds.

Testing was then performed on Day 3 and five separate experiments were performed. The sensor platform was placed in refrigerator storage at 4°C for an hour in-between the 3rd and 4th experiment. Experiments 1 through 3 and 4 through 5 were run consecutively, including 45 minutes of pre-conditioning in-between each. The raw data for the 1st experiment and 5th experiment are shown in Figure 4.4. On the first experiment, the last addition of cholesterol (added at 360 seconds) wasn't detected, whereas on the fifth experiment it was (added at 300 seconds). Calibration curves were constructed by plotting the steady state current value for each cholesterol concentration. The fifth addition of cholesterol solution was detected on two out of the five experiments performed: run 3 and run 5. For the experiments that didn't detect the fifth cholesterol addition, only 4 points

were used to construct the calibration curve. Calibration curves for experiment 1 and 5 are

shown in Figure 4.5. Based on this, the data was divided into two groups for comparison.

This data is presented in Table 4.2.

Cholesterol Detection Day 3 Run 1
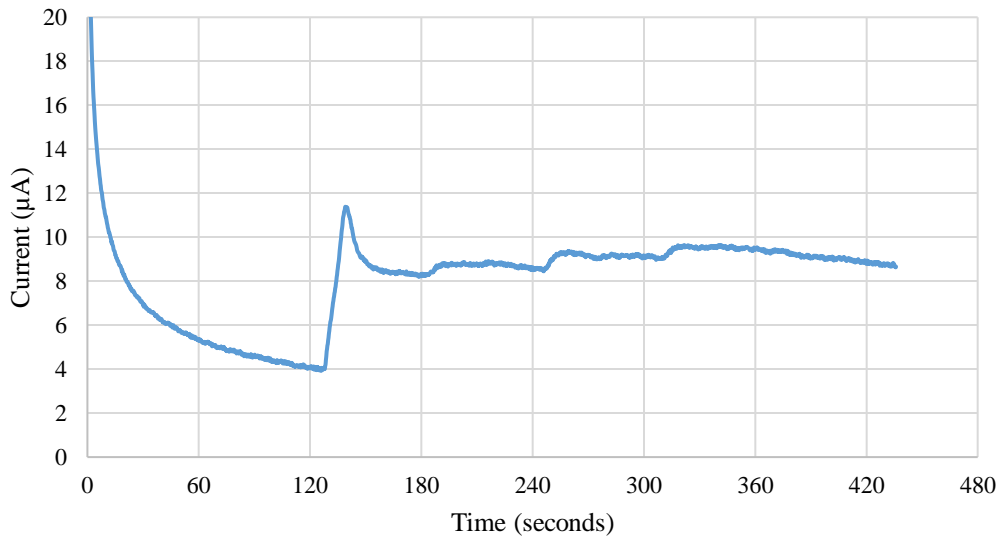
Cholesterol Detection Day 3 Run 5
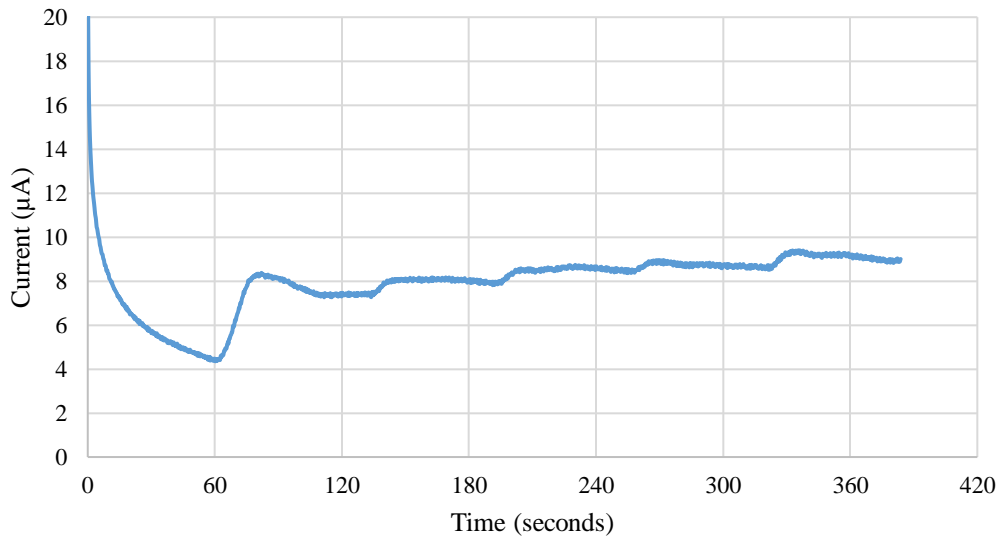
Figure 4.4 Raw data from cholesterol detection testing on day 3. The top graph shows raw data from the first experiment performed. The first cholesterol addition was added at 120 seconds and every 60 seconds after. The bottom graph shows raw data from the fifth experiment performed. The first cholesterol addition was added at 60 seconds and every 60 seconds after.

Cholesterol Concentration vs Current Day 3 Run 1

y = 0.2139x + 8.2018
R² = 0.9618
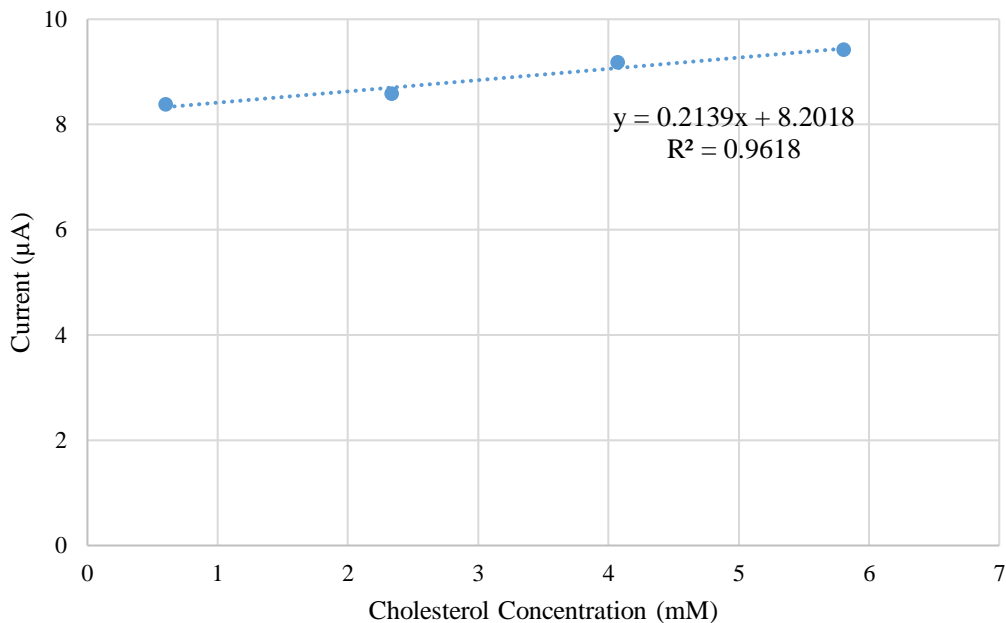
Cholesterol Concentration vs Current Day 3 Run 5

y = 0.2179x + 7.3804
R² = 0.9458
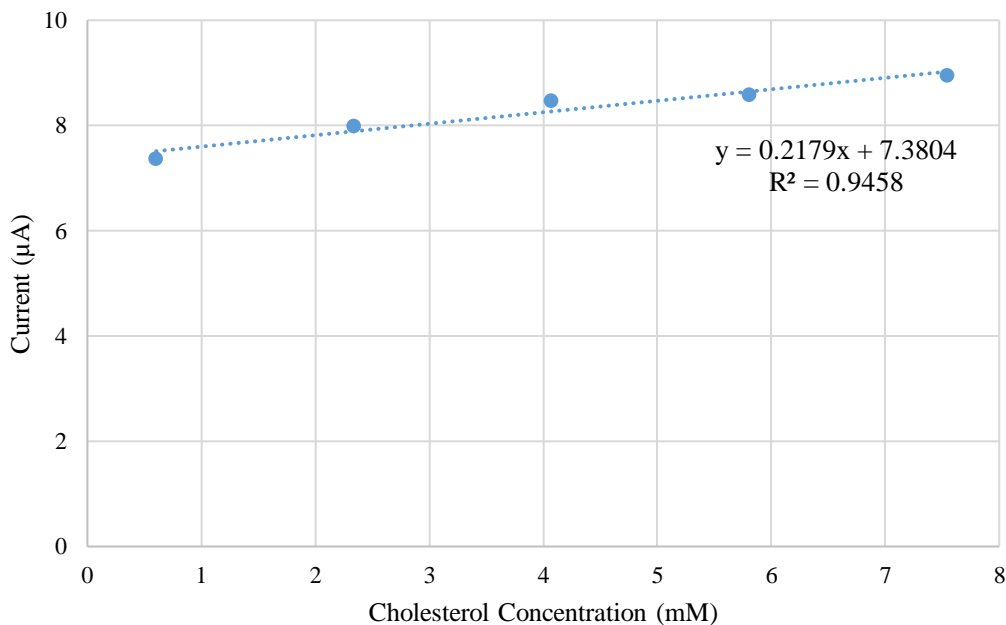
Figure 4.5 The top graph shows the calibration curve based on the first experiment and includes the first 4 data points. The bottom graph shows the calibration curve based on the fifth experiment and includes all 5 data points. This data is from Day 3 testing.

Group	Experiment Number	# of Points in Calibration Curve	Slope (µA/mM)	R^2
A	1	4	0.21	0.9618
	2		0.33	0.6481
	4		0.39	0.9783
B	3	5	0.19	0.6664
	5		0.22	0.9458

Table 4.2 Slope and R^2 values obtained from calibration curves. The first group of data points doesn't include the 5th cholesterol addition and the second group does.

Examining group A, it can be seen that the sensitivity of the sensor, or slope of the calibration curve, increased with increased time. In other words, the more pre-conditioning the sensor had been exposed to, as well as the more experiments performed on the sensor in one day, the higher the sensitivity to cholesterol. This same trend is observed in group B. It is also interesting to note that experiment 3 and experiment 5 were both conducted when the sensor had been out of refrigerator storage for a longer period of time. For example, prior to experiment 1 the sensor had been in refrigerator storage for over 48 hours, and the 5th cholesterol addition wasn't detected until experiment 3. Prior to experiment 4 the sensor had been in refrigerator storage for 1 hour, and the 5th cholesterol addition was detected on experiment 5. Although further exploration would be needed, it is possible there is a correlation between the amount of time in refrigerator storage to the amount of pre-conditioning time needed to reach an acceptable sensitivity. This is also interesting due to the 45 minutes of pre-conditioning performed on the sensor prior to any experiment. This means before the first experiment is run the sensor is equilibrated in solution at room temperature for 45 minutes, likely

reaching room temperature before the start of experiments. This suggests that the

temperature of the sensor at the time of testing isn't the main factor causing this trend.

To explore the previously observed trends further and continue optimization of

the testing conditions, a second set of testing was executed on a newly functionalized

sensor with testing done on Day 0, Day 1, Day 2 and Day 3. Three experiments were

performed on each day of testing. A summary of the slope and R^2 values obtained from

calibration curves for each run are given in Table 4.3.

	Day 0		Day 1		Day 2		Day 3	
	Slope (μA/mM)	R^2	Slope (μA/mM)	R^2	Slope (μA/mM)	R^2	Slope (μA/mM)	R^2
Run 1	-0.26	0.8152	0.04	0.4753	0.04	0.4484	0.08	0.6594
Run 2	-0.16	0.7154	0.12	0.7145	0.02	0.1924	0.18	0.9849
Run 3	-0.10	0.5711	0.09	0.6625	0.09	0.9284	0.12	0.8627
Mean	-0.16	0.7006	0.08	0.6174	0.05	0.5231	0.13	0.8357
Std Dev	0.09	0.1227	0.04	0.1258	0.04	0.3736	0.05	0.1644

Table 4.3 Summary of the slope and R^2 values obtained from calibration curves for each experiment on every day of testing on the cholesterol sensor.

Similar to the previous set of data, on Day 0 the current followed a decreasing

trend, signified by negative slope values. By examining the raw data it is clear that there

were small peaks when a cholesterol addition was added, but that the decreasing trend

then followed. This reiterates the need for a conditioning period to increase the sensitivity

of the sensor. On Day 0 the magnitude of the slope and R^2 value both decreased from run

1 to run 3. Given this, it appears the sensitivity of the sensor to cholesterol was slowly

increasing. As is visible from the calibration curves in Figure 4.6, in run 3 compared to

run 1, the points began to follow a curved trend instead of a straight line. This occurred because the last three additions were decreasing less, suggesting an increasing sensitivity.
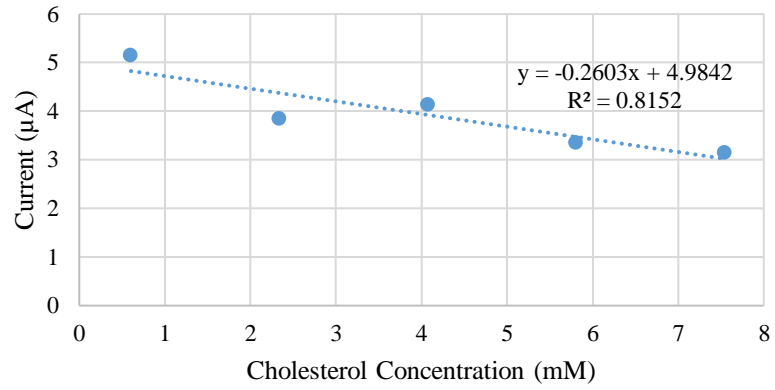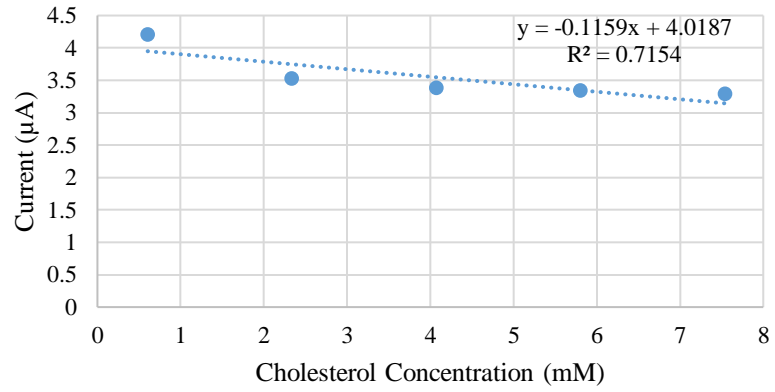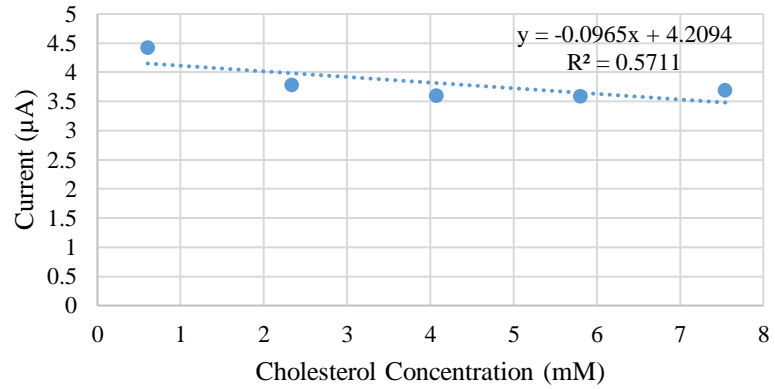
Figure 4.6 Calibration curves for all experiments performed on day 0 of cholesterol testing.

On Day 1 of testing the sensitivity was increased and the results followed a positive trend the remaining days of testing. By examining the data given in Table 4.3 it can be seen that the mean slope and mean R^2 values were highest on day 3 of testing. Based on this and the previous experimental timeline, the additional testing performed in-between Day 0 and Day 3 didn't seem to quicken the increased sensitivity. However, the additional testing may have improved the consistency of sensitivity. When the sensor was tested only on Day 0 and Day 3, the fifth cholesterol addition was detected on 2 out of the 5 runs. When the sensor was tested on Day 0 through Day 3, the fifth cholesterol addition was detected on all 3 runs, suggesting a more consistent sensitivity. Based on the results of both testing timelines, it was concluded that the best pre-conditioning method moving forward consisted of testing the sensor every day from Day 0 to Day 3.

4.5   Results & Discussion

From these preconditioning optimization experiments shown, detection testing on Day 3 was found to provide the highest sensitivity to cholesterol, and that testing every day up to Day 3 provided the most consistency in results. Based on this, a new sensor was functionalized and tested following the optimized pre-conditioning method. Additionally, further improvements were made to improve performance, specifically testing the sensor at the same time every day to ensure equal amount of testing and storage time in-between testing. The results obtained from testing the sensor daily will be discussed in greater detail. The average raw data from experiments performed on Day 3 and the corresponding calibration curve are given in Figure 4.7. A summary of the data from every day of testing is provided in Table 4.4.

Cholesterol Detection - Day 3

Cholesterol Concentration vs Current - Day 3
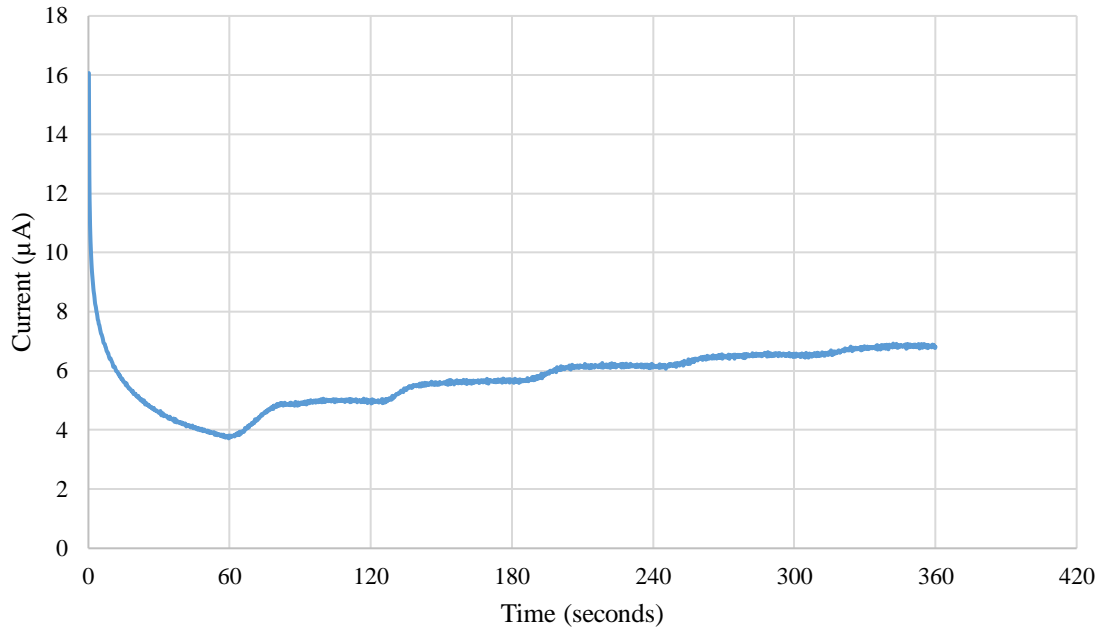
$y = 0.2636x + 4.9651$
$R^2 = 0.9623$
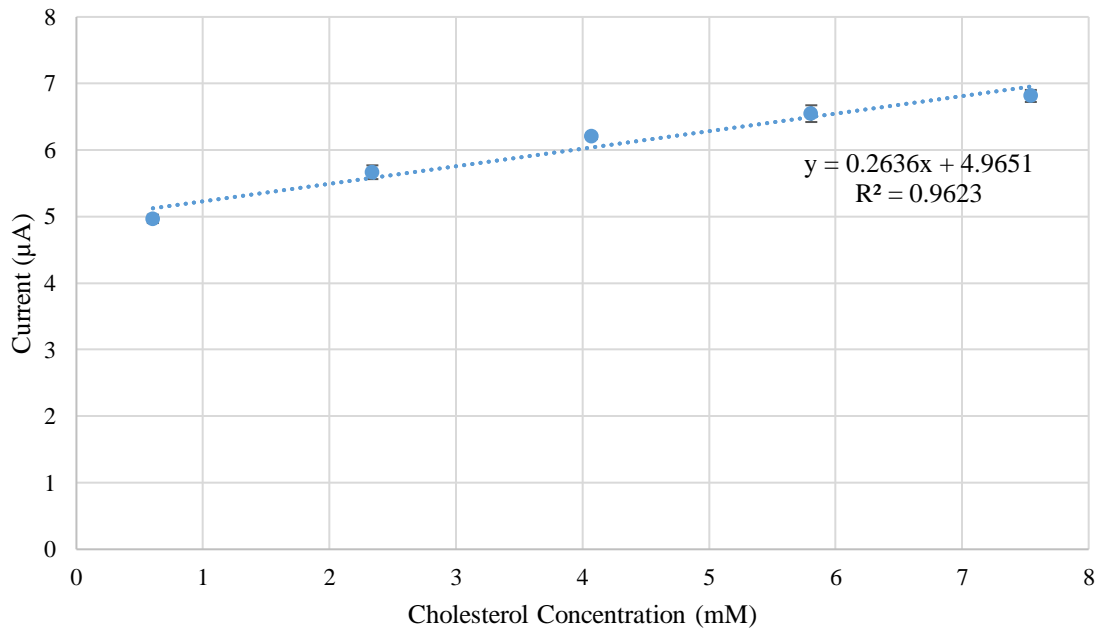
Figure 4.7 Raw data of cholesterol detection testing on Day 3. Sensor was previously tested on Day 0, Day 1, and Day 2. First cholesterol addition added at 60 seconds and a new cholesterol addition made every 60 seconds. The data is an average of 3 experiments.

	Day 0		Day 1		Day 2		Day 3	
	Slope (mA/mM)	R^2	Slope (mA/mM)	R^2	Slope (mA/mM)	R^2	Slope (mA/mM)	R^2
Run 1	-0.47	0.9915	0.04	0.6993	0.17	0.9450	0.25	0.9558
Run 2	-0.28	0.8627	0.13	0.9100	0.19	0.9393	0.28	0.9708
Run 3	-0.21	0.6498	0.16	0.9169	0.28	0.9667	0.26	0.9476
Mean	-0.32	0.8347	0.11	0.8421	0.21	0.9503	0.26	0.9581
Std Dev	0.14	0.1726	0.06	0.1237	0.06	0.0145	0.01	0.0118

Table 4.4 Summary of slope and R^2 data collected on each day of sensor testing.

The graphed raw data from Day 3 testing shows the desired step increases in response to an increase in cholesterol concentration. The respective calibration curve shows good linearity in the response and minimal deviation between the three experiments. The summary of data shows that a negative slope occurred on Day 0 of testing, further confirming this trend, and then shows that the sensitivity, or slope, increased between each experiment and increased between each day of testing prior to Day 3. On Day 3 of testing, the sensitivity is similar between the three experiments, showing a good repeatability in results and an average sensitivity value of 0.26 μA/mM. Additionally, a one-way repeated measure ANOVA with an alpha of 0.05 was used to examine the effect of testing day on sensor sensitivity. This resulted in a P-value of 5.67×10^{-5}. Since the P-value was less than alpha it can be concluded that the day of testing had a statistically significant effect on the sensitivity of the sensor. Further, it was shown that the variance was the lowest on Day 3 of testing with a value of 0.0003 compared to 0.018, 0.004, and 0.003 for Day 0, Day 1, and Day 2, respectively, confirming the greater repeatability of results on Day 3.

An important observation made throughout all testing was the impact of the solution on the reference electrode. Potassium ferricyanide, used as the reaction mediator in solution, causes a reaction with the silver on-chip reference electrode, resulting in a darkening color change. This darkening increases with the more experiments that are performed and likely impacts the repeatability of results. Using an Ag/AgCl on chip or glass external reference electrode might be beneficial to avoid this reaction and improve repeatability.

4.6   Conclusion

Through the detection testing performed on the cholesterol biosensor, it was proven that the microfluidic, chip-based biosensor for cholesterol detection was achieved. It was shown that cholesterol changes could be detected within the physiological range of cholesterol. This cholesterol biosensor provides a firm baseline to improve upon for further testing.

CHAPTER 5.   OXYGEN DETECTION BIOSENSOR

5.1   Introduction

Additional sensing capabilities were explored further with oxygen detection. Oxygen is a critical biomarker associated with not only oxygenation of various tissues and organs but also the redox of many crucial biochemical species in the body. Oxygen monitoring and measurement is a key step in understanding and managing patient care and outcomes, hence playing a critical role in many research fields and project areas. One difficulty facing oxygen detection is dealing with ambient air and interfering external conditions. Combining a chip-based oxygen biosensor with the previously designed microfluidic platform could help in eliminating these difficulties. By sealing the oxygen biosensor to the PDMS platform the environment in which the sensor surface is exposed to is controlled, which is advantageous for results.

For the scope of this project, our goal was to expand further sensing capabilities by creating and testing a chip-based oxygen biosensor. For this reason, the focus of this part of the project was to implement an oxygen detection capability and not to integrate it with the microfluidic platform, which will be delegated for future work.

This chapter discusses the biofunctionalization process of the oxygen biosensor followed by the different methods of testing and the results of each method.

5.2   Sensor Biofunctionalization

Chip sensors composed of three screen printed electrodes (i.e., gold working electrode, gold counter electrode and Ag/AgCl reference electrode) on a polyamide base are used. The biofunctionalization of the working electrode is completed in three steps:

anchoring, hydrogel layer polymerization, and creation of gas permeable membrane. The anchoring step requires the chip sensor be submerged in a 10:1 solution of toluene and 3-(trimethyoxysilyl)propyl methacrylate for 2 hours. The toluene primes the surface of the electrodes for more effective adhesion of the subsequent hydrogel layer. The toluene treated sensor surface is rinsed with ethanol followed by DI water. A hydrogel mixture solution is prepared consisting of 40 wt% acrylamide, 5 wt% N,N'-methylene-bis-acrylamide, 0.1 mg/ml riboflavin 5'-phosphate sodium, 1 ml/mg N,N,N',N'-tetramethyl-ethylenediamine, and 1:1 ratio of water to glycerol. The electrode end of the sensor is placed into the hydrogel mixture for several seconds. A thin sheet of plastic film is used to cover the wetted sensor surface to prevent immediate desiccation and ensure the formation of an even hydrogel layer on the electrode surface. Before removing the plastic film, the electrode is exposed to a UV light source for 30 minutes. A mixture solution consisting of 0.5 wt% 2,2-dimethoxy-2-phenyl-acetophenone dissolved in a 1:5 solution of acetone and methacryloxypropyl methyl siloxane is prepared. This mixture solution is to form a of permeable membrane on top of the hydrogel layer to separate the electrodes from contacting the electrolyte directly while still allowing gas exchange to occur. The residue acetone in the mixture solution is forced out by heated evaporation at 40°C and the solution is allowed to rest to rid of remaining air bubbles. To form the permeable membrane, the electrode end of the sensor is dipped in this permeable-membrane solution mixture for several seconds. Similarly, another piece of plastic film is placed over the solution to ensure an even layer of the permeable membrane formation over the hydrogel layer on the electrode. The sensor is then placed under the UV light for 24 hours, removing the plastic film halfway through. The biofunctionalization process can be seen visually in Figure 5.1.

Bare Top View   Biofunctionalized Cross Section
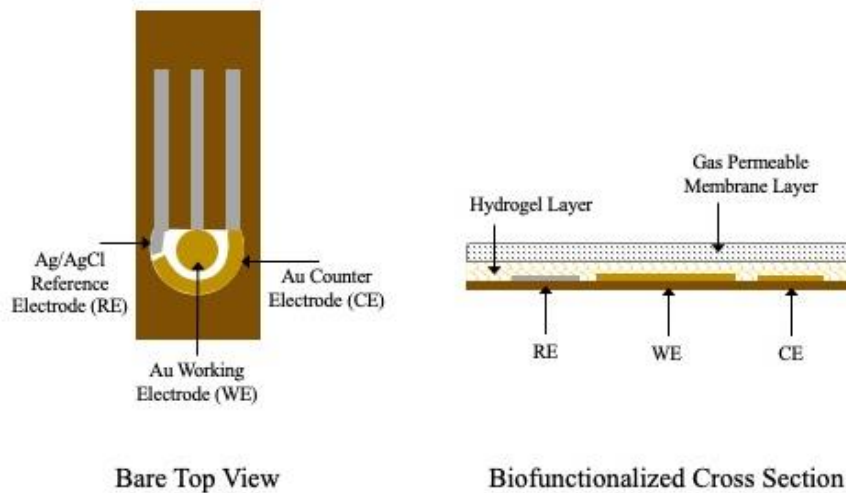
Figure 5.1 Schematic of the biofunctionalization process for the oxygen biosensor.

5.3   Methods for Oxygen Detection

A negative potential is applied to the working electrode to perform the reduction of oxygen at the working electrode, and subsequent oxidation at the counter electrode. This can be visualized by the following reaction:

$$O_2 + 2H^+ + 2e^- \rightarrow H_2O_2$$
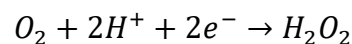
To assess the detection capabilities of the biofunctionalized oxygen detection biosensor four different sets of experiments were conducted using the Keithley 2450 SourceMeter SMU (Tektronix, Beaverton, OR, USA). Experiments were run using a three-electrode setup, utilizing the reference, working and counter electrode on the biofunctionalized sensor:

1. Differing the applied voltage in DI water

2. Differing the applied voltage in 4M KCl solution

3. Applying a constant voltage in different molar solutions of KCl

4. Applying a constant voltage at different pressure settings in a vacuum chamber

The oxygen sensor was first tested under different voltages in two solutions. The first was non-electrolyte DI water and the other is with a solution fixed concentration of electrolyte of 4M KCl. For these tests, the sensor was placed in the respective solution and chronoamperometric experiments were run by applying -0.2 V, -0.3 V, -0.4 V, -0.5 V, and -0.6 V, versus Ag/AgCl reference, to the working electrode for 5 minutes each. The current response at each applied voltage was recorded.

After that, the sensor was tested under a constant voltage in solutions of different molar concentrations of KCl electrolyte: 1M KCl, 2M KCl, 3M KCl, and 4M KCl. For these tests, the sensor was placed in each of the four KCl solutions and chronoamperometric experiments were run by applying -0.5 V, versus Ag/AgCl reference, for 5 minutes each. The current response at each molar concentration of KCl was recorded.

The oxygen sensor was further tested in a controlled pressure chamber under a constant working electrode potential in DI water. To do that, the sensor was placed in a beaker of DI water sitting in a vacuum chamber. Chronoamperometric experiments were run by applying -0.3 V versus Ag/AgCl reference for 2 minutes at six preselected pressure settings: -0.1, -0.2, -0.3, -0.4, -0.5 and -0.6 bar. These pressure readings, converted to mmHg and kPa, along with the corresponding oxygen partial pressure in mmHg are listed in Table 5.1.

Bar	Relative bar	Relative mmHg	O_2 Partial Pressure (mmHg)	kPa
-0.6	0.413	310	65.10	-60
-0.5	0.513	385	80.85	-50
-0.4	0.613	460	96.60	-40
-0.3	0.713	535	112.35	-30
-0.2	0.813	610	128.10	-20
-0.1	0.913	685	143.85	-10

Table 5.1 Pressure conversions and oxygen content for experiments performed on oxygen detection biosensor at different pressures in vacuum chamber.

5.4   Results & Discussion

The raw data of average current response of the oxygen sensor in DI water to changes in voltage is shown in Figure 5.2. The raw data for the other three experimental conditions is given in Appendix B. The response curves follow the trend of the Cottrell decay curve, only reversed, which is to be expected. If a positive potential is applied to the system, the decay curve is the result. Whereas, if a negative potential is applied a saturation curve occurs, as shown in Figure 5.2. This represents what a typical measurement looks like. The steady state current values from the raw data are then used to create the calibration curves. The calibration curve for the oxygen detection performed in DI water is shown in Figure 5.3, and it provides a correlation coefficient of 0.98. This suggests that the magnitude of the current response linearly increases with increasing voltage.
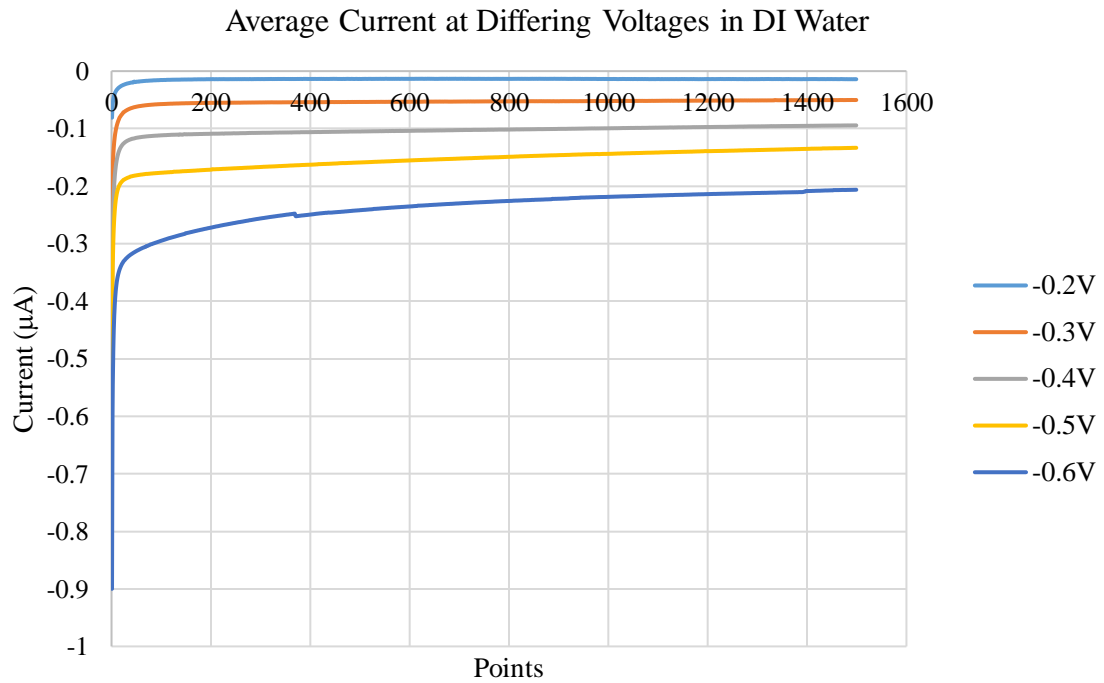
Figure 5.2 Raw data of the amperometric current response of the biosensor in DI water at different applied voltages.
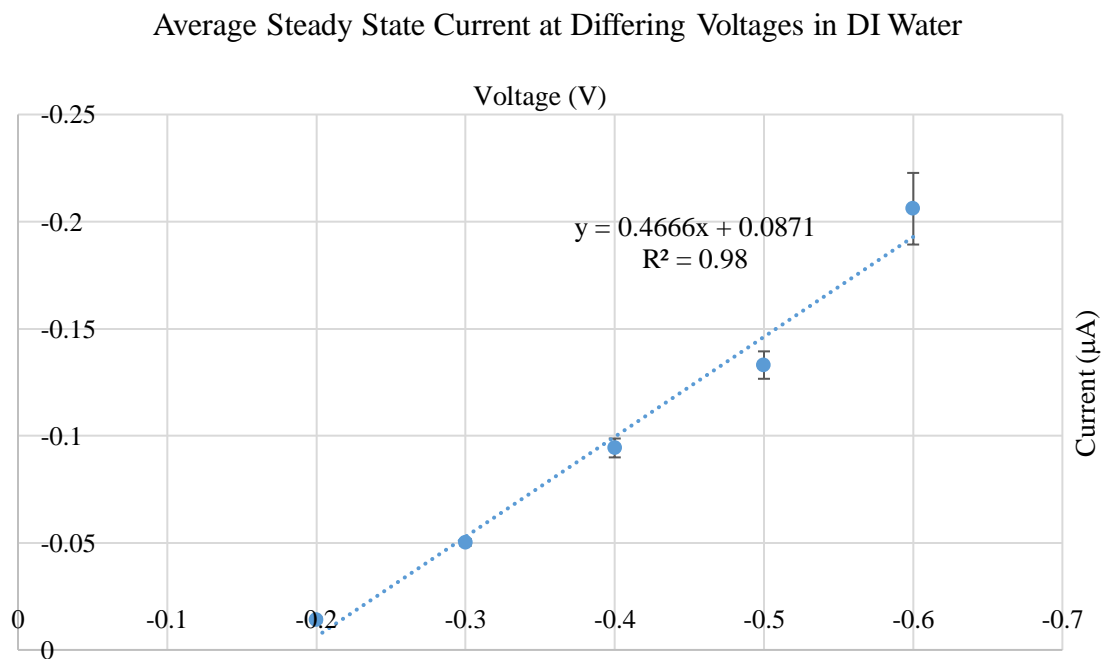
Figure 5.3 Final, steady state average current response of the oxygen biosensor in DI water at different applied voltages.

As compared with the previous results of current response in DI water, the linearity between current response and voltage change in 4M KCl is lower at 0.8889. However, due to the magnitude of the current responses, the slope of the trendline is higher showing a higher sensitivity to changes in oxygen in 4M KCl solution. The sensitivity to change in 4M KCl solution is 142.96% higher than in DI water, indicative of the enhanced mass transport by the presence of the electrolyte.

Average Steady State Current at Differing Votlages in 4M KCl Solution
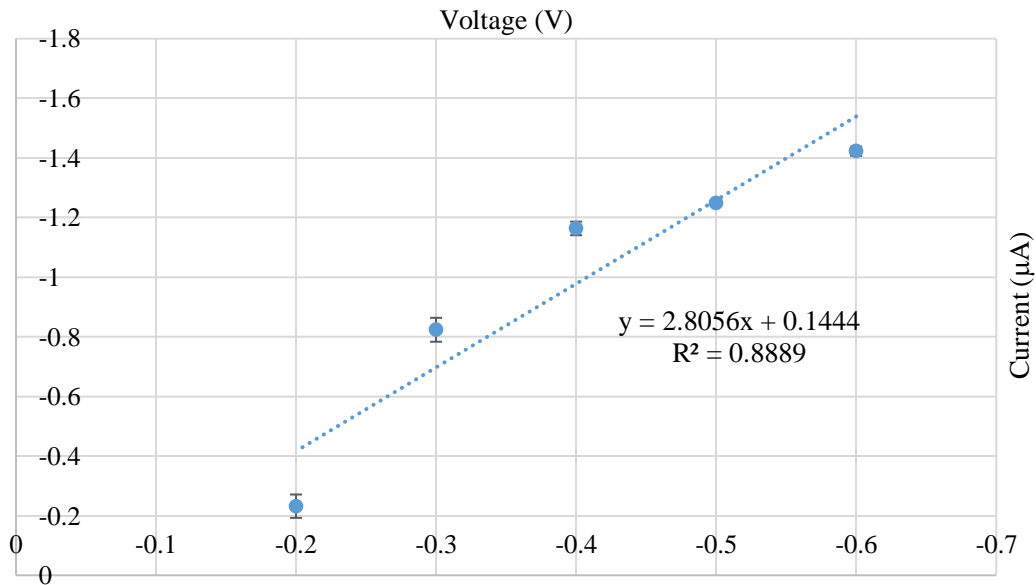
Figure 5.4 Final, steady state average current response of the oxygen biosensor in 4M KCl solution at different applied voltages.

The calibration curve in response to the oxygen detection performed in different molarities of KCl solution is shown in Figure 5.5. This provides a correlation coefficient of 0.9814, indicating a linear correlation between KCl concentration and current response. As the molarity of the KCl solution was increase, the magnitude of the resulting current response also increased.

Steady State Current at Differing Molarities KCl Solution
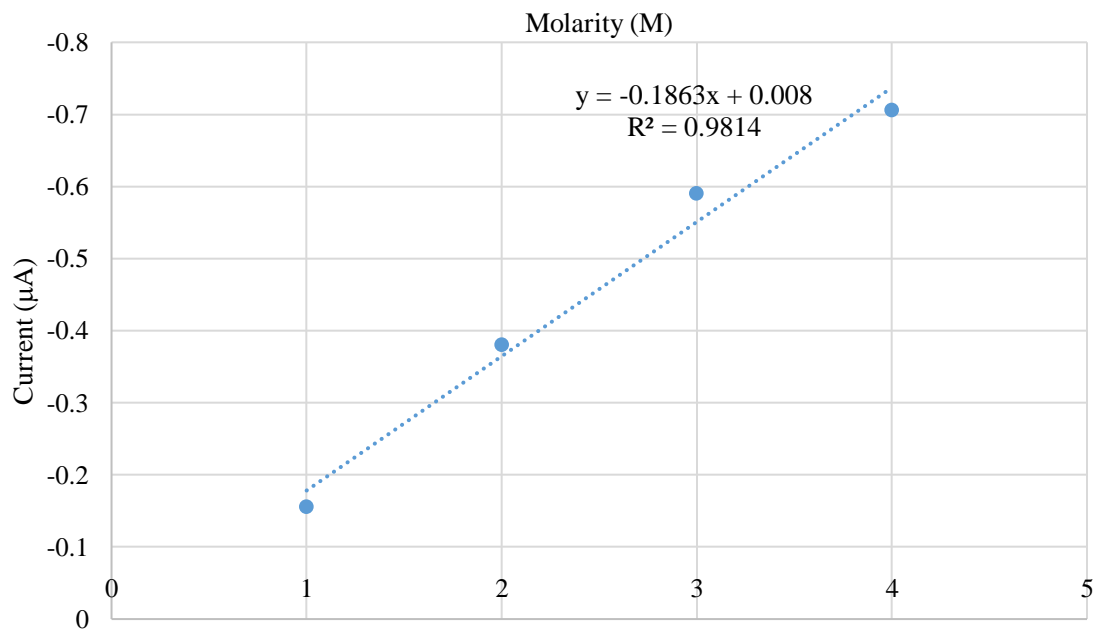
Figure 5.5 Final, steady state average current response of the oxygen biosensor in different molar concentrations of KCl solution.

For measurements taken at different pressure settings in a vacuum chamber, the pressure was converted from Bar (unit of vacuum chamber) to mmHg (oxygen content) and steady state current was plotted against this value (Figure 5.6). The linearity was high, 0.9842, indicating a linear relationship between current and pressure, and therefore a linear relationship between current and oxygen concentration. As the oxygen content increases, the magnitude of the current increases, showing that the oxygen detection sensor is functioning properly in detecting changes in oxygen. The normal arterial oxygen partial pressure is within 75-100 mmHg. The results confirm the capability of the developed oxygen sensor to detect changes in oxygen content within this physiological range.
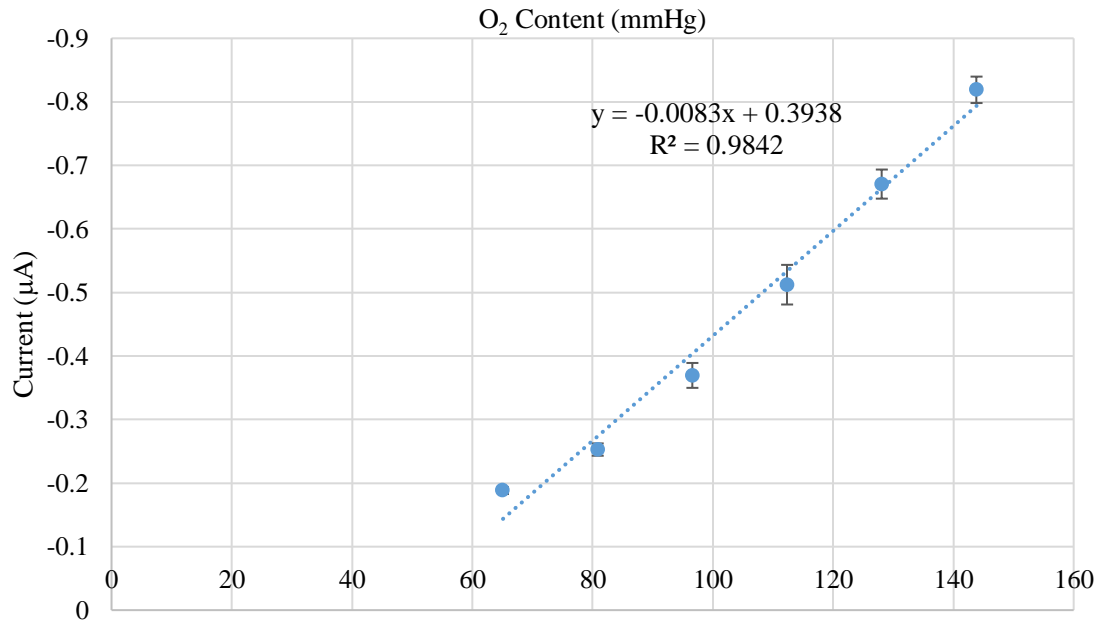
Figure 5.6 Final, steady state average current response at different amounts of oxygen content. The reading, in units of Bar, on the vacuum chamber was converted to mmHg to determine oxygen content.

5.5   Conclusion

Through the different tests performed to the oxygen biosensor, it was shown that the

biosensor could detect changes in oxygen concentration in solution.

CHAPTER 6.   CONCLUSIONS AND FUTURE WORK

6.1   Conclusions

This work has demonstrated the success of a microfluidic, chip-based biosensor for the detection of different critical biomarkers. Through the timeline of this project and the effort for continuous improvement, we were able to combine microfluidics with an amperometric biosensor. We were also able to prove the capability of the biosensor to detect different targets, mainly glucose, cholesterol, and oxygen. This design provides a desirable platform due its reusability, the small volume of solution needed, and the continuous flow of solution, which would allow for continuous monitoring in a research and clinical setting. Additionally, this platform would provide a more cost effective and easy-to-deploy method for biomarker detection than what is currently used for the measurement and monitoring of many critical biomarkers.

6.2   Future Work

Further evaluation should be done on the cholesterol biosensor to optimize the pre-conditioning and testing timeline of the sensor for improved sensitivity. Additionally, modifications should be made to the reference electrode to prevent the reaction with the mediator in solution and improve the repeatability of results. This could be done by modifying the on-chip electrode or adapting the microfluidic platform design to include an external glass reference electrode.

An optimal design would include the possibility to perform detection of multiple biomarkers simultaneously, or a multi-target device. To facilitate this, future work includes expansion of the current microfluidic, chip-based platform design to create a device

consisting of multiple functionalized sensors to allow for simultaneous biomarker detection and monitoring. This would allow for glucose, cholesterol, and oxygen detection and monitoring within one device. Based on the intended use and what is needed, the detection of other biomarkers using this platform should be explored. This could provide a device that can be customized based on the multi-target detection needs.

Further testing should also be done to evaluate the specificity of the biosensors to the biomarker in question to examine their practical application capabilities. Testing of each biosensor was performed without or with minimal potential interference substances in solution. It is important to test these further to determine the sensors response when multiple substances are present in solution, such as in human blood or serum.

6.3 APPENDIX A. OXYGEN SENSOR RAW DATA
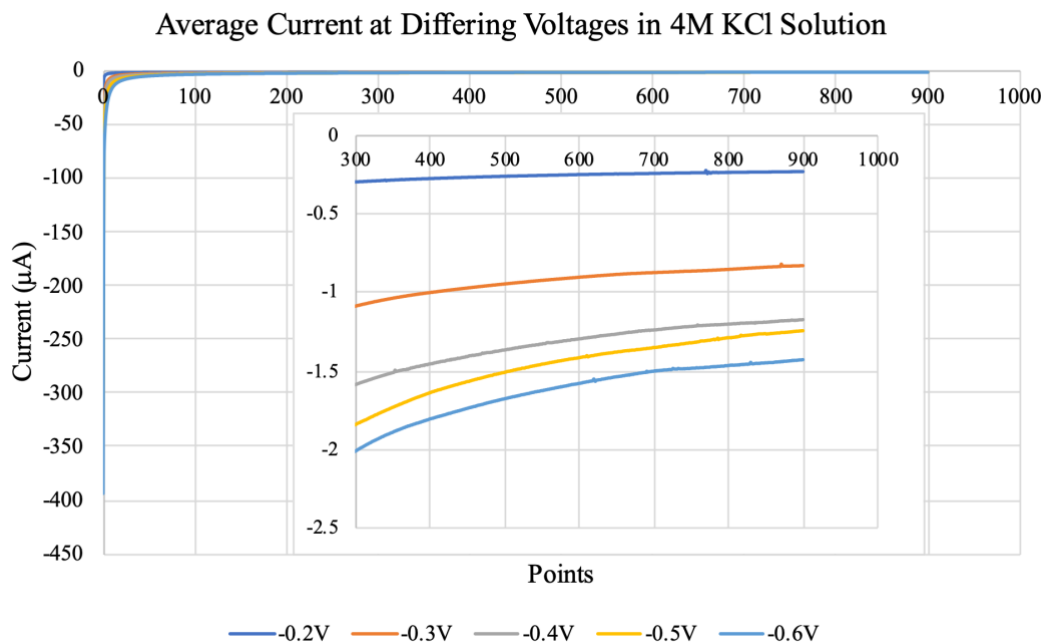
Average Current at Differing Voltages in 4M KCl Solution

Raw data of the amperometric current response of the biosensor in 4M KCl solution at different applied voltages.

Current at 1M, 2M, 3M & 4M KCl Solution
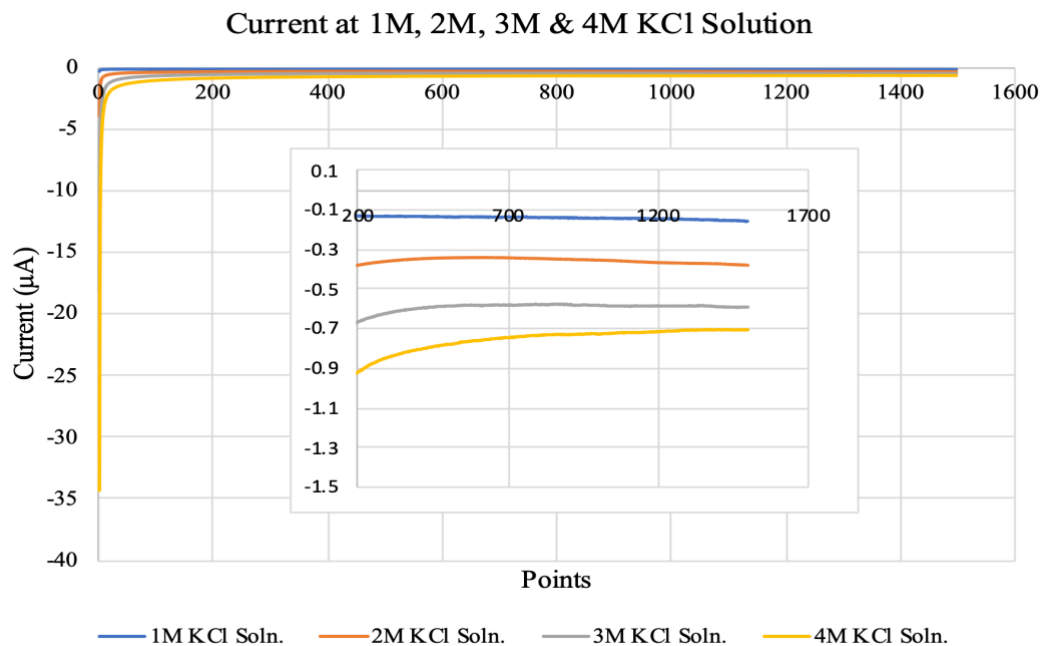
Raw data of the amperometric current response of the biosensor in different molarities of KCl solution at a constant applied voltage.
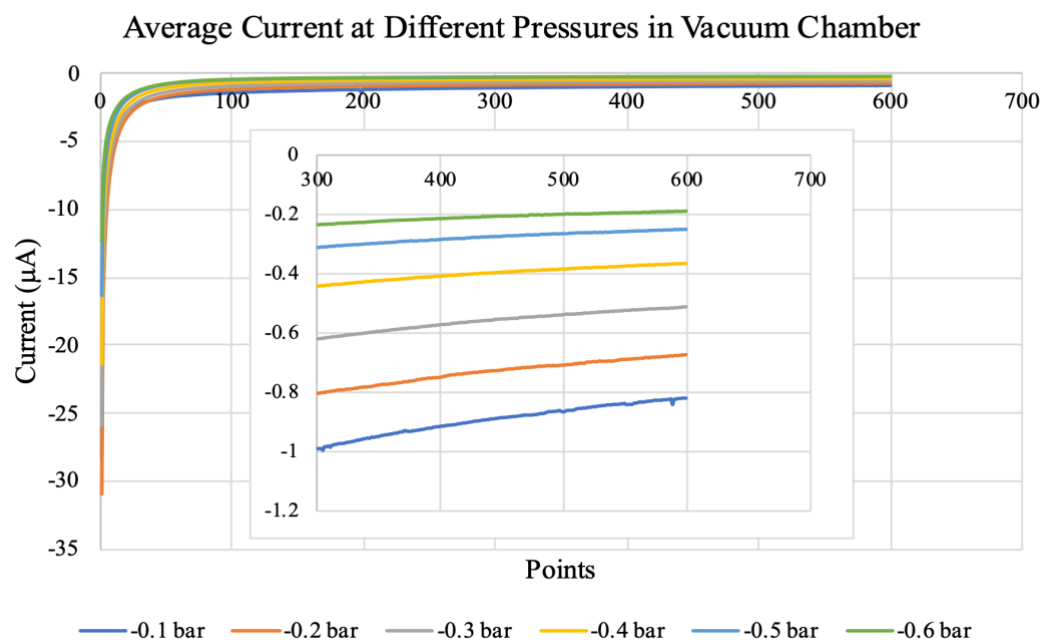
Raw data of the amperometric current response of the biosensor in DI water at different pressures in a vacuum chamber.

6.4   APPENDIX B. LABORATORY PROCEDURES

RCA-1 Cleaning Procedure for Sensor

Solution: 5 parts water, 1 part NH4OH, 1 part H2O2

Procedure:
1. Add 10 mL DI water and 2 mL 27% ammonium hydroxide (NH4OH) to Pyrex glass beaker.
2. Heat to 70 +/- 5 degrees Celsius on hot plate (~25 min. using hot plate with external temp. probe).
3. Once heated, turn off hot plate and add 2 mL 30% hydrogen peroxide (H2O2).
4. Solution will bubble vigorously after 1-2 min., indicating its ready for use.
5. Using a Q-tip, add solution to only the working and counter electrode. Every 3 minute remove the solution with the Q-tip and replace the solution. Continue this for a total of 15 minutes.
6. Transfer solution to a beaker with cold water to cool.
7. Rinse the sensor multiple times with DI water and let dry.
8. Once solution in DI water has cooled, pour down the drain with plenty of cold water to flush (let water run for 5 minutes). Rinse all lab ware 3 times in cold water.

Glucose Sensor Functionalization – Beaker Method

Procedure:
1. Chill 5mL PBS in the 10mL glass beaker in the refrigerator for 5 minutes.
2. Remove and use spoon scoop to weigh and add 0.005g of GOx, stir solution.
3. Use the pipet to add 35 µL of pyrrole and thoroughly stir solution.
4. Tape over the counter and reference electrodes of the sensor with scotch tape
5. Turn on the potentiostat.
6. Connect the working/working sense lead of the potentiostat together and connect to the working wire of the sensor cable and place the sensor in the beaker solution.
7. Connect the reference/counter lead together and connect to the platinum gauze and place the gauze into the solution, close to the working electrode without touching it.
8. Run a chronopotentiometry experiment at 10µA, 0.2 time per point, for 420 seconds for AT electrode and 270 seconds for BT electrodes.
   a. The deposition should be as even as possible and darkened but not completely (gold should still be visible through) (AT left, BT right).
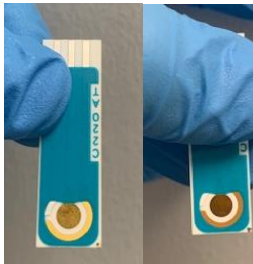
Glucose Sensor Functionalization – PDMS Well Method

Procedure:
1. Create the deposition solution by adding 0.002g of glucose oxidase (GOx) and 14.4µL of pyrrole to 1mL chilled PBS in a 10mL glass beaker, thoroughly stir solution.
2. Put solution into syringe with purple blunt tip needle.
3. Cut a piece of conductive tape in half lengthwise (to make it thinner) and wrap around the needle leaving excess to be attached to the counter lead, folding over to hide sticky section.
4. Turn on the potentiostat and connect the working and working sense leads together and the reference and counter leads together.
5. Secure the PDMS well to the sensor by using the clamps and wood board, and connect the sensor to the CAC cable.
6. Secure syringe to clamp on the stand and lower into the PDMS well, close to the working electrode without touching it.
7. Attach the counter/reference lead to the conductive tape and the working/working sense lead to the working lead of the CAC cable.
8. Press the syringe to fill the well with solution (initially fill ½ to ¾ of the way full)
    a. The needle should be partially submerged, and the solution shouldn't touch the conductive tape.
9. Choose new chronopotentiometry experiment.
10. Run a chronopotentiometry experiment at 10µA in 1-minute increments.
    a. After each minute increase the liquid in the well.
    b. Every 3 minutes remove solution from well with a separate syringe and refill the well.
    c. Visually inspect working electrode after minute runs. Should be darkened but still visible gold showing through.

Glucose Detection – Low Glucose Concentration Range (Beaker Method)

Procedure:
1. Make a 0.1M PBS solution containing 3mM p-Benzoquinone by adding 0.0066g of p-Benzoquinone to 20mL PBS in a 20mL glass beaker.
2. Remove the functionalized sensor from the refrigerator and clip sensor into the CAC cable and place sensor inside the 10mL beaker. Ensure the sensor remains vertical.
3. Using a 1mL syringe, add 5mL of the PBS/p-Benzoquinone solution to the beaker with the sensor.
4. Turn on the potentiostat and allow a minute for boot up.
5. Open up the VersaStudio software and select choose instrument. Choose the corresponding instrument. Create a new experiment and choose chronoamperometry.
6. Attach the 3 potentiostat leads to the 3 sensor cable leads.

7. The sense lead should be connected to the working lead and both ground cables should be left disconnected.
8. Let the sensor sit in the solution, connected, for pre-conditioning for 30 minutes.
9. During the 30 minutes – In a separate beaker, create a 1M glucose solution by adding 0.9008g of glucose to 5mL DI water.
10. After the 30 minutes – on the VersaStudio screen – enter in the following parameters: Potential (V) = 0.35V vs ref, Time Per Points (s) = 0.2, Duration (s) = 1500
11. Leave all other parameters as is
12. Start the experiment by pressing the run button in VersaStudio.
13. Let run for 15 minutes (900 seconds) for current to even out, then add glucose solution to the beaker on the 15-minute mark.
    a. 5 µL additions for physiological range
    b. Larger additions for higher range (use glucose concentration calculator for desired amount)
14. Make additions of glucose solution each consecutive minute.
15. Perform manual stirring using the pipette.
16. Save and copy data and paste into excel.
17. Return the sensor back to dry refrigerator storage (in Ziploc bag) after use.

Glucose Detection – High Glucose Concentration Range (24-Well Plate Method)

Procedure:
1. Make a 0.1M PBS solution containing 3mM p-Benzoquinone by adding 0.0033g of p-Benzoquinone to 10mL PBS in a 20mL glass beaker.
2. Remove the sensor from the refrigerator and clip sensor into the CAC cable and place sensor inside one of the wells on the plate. Ensure the sensor remains vertical.
3. Using a 1mL syringe, add 1.5mL of the PBS/p-Benzoquinone solution to the well with the sensor.
4. Turn on the potentiostat and allow a minute for boot up.
5. Open up the VersaStudio software and select choose instrument. Choose the corresponding instrument. Create a new experiment and choose chronoamperometry.
6. Attach the 3 potentiostat leads to the 3 sensor cable leads.
7. The sense lead should be connected to the working lead and both ground cables should be left disconnected.
8. Let the sensor sit in the solution with continuous measurement for 30 minutes.
9. During the 30 minutes – In a separate beaker, create a 1M glucose solution by adding 0.9008g of glucose to 5mL DI water.
10. After the 30 minutes – on the VersaStudio screen – enter in the following parameters: Potential (V) = +0.35V vs ref, Time Per Points (s) = 0.2, Duration (s) = 1500.
11. Leave all other parameters as is.
12. Start the experiment by pressing the run button in VersaStudio.
13. Let run for 15 minutes (900 seconds) for the current to level out, then add 30µL of glucose solution to the well on the 15-minute mark.

14. Make 30 µL additions of glucose solution each consecutive minute.
15. Perform manual stirring using the pipette.
16. Save and copy data and paste into excel.
17. Return the sensor back to dry refrigerator storage (in a Ziploc bag) after use.

Glucose Detection – Manual Solution Flow

This method utilizes the liquid capacity of the sensor when lying flat on a surface.

Procedure:
1. Make a 0.1M PBS solution containing 3mM p-Benzoquinone by adding 0.0066g of p-Benzoquinone to 20mL PBS in a 20mL glass beaker.
2. In a 10mL beaker, create a 1M glucose solution by adding 0.9008g of glucose to 5mL DI water.
3. Create 10 different solutions using the solutions above and the below chart:

Solution #	PBS soln. (mL)	Glucose (µL)	Molarity (mol/L)	Clinical (mg/dL)
1	1.5	5	0.0033223	59.8
2	1.5	7	0.0046451	83.6
3	1.5	9	0.0059643	107.4
4	1.5	11	0.0072801	131
5	1.5	15	0.0099012	178.2
6	1.5	20	0.0131582	236.8
7	1.5	25	0.0163938	295.1
8	1.5	35	0.0228018	410.4
9	1.5	45	0.0291269	524.3
10	1.5	50	0.0322588	580.7

4. Remove the functionalized sensor from the refrigerator, attach to the CAC cable and secure flat to the platform.
5. Turn on the potentiostat and allow a minute for boot up.
6. Open up the VersaStudio software and select choose instrument. Choose the corresponding instrument. Create a new experiment and choose chronoamperometry.
7. Attach the 3 potentiostat leads to the 3 sensor cable leads.
8. Using a pipette, dispense 70 µL of the PBS/p-benzoquinone solution onto the sensor.
9. Let sit for pre-conditioning for 5 minutes.
10. On the VersaStudio screen – enter in the following parameters: Potential (V) = +0.35V vs ref, Time Per Points (s) = 0.2, Duration (s) = 900 (15 minutes)

11. Start the experiment by pressing the run button in VersaStudio.
12. Let the experiment run for 300 seconds (5 min) to allow the current to even out, then at 300 seconds use two pipettes to replace the solution (1 to remove the solution on the sensor and the 2nd to add the new concentration), continue this on each minute mark, increasing the concentration as you go.
13. Rinse the sensor with DI water and store in a ziploc bag in the refrigerator.

Glucose Detection – Microfluidic, Chip-Based

Procedure:
1. Make a 0.1M PBS solution containing 3mM p-Benzoquinone by adding 0.0066g of p-Benzoquinone to 20mL PBS in a 20mL glass beaker.
2. In a 10mL beaker, create a 1M glucose solution by adding 0.9008g of glucose to 5mL DI water.
3. Create 10 different solutions in 10 separate beakers using the solutions above and the below chart:

Solution #	PBS soln. (mL)	Glucose (µL)	Molarity (mol/L)	Clinical (mg/dL)
1	1.5	5	0.0033223	59.8
2	1.5	7	0.0046451	83.6
3	1.5	9	0.0059643	107.4
4	1.5	11	0.0072801	131
5	1.5	15	0.0099012	178.2
6	1.5	20	0.0131582	236.8
7	1.5	25	0.0163938	295.1
8	1.5	35	0.0228018	410.4
9	1.5	45	0.0291269	524.3
10	1.5	50	0.0322588	580.8

4. Attach the sensor/microfluidic platform to the pump and CAC cable.
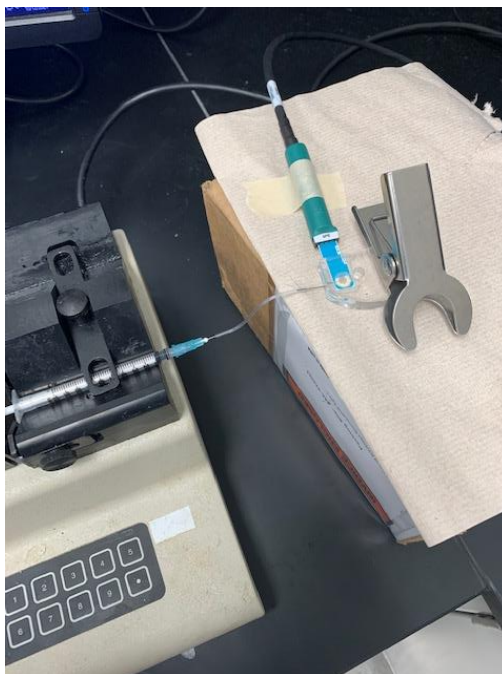
5. Pump through 100 microL of PBS/p-Benzoquinone solution to cover the electrodes and stop the pump right before the well empties of solution. Perform preconditioning for 5 minutes by connecting the CAC cable leads to the working, counter and reference leads of the PARSTAT MC and letting sit for 5 minutes.
6. Start a new chronoamperometry experiment at +0.35V, 0.2 time per points, and 900 seconds
7. At 300 seconds, add 100 microL of the first PBS/p-Benzoquinone/glucose addition solution and start the pump
8. Add 100 microL on each minute after, increasing from the lowest to highest concentration.
9. Save, copy and paste data into excel.
10. Store the sensor attached to the PDMS platform in the refrigerator.

Cholesterol Sensor Functionalization

Procedure:
1. Create the deposition solution by adding one 25U bottle of cholesterol oxidase (ChOx) and 14.4µL of pyrrole to 1mL chilled PBS in a 10mL glass beaker, thoroughly stir solution.
2. Put solution into syringe with purple blunt tip needle.
3. Cut a piece of conductive tape in half lengthwise (to make it thinner) and wrap around the needle leaving excess to be attached to the counter lead, folding over to hide sticky section.
4. Turn on the PARSTAT MC and connect the working and working sense leads together and the reference and counter leads together.

5. Secure the PDMS well to the sensor by using the clamps and wood board, and connect the sensor to the CAC cable.
6. Secure syringe to clamp on the stand and lower into the PDMS well, close to the working electrode without touching it.
7. Attach the counter/reference lead to the conductive tape and the working/working sense lead to the working lead of the CAC cable.
8. Press the syringe to fill the well halfway with solution.
   a. The needle should be partially submerged, and the solution shouldn't touch the conductive tape.
9. Choose new chronopotentiometry experiment.
10. Run a chronopotentiometry experiment at 10µA in 1-minute increments for 7-8 minutes depending on visual inspection.
   a. After each minute increase the liquid in the well. Should follow the pattern: half filled, run experiment, fully filled, run experiment, run experiment again fully filled, then remove solution and replace to half filled with new solution.
   b. So, every 3 minutes remove solution from well with a separate syringe and refill the well
   c. Visually inspect working electrode after minute runs. Should be darkened but still visible gold showing through.

Cholesterol Detection – Microfluidic, Chip-Based

Procedure:
1. The Verichem Matrix Plus Cholesterol Reference kit is used for the cholesterol testing concentrations.
2. Using 5 separate 10mL glass beakers, dispense 5 drops (~140µL) of each solution into each beaker.
   a. Before dispensing of each solution into the individual beakers, drop one drop from each bottle into a beaker for later disposal.
3. The 5 different solutions are pre-determined as follows:

Solution Level	Cholesterol (mg/dL)	Cholesterol (M)	Uric Acid (mg/dL)
A	40	0.001034	2
B	155	0.004008	7
C	270	0.006982	12
D	385	0.009956	17
E	500	0.012930	22

4. Create supporting electrolyte / redox mediator solution by adding 0.033 g of potassium ferricyanide to 10 mL PBS and mix. This is a 10mM $[Fe(CN6)]3-$ solution.

5. Add 100 μL of the solution in step 4 into each individual beaker from step 2 and mix.
6. Attach the sensor/microfluidic platform to the pump and CAC cable.
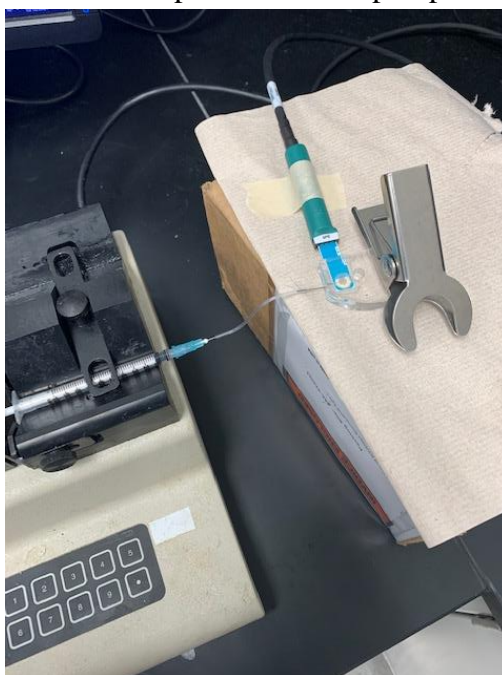
7. Set the pump to a withdraw rate of 0.2 mL/min and pump through 300 μL of the solution from step 4 to cover the electrodes and stop the pump right before the well empties of solution. Perform preconditioning for 45 minutes by connecting the CAC cable leads to the working, counter and reference leads of the PARSTAT MC and letting sit for 45 minutes.
8. Start a new chronoamperometry experiment at +0.60V, 0.2 time per points, and 600 seconds.
    a. IMPORTANT: set the current range to 20 μA. Don't leave it on auto.
9. At 60 seconds, add 200 μL of the first cholesterol addition solution and start the pump (this is two separate 100 μL additions).
10. Add 200 μL on each minute after, increasing from the lowest to highest concentration.
11. Save, copy and paste the data into excel.
12. Store the sensor attached to the PDMS platform in the refrigerator.

Oxygen Sensor Functionalization

Procedure:
Anchoring method
1. 20mL of toluene and 2mL of 3-(trimethyoxysilyl)propyl methacrylate were added to a 20 mL beaker.

2. Submerge the electrode in the beaker (make sure all electrodes are covered) for at least 2 hours.
3. Remove the electrode from solution and rinse with ethanol, then with DI water.
4. Let air dry before adding hydrogel layer.

Hydrogel Layer
1. Add 2.5 mL of DI water to a 20 mL beaker.
2. Add a stir bar and place the beaker on a stir plate.
3. Add 2.264g of acrylamide to the beaker and stir until completely dissolved.
4. Add 0.269g of N, N'-methylene-bis-acrylamide to the beaker and stir until completely dissolved.
5. Add 2.5 mL of glycerol to the beaker and stir until dissolved.
6. Add 0.0051g of Riboflavin 5'-phosphate sodium and 6 μL of N, N, N', N'-tetramethyl-ethylenediamine into the beaker and stir until dissolved (After these two chemicals are added, speed is necessary as the hydrogel will start to polymerize quickly. Make sure the electrode is ready before adding these two chemicals).
7. As soon as the Riboflavin 5'-phosphate sodium and N, N, N', N'-tetramethyl-ethylenediamine dissolve, stick the electrode end of the sensor into the hydrogel mixture.
8. After several seconds, pull the electrode out.
9. Make sure the hydrogel is in an even, thin layer by placing a small piece of plastic film over the hydrogel layer.
10. Place the electrode under a UV light source for 30 minutes.
11. Make the permeable membrane solution while you are waiting for the hydrogel to polymerize.
12. Remove the thin film from the electrode.

Permeable Membrane
1. Add 0.0261g of 2,2-dimethoxy-2-phenyl-acetophenone into a 20 mL beaker.
2. Add 1 mL of acetone to the beaker and stir, by hand, until dissolved.
3. Add 5 mL of Methacryloxypropyl methyl siloxane (measure with a graduated cylinder) into the beaker and stir by hand.
4. Place the beaker in a 40°C oven to evaporate the acetone.
5. The beaker needs to rest, wrapped in aluminum foil until the bubbles created during stirring disappear.
6. Place the electrode end of the sensor into the membrane mixture.
7. After several seconds, pull the electrode out and let the excess mixture drip off.
8. Place a piece of the plastic film over the membrane and carefully smooth the surface until an even thin film forms over the hydrogel.
9. Place the electrode under a UV light source for 12 hours.
10. Remove the thin film and leave the sensor under the light source for 12 hours.
11. Attach wires to each electrode strip using conductive tape.
12. Cover the connected wires with microstop to seal.

Oxygen Sensor Testing – Applying Different Voltages

Procedure:

Testing in DI water:
1. Place sensor inside the 10mL beaker containing 5mL DI water.
2. Turn on the potentiostat and allow a minute for boot up.
3. Open up the VersaStudio software and select choose instrument. Choose the corresponding instrument. Create a new experiment and choose chronoamperometry.
4. Attach the 3 potentiostat leads to the 3 wires attached to the sensor.
5. The sense lead should be connected to the working lead and both ground cables should be left disconnected.
6. Let the sensor sit connected for pre-conditioning for 3 minutes.
7. On the VersaStudio screen – enter in the following parameters: Time Per Points (s) = 0.2, Duration (s) = 300
a. The voltage changes with each experiment: -0.2V, -0.3V, -0.4V, -0.5V, and -0.6V
8. Leave all other parameters as is.
9. Start the experiment by pressing the run button in VersaStudio.
10. Save and copy data and paste into excel.
11. Store the sensor in a Ziploc bag at room temperature.

Testing in 4M KCl solution:
1. Make a 4M KCl solution in DI water in a 20mL beaker with 5.964g KCl and 20mL DI water.
2. Turn on the potentiostat and allow a minute for boot up.
3. Open up the VersaStudio software and select choose instrument. Choose the corresponding instrument. Create a new experiment and choose chronoamperometry.
4. Attach the 3 potentiostat leads to the 3 wires attached to the sensor and place sensor inside the beaker containing 4M KCl.
5. The sense lead should be connected to the working lead and both ground cables should be left disconnected.
6. Let the sensor sit connected for pre-conditioning for 3 minutes.
7. On the VersaStudio screen – enter in the following parameters: Time Per Points (s) = 0.2, Duration (s) = 300
a. The voltage changes with each experiment: -0.2V, -0.3V, -0.4V, -0.5V, and -0.6V
8. Leave all other parameters as is.
9. Start the experiment by pressing the run button in VersaStudio.
10. Save and copy data and paste into excel.
11. Store the sensor in a Ziploc bag at room temperature.

Oxygen Sensor Testing – Constant Voltage in Different Molarities of KCl Solution

Procedure:
1. Make a 4M KCl solution in DI water in a 20mL beaker by adding 5.964g KCl to 20mL DI water.

2. Stir using stir bar until fully dissolved.
3. Turn on the potentiostat and allow a minute for boot up.
4. Open up the VersaStudio software and select choose instrument. Choose the corresponding instrument. Create a new experiment and choose chronoamperometry.
5. Attach the 3 potentiostat leads to the 3 wires attached to the sensor and place the sensor in the beaker containing KCl solution.
6. The sense lead should be connected to the working lead and both ground cables should be left disconnected.
7. Let the sensor sit connected for pre-conditioning for 3 minutes.
8. On the VersaStudio screen – enter in the following parameters: Voltage = -0.5V, Time Per Points (s) = 0.2, Duration (s) = 300
9. Leave all other parameters as is.
10. Start the experiment by pressing the run button in VersaStudio.
11. Save and copy data and paste into excel.
12. Repeat steps 1-12 for different molarities of KCl dissolved in 20mL DI water:
    a. 1M: 1.491g KCl
    b. 1.5M: 2.237g KCl
    c. 2M: 2.982g KCl
    d. 2.5M: 3.7275g KCl
    e. 3M: 4.473g KCl
    f. 3.5M: 5.2185g KCl
13. Store the sensor in a Ziploc bag at room temperature.

Oxygen Sensor Testing – Different Pressures in a Vacuum Chamber

Procedure:
1. Create the seal on the rim of the vacuum chamber by placing a piece of scotch tape over the rim (a couple inches across) and placing a thin layer of putty over the tape.
2. Place the sensor in a beaker of DI water inside the vacuum chamber and seal the chamber to -0.8 bar.
3. Place putty externally around where the sensor and tape are.
4. Connect the three wires attached to the sensor to the three leads of the potentiostat.
5. Decrease the vacuum to –0.1 bar.
6. Let the connected sensor sit for pre-conditioning for 5 minutes.
7. Run a chronoamperometry experiment at -0.3V for 120 seconds.
8. Copy and Save data.
9. Repeat steps 6-8 at -0.2, -0.3, -0.4, -0.5, and -0.6 bar.

PDMS Well

Procedure:
Platform Setup:
1. Attach multiple 3D wells, spread out, to the petri dish using silicone sealant

PDMS:

1. Use the scale to measure out a 10:1 ratio of silicone elastomer base to elastomer curing agent in a weigh dish.
2. Stir the solution until mixed (will be very bubbly) for 5-10minutes depending on how much you make.
3. Pour the solution into two centrifuge tubes (equal amounts in each tube) (if more tubes are needed use an even number so that its symmetrical in the centrifuge machine).
4. Place the tubes symmetrically into the centrifuge.
5. Run the centrifuge at 3200 rpm for 2 minutes.
6. Remove the tubes from the machine. The bubbles should be removed, and the solution should be clear.

PDMS pouring:
1. Pour the PDMS into the petri dish until in line with the top of the 3D printed wells.
2. Ensure there are no bubbles in the PDMS from pouring. The small bubbles will disperse on their own. A needle can be used to extract the large bubbles if necessary.
3. Leave to fully cure for 48 hours.

Removal:
1. Once fully cured, remove the PDMS from the petri dish (this can be done using a blade and going around the edges or by breaking the petri dish).
2. The 3D printed wells can then be removed gently by hand and the PDMS can be cut into individual PDMS wells.
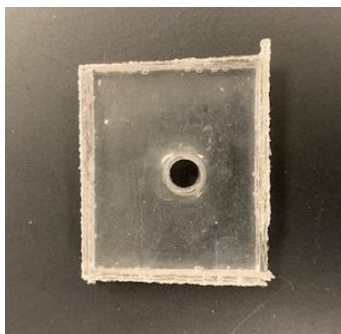
PDMS Microfluidic Platform

Procedure:
Platform Setup:
1. Mold the inlet channels using the 0.5mm extruded PLA material and the soldering iron. Attach the 0.5mm bar to the end of the soldering iron using masking tape and turn the soldering iron on to setting 3.
2. Once heated, take the 0.5mm extruded PLA and bend over the 0.5mm bar to form a 90-degree angle. Remove quickly and hold in shape until cooled (a few seconds). Do this twice so that you have two inlet channels.
3. Cut straight pieces of the 0.5mm extruded PLA material to use as the outlet channels.
4. To attach the channels to the disk, dip the section you want to attach into the acetone and place it onto the disk. It will attach as it dries. Do this for the inlet and outlet channels. Stagger the inlet and outlet channels on the disk so they are not directly in line with each other
5. Attach the channels and disk to the sensor by placing a small amount of silicone sealant on the working electrode and placing the disk on top. Press firmly to ensure placement.
6. Secure each sensor to the petri dish by placing silicone sealant on the back of the sensor and placing the sensor on the petri dish. Press firmly to ensure placement.
7. The two sensors should be placed in opposite directions.
8. Let the acetone completely evaporate while you make the PDMS.
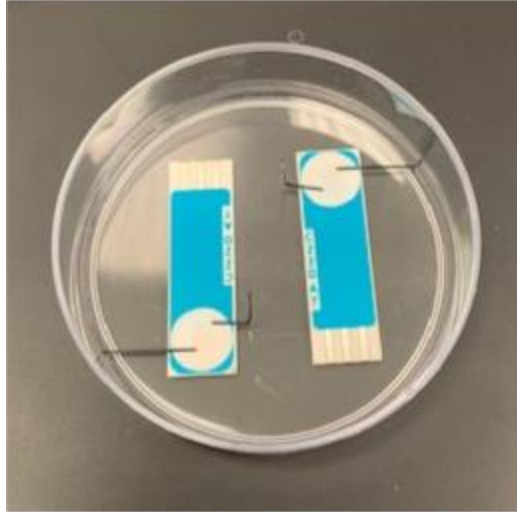
PDMS:

1. Use the scale to measure out a 10:1 ratio of silicone elastomer base to elastomer curing agent in a weigh dish.
2. Stir the solution until mixed (will be very bubbly) for 5-10minutes depending on how much you make.
3. Pour the solution into two centrifuge tubes (equal amounts in each tube) (if more tubes are needed use an even number so that its symmetrical in the centrifuge machine).
4. Place the tubes symmetrically into the centrifuge.
5. Run the centrifuge at 3200 rpm for 2 minutes.
6. Remove the tubes from the machine. The bubbles should be removed, and the solution should be clear.

First Round of PDMS:

1. Pour the PDMS into the petri dish covering the sensor chips and disks. The petri dish should be about half full.
2. Ensure there are no bubbles in the PDMS from pouring. The small bubbles will disperse on their own. A needle can be used to extract the large bubbles if necessary.
3. Leave to partially cure for ~24 hours.
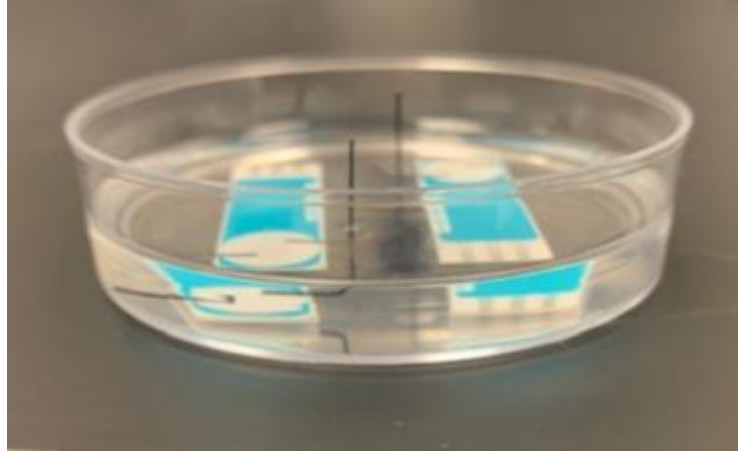
Second Round of PDMS:
1. Once the first pour is partially cured, 3D printed PLA wells need to be placed. The PDMS is still sticky when partially cured, which allows the PLA wells to be placed without moving.
2. Cut down the PLA to be in line with the PDMS.
3. Place each PLA well centered above the inlet channels for each. Press slightly to ensure the well is in place on the sticky PDMS.
4. Make another batch of PDMS following the above steps.
5. Pour the PDMS on top of the partially cured PDMS. Stop pouring once the PDMS is in line with the top of the PLA well.
6. Remove any bubbles if necessary.
7. Let the PDMS cure for 48 hours.
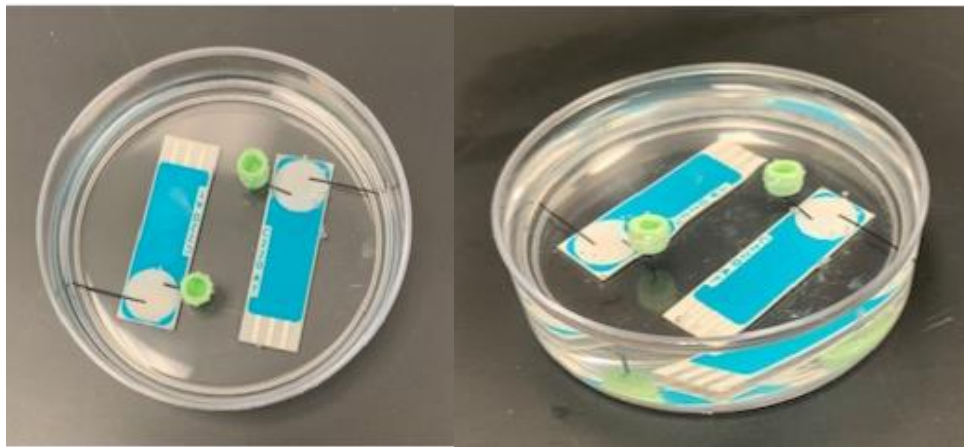
Removal:
1. Once fully cured, remove the PDMS from the petri dish (this can be done using a blade and going around the edges or by breaking the petri dish).
2. The sensor can be removed from the PDMS by hand (gently), along with the disk.
3. The PLA channels can either be removed by gently pulling (if there is no resistance), or the platform can be soaked in acetone overnight and a syringe can be used to remove the remaining PLA.
4. Once removed, use a syringe to pump DI water through the system to ensure all channels are open and connected. A needle can be used to open/connect any channels if needed.
5. The platform can then be sliced in half using a blade to create the two separate microfluidic platforms.
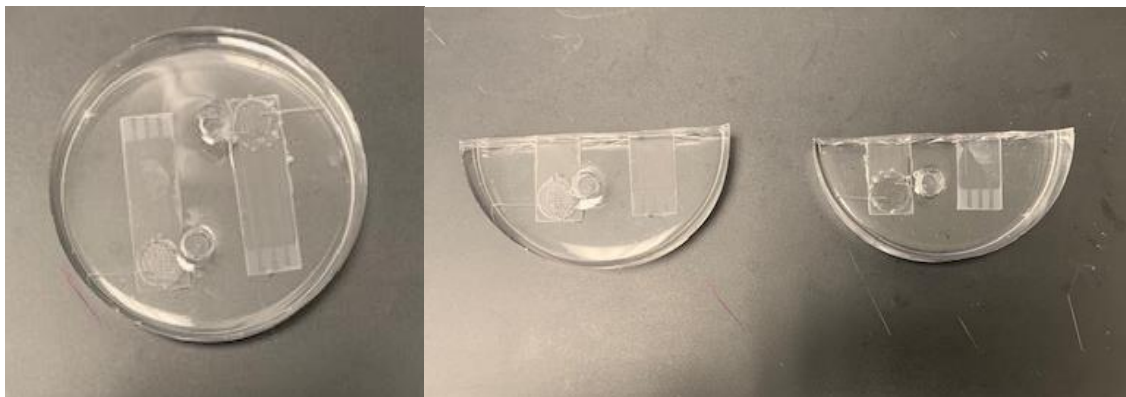
Cyclic Voltammetry Experiments on Blank Electrodes

Procedure:
1. Clean electrodes using the RCA-1 method.
2. Prepare solution of 5 mM potassium ferricyanide in PBS by adding 0.01646 g of potassium ferricyanide to 10 mL PBS.
3. Set up the sensor by attaching the sensor to the CAC cable and placing the sensor inside the beaker of solution. Place a stir bar inside beaker and place on stir plate.
4. Attach platinum gauze (external counter electrode) to the counter lead of the potentiostat and place in solution close to sensor electrodes.
5. Attach external glass reference electrode to the reference lead of the potentiostat and place in solution close to sensor electrodes.
6. Run a cyclic voltammetry (multiple cycles) experiment with a potential range of +0.7V to -0.15V and 20 cycles.
7. Run at the selected scan rate (50 mV/s, 100 mV/s, 150 mV/s, 200 mV/s) and adjust the stir bar speed accordingly.

REFERENCES

Ahmed, A., Rushworth, J.V., Hirst, N.A., Millner, P.A. (2014). Biosensors for Whole-Cell Bacterial Detection. *Clinical Microbiology Reviews* 27, 631-646.

Alvarez, M., Zinoviev, K., Moreno, M., Lechuga, L. (2008). Cantilever Biosensors. In F. S. Ligler & C. R. Taitt (Eds.), Optical Biosensors: Today and Tomorrow (2nd ed., pp. 419-452). Elsevier.

Anandan, V., Yang, X., Kim, E., Rao, Y.L., Zhang, G. (2007). Role of Reaction Kinetics and Mass Transport in Glucose Sensing with Nanopillar Array Electrodes. *Journal of Biological Engineering* 1:5.

Anandan, V., Gangadharan, R., Zhang, G. (2009). Role of SAM Chain Length in Enhancing the Sensitivity of Nanopillar Modified Electrodes for Glucose Detection. *Sensors* 9, 1295-1305.

Arlett, J. L., Myers, E. B., & Roukes, M. L. (2011). Comparative advantages of mechanical biosensors. *Nature Nanotechnology*, 6(4), 203–215. https://doi-org.ezproxy.uky.edu/10.1038/nnano.2011.44

Asal, M., Ozen, O., Sahinler, M., Baysal, H.T., Polatoglu, I. (2018). An Overview of Biomolecules, Immobilization Methods and Support Materials of Biosensors. *Sensor Review* 39, 377-386.

Bahadir, E.B. and Sezginturk, M.K. (2016). A Review on Impedimetric Biosensors. *Artificial Cells, Nanomedicine & Biotechnology* 44, 248-262.

Biosensing Instrument Inc. (2014). *Technical Note 101: Principle of SPR Detection: Intensity profile and shift of the SPR angle.*

Borisov, S. M., and Wolfbeis, O. S. (2008). Optical Biosensors. *Chem. Rev.*, 108, 423-461.

Bryan, T., Luo, X., Bueno, P., Davis, J. (2013). An Optimized Electrochemical Biosensor for the Label-Free Detection of C-reactive Protein in Blood. *Biosensors and Bioelectronics*, 39, 94-98.

Catherino, H. (2006). Electrochemical Biosensors. 1313-1318.

Chaubey, A., and Malhotra, B.D. (2002). Mediated Biosensors. *Biosensors & Bioelectronics* 17, 441-456.

Chauhan, N. and Pundir, C.S. (2014). Amperometric Determination of Acetylcholine – A Neurotransmitter, by Chitosan/Gold-Coated Ferric Oxide Nanoparticles Modified Gold Electrode. *Biosensors and Bioelectronics* 61, 1-8.

Daniels, J.S. and Pourmand, N. (2007). Label-Free Impedance Biosensors: Opportunities and Challenges. *Electroanalysis* 19, 1239-1257.

Detect COVID-19 in as Little as 5 Minutes. (2020). Retrieved from https://www.abbott.com/corpnewsroom/product-and-innovation/detect-covid-19-in-as-little-as-5-minutes.html

Elgrishi, N., Rountree, K.J., McCarthy, B.D., Rountree, E.S., Eisenhart, T.T., Dempsey, J.L. (2018). A Practical Beginner's Guide to Cyclic Voltammetry. *J. Chem. Educ.* 95, 197-206.

Emergency Use Authorizations. (2020). Retrieved from https://www.fda.gov/medical-devices/emergency-situations-medical-devices/emergency-use-authorizations#covid19ivd

Fritz, J. (2008). Cantilever Biosensors. *Analyst* 133, 855-863.

Gangadharan, R., Anandan, V., Zhang, A., Drwiega, J.C., Zhang, G. (2011). Enhancing the Performance of a Fluidic Glucose Biosensor with 3D Electrodes. *Sensors and Actuators* B 160, 991-998.

Gao, J., Huang, W., Chen, Z., Yi, C., Jiang, L. (2019). Simultaneous Detection of Glucose, Uric Acid and Cholesterol Using Flexible Microneedle Electrode Array-Based Biosensor and Multi-Channel Portable Electrochemical Analyzer. *Sensors & Actuators: B. Chemical* 287, 102-110.

Gholivand, M.B., Khodadadian, M. (2014). Amperometric Cholesterol Biosensor Based on the Direct Electrochemistry of Cholesterol Oxidase and Catalase on a Graphene/Ionic Liquid-Modified Glassy Carbon Electrode. *Biosensors and Bioelectronics* 53, 472-478.

Grieshaber, D., MacKenzie, R., Voros, J., and Reimhult, E. (2008). Electrochemical Biosensors – Sensor Principles and Architectures. *Sensors* 8, 1400-1458.

Gupta, B., Shrivastav, A., Usha, S. (2016). Surface Plasmon Resonance-Based Fiber Optic Sensors Utilizing Molecular Imprinting. *Sensors (Basel)* 16, 1381-1414.

Gupta, B.D., Verma, R.K. (2009). Surface Plasmon Resonance-Based Fiber Optic Sensors: Principle, Probe Designs, and Some Applications. *Journal of Sensors* 2009, 1-12.

Hegnerova, K., Bockova, M., Vaisocherova, H., Kristofikova, Z., Ricny, J., Ripova, D., Homola, J. (2009). Surface Plasmon Resonance Biosensors for Detection of Alzheimer Disease Biomarker. *Sensors and Actuators B* 139, 69-73.

Hernandez-Vargas, G., Sosa-Hernandez, J.E., Saldarriaga-Hernandez, S., Villalba-Rodriquez, A.M., Parra-Saldivar, R., Iqbal, H.M.N. (2018). Electrochemical Biosensors: A Solution to Pollution Detection with Reference to Environmental Contaminants. *Biosensors* 8, 1-29.

Hoa, X.D., Kirk, A.G., Tabrizian, M. (2007). Towards Integrated and Sensitive Surface Plasmon Resonance Biosensors: A Review of Recent Progress. *Biosensors and Bioelectronics* 23, 151-160.

Homola, J., Yee, S., Myszka, D. (2002). Surface Plasmon Resonance Biosensors. In F. Ligler & C. Taitt (Eds.), *Optical Biosensors Present & Future* (pp. 207-251). Burlington: Elsevier Science.

Hu, W.P., Hsu, H.-Y., Chiou, A., Tseng, K.Y., Lin, H.-Y., Chang, G.L., Chen, S.-J. (2006). Immunodetection of Pentamer and Modified C-reactive Protein using Surface Plasmon Resonance Biosensing. *Biosensors and Bioelectronics* 21, 1631-1637.

Jackson, K., Barisone, G., Diaz, E., Jin, L., DeCarli, C., Despa, F. (2013). Amylin Deposition in the Brain: a Second Amyloid in Alzheimer's Disease? *Ann Neurol.* 74, 517-526.

Ji, Hai-Feng and Armon, B.D. (2010). Approaches to Increasing Surface Stress for Improving Signal-to-Noise Ratio of Microcantilever Sensors. *Anal. Chem.* 82, 1634-1642.

Jin, D.S., Brightbill, E.L., Vogel, E.M. (2019). General Model for Mass Transport to Planar and Nanowire Biosensor Surfaces. *J. Appl. Phys.* 125, 114502.

Kaur, G., Tomar, M., Gupta, V. (2018). Development of a Microfluidic Electrochemical Biosensor: Prospect for Point-of-care Cholesterol Monitoring. *Sensors and Actuators* 261, 460-466.

Kim, B., Lee, H., Lee, N. (2019). A Durable, Stretchable, and Disposable Electrochemical Biosensor on Three-dimensional Micro-patterned Stretchable Substrate. *Sensors and Actuators B: Chemical* 283, 312-320.

Kubicek-Sutherland, J., Vu, D., Mendez, H., Jakhar, S., and Mukundan, H. (2017). Detection of Lipid and Amphiilic Biomarkers for Disease Diagnostics. *Biosensors* 7, 1-24.

Layqah, L.A. and Eissa, S. (2019). An Electrochemical Immunosensor for the Corona Virus associated with the Middle East Respiratory Syndrome using an Array of Gold Nanoparticle-modified Carbon Electrodes. *Microchimica Acta* 224, 1-10.

Lee, S.-J., Anandan, V., Zhang, G. (2008). Electrochemical Fabrication and Evaluation of Highly Sensitive Nanorod-Modified Electrodes for a Biotin/Avidin System. *Biosensors and Bioelectronics* 23, 1117-1124.

Lee, I., Luo, X., Huang, J., Cui, X., Yun, M. (2012). Detection of Cardiac Biomarkers Using Single Polyaniline Nanowire-Based Conductometric Biosensors. *Biosensors* 2, 205-220.

Lewis, J.L. (2020). Overview of Acid-Base Balance. Merck Manual Consumer Version.

Li, L., Dutkiewicz, E., Huang, Y. Zhou, H., Hsu, C. (2018). Analytical Methods for Cholesterol Quantification. *Journal of Food and Drug Analysis* 27, 375-386.

Liang, G., Luo, Z., Liu, K., Wang, Y., Dai, J., and Duan, Y. (2016). Fiber Optic Surface Plasmon Resonance-Based Biosensor Technique: Fabrication, Advancement, and Application. *Critical Reviews in Analytical Chemistry* 46, 213-223.

Long, F., Zhu, A., Shi, H. (2013). Recent Advances in Optical Biosensors for Environmental Monitoring and Early Warning. *Sensors* 13, 13928-13948.

Luka, G., Ahmadi, A., Nijjaran, H., Alocilja, E., DeRosa, M., Wolthers, K., Malki, A., Aziz, H., Althani, A., Hoorfar, M. (2015). Microfluidics Integrated Biosensors: A Leading Technology towards Lab-on-a-Chip and Sensing Applications. *Sensors* 15, 30011-30031.

Marazuela, M.D., and Moreno-Bondi, M.C. (2002). Fiber-Optic Biosensors – An Overview. *Anal Bioanal Chem* 372, 664-682.

Mohammed, M. and Desmulliez, M.P.Y. (2014). Autonomous Capillary Microfluidic System with Embedded Optics for Improved Troponin I Cardiac Biomarker Detection. *Biosensors and Bioelectronics* 61, 478-484.

Murugaiyan, S., Ramasamy, R., Gopal, N., and Kuzhandaivelu, V. (2012). Biosensors in Clinical Chemistry: An Overview. *Adv Biomed Res* 3:67.

Nikoleli, G., Ibupoto, Z., Nikolelis, D., Likodimos, V., Psaroudakis, N., Tzamtzis, N., Willander, M., Hianik, T. (2013). Potentiometric Cholesterol Biosensing Application of Graphene Electrode with Stabilized Polymeric Lipid Membrane. *Cent. Eur. J. Chem.* 11(9), 1554-1561.

Pohanka, M., Skladal, P. (2008). Electrochemical Biosensors – Principals and Applications. *J. Appl. Biomed.* 6, 57-64.

Prabowo, B.A., Purwidyantri, A., Liu, K. (2018). Surface Plasmon Resonance Optical Sensor: A Review on Light Source Technology. *Biosensors* 8, 1-27.

Prakash, S., Pinti, M., Bhushan, B. (2012). Theory, Fabrication and Applications of Microfluidic and Nanofluidic Biosensors. *Phil. Trans. R. Soc.* 370, 2269-2303.

Qureshi, A., Gurbuz, Y., Niazi, J. (2012). Biosensors for Cardiac Biomarkers Detection: A Review. *Sensors and Actuators B* 171-172, 62-76.

Rahman, M. (2014). Reusable and Mediator-Free Cholesterol Biosensor Based on Cholesterol Oxidase Immobilized onto TGA-SAM Modified Smart Bio-Chips. *PLOS ONE* 9, e100327.

Ramsden, J. (1997). Optical Biosensors. *J. Mol. Recogn.* 10, 109-120.

Rodriguez, B. A.G., Trindade, E. K.G., Cabral, D. G.A., Soares, E. C.L., Menezes, C. E.L., Ferreira, D. C.M., Mendes, R. K., Dutra, R. F. (2015). Nanomaterials for Advancing the Health Immunosensor. Biosensors – Micro and Nanoscale Applications, Toonika Rinken, IntechOpen.

Rushworth, J. V., Ahmed, A., Millner, P.A., Pike, D.J., Hirst, N.A., Goode, J.A. (2013). *Impedimetric Biosensors for Medical Applications: Current Progress and Challenges.* Momentum Press.

Rushworth, J., Ahmed, A., Griffiths, H., Pollock, N., Hooper, N., Millner, P. (2014). A Label-free Electrical Impedimetric Biosensor for the Specific Detection of Alzheimer's Amyloid-beta Oligomers. *Biosensors and Bioelectronics* 56, 83-90.

Russell, S. (2017). *Continuous Glucose Monitoring*. National Institute of Diabetes and Digestive and Kidney Diseases. https://www.niddk.nih.gov/health-information/diabetes/overview/managing-diabetes/continuous-glucose-monitoring

Saxena, U. and Das, A. (2016). Nanomaterials Towards Fabrication of Cholesteorl Biosensors: Key Roles and Design Approaches. *Biosensors and Bioelectronics* 75, 196-205.

Sing, N., Rai, P., Ali, A, Kumar, R., Sharma, A., Malhotra, B. D., John, R. (2019). A Hollow-nanosphere-based Microfluidic Biosensor for Biomonitoring of Cardiac Troponin I. *J. Mater. Chem. B.* 7, 3826-3839.

Song, C., Deng, P., Que, L. (2018). Rapid Multiplexed Detection of Beta-amyloid and Total-tau as Biomarkers for Alzheimer's Disease in Cerebrospinal Fluid. *Nanomedicine: NBM* 14, 1845-1852.

Sun, L., Zhong, Y., Gui, J., Wang, X., Zhuang, X., Weng, J. (2018). A Hydrogel Biosensor for High Selective and Sensitive Detection of Amyloid-beta Oligomers. *International Journal of Nanomedicine* 13, 843-856.

Taniguchi, T., Murakami, Y., Sohgawa, M., Yamashita, K., Noda, M. (2017). Detection of Aβ(1-40) Protein in Human Serum as a Causative Agent of Alzheimer's Disease by Strain Gauge Cantilever Biosensor Immobilizing Liposome Incorporating Cholesterol. *Proceedings* 1, 503-506.

Trinh, Q. (2011). "Cottrell Equation for the Potential-Step Experiment". https://demonstrations.wolfram.com/CottrellEquationForThePotentialStepExperiment/

Urschel, K., Cicha, I. (2015). TNF-a in the Cardiovascular System: from Physiology to Therapy. *International Journal of Interferon, Cytokine and Mediator Research* 7, 9-25.

Voros, J., Ramsden, J. J., Csucs, G., Szendro, I., De Paul, S. M., Textor, M., Spencer, N. D. (2002). Optical Grating Coupler Biosensors. *Biomaterials* 23, 3699-3710.

Wang, J. (2000). *Analytical Electrochemistry* (2nd edition). John Wiley & Sons, Inc.

Wang, X., Hu, L. (2020). Review – Enzymatic Strips for Detection of Serum Total Cholesterol with Point-of-Care Testing (POCT) Devices: Current Status and Future Prospect. *Journal of The Electrochemical Society* 167, 037535.

Wee, K.W., Kang, G.Y., Park, J., Kang, J.Y., Yoon, D.S., Park, J.H., Kim, T.S. (2005). Novel Electrical Detection of Label-free Disease Marker Proteins using Piezoresistive Self-sensing Micro-cantilevers. *Biosensors and Bioelectronics* 20, 1932-1938.

Xpert Xpress SARS-CoV-2 has received FDA Emergency Use Authorization. (2020). Retrieved from https://www.cepheid.com/coronavirus

Xu, D., Huang, X., Guo, J., Ma, X. (2018). Automatic Smartphone-based Microfluidic Biosensor System at the Point of Care. *Biosensors and Bioelectronics* 110, 78-88.

Zhang, Z., Murakami, Y., Taniguchi, T., Sohgawa, M., Yamshita, K., Noda, M. (2017). A Cantilever-based Biosensor for Real-time Monitoring of Interactions between Amyloid-β(1-40) and Membranes Comprised of Phosphatidylcholine Lipids with Different Hydrophobic Acyl Chains. *Electroanalysis* 29, 722-729.

Education:

University of Kentucky, Lewis Honors College   Aug. 2013 – Dec. 2018
Bachelor of Science in Biosystems Engineering
Minor in Biomedical Engineering

Professional Experience:

Bioanalytics & Integrative Bioengineering Lab   Aug. 2019 – Feb. 2022
Research Assistant

Piramal Pharma Solutions
Process Engineer I   Mar. 2019 – Aug. 2019
Intern, Process Engineering   May 2018 – Nov. 2018

KY Transportation Center   Aug. 2015 – May 2018
Student Research Engineer

Professional Activities:

Society for Biomaterials   Aug. 2019 – May 2021
President

Alpha Epsilon Honors Society for Ag. & Biological Engineers   May 2017 – May 2018
President

Honors

2020 Joyce M. Evans Excellence in Service Award

Presentations

Lauren Bell, Elizabeth Aikman, Yu Zhao, Frédérique Yiannikouris and Guigen Zhang, 2019, An In-Situ and Real-time Means to Detect Biomarkers Crucial to Cardiovascular Diseases, 2019 Cardiovascular Day Conference (poster)

Lauren Bell, Elizabeth Aikman, Yu Zhao, Frédérique Yiannikouris and Guigen Zhang, 2020, An Electrochemical Sensor for In-Situ Application, BMES 2020 Virtual Annual Meeting (poster)

Lauren Bell, Yu Zhao, Frédérique Yiannikouris and Guigen Zhang, 2021, An Electrochemical Sensor for Oxygen and Glucose Detection, UK CCTS Research Days (poster)

<div align="right">Lauren Bell</div>